SANDIA REPORT

Filtered Rayleigh Scattering Diagnostic for Multi-Parameter Thermal-Fluids Measurements: LDRD Final Report

Sean P. Kearney, Steven J. Beresh, Robert W. Schefer, and Thomas W. Grasser

Approved for public release; further dissemination unlimited.

Sandia National Laboratories

Issued by Sandia National Laboratories, operated for the United States Department of Energy by Sandia Corporation.

FILTERED RAYLEIGH SCATTERING DIAGNOSTIC FOR MULTI-PARAMETER THERMAL-FLUIDS MEASUREMENTS : LDRD FINAL REPORT

Sean P. Kearney, Steven J. Beresh, and Thomas W. Grasser
Engineering Sciences Center
Thermal-Fluid Experimental Sciences
Sandia National Laboratories
Albuquerque, NM 87185

Robert W. Schefer
Combustion Research Facility
Reacting Flow Research
Sandia National Laboratories
Livermore, CA 94551

ABSTRACT

Simulation-based life-cycle-engineering and the ASCI program have resulted in models of unprecedented size and fidelity. The validation of these models requires high-resolution, multi-parameter diagnostics. Within the thermal/fluids disciplines, the need for detailed, high-fidelity measurements exceeds the limits of current Engineering Sciences capabilities and severely tests the state of the art; therefore, a diagnostic development effort is warranted. The focus of this LDRD is the development and application of filtered Rayleigh scattering (FRS) for high-resolution, nonintrusive measurement of gas-phase velocity and temperature. This multi-parameter technique adds significant experimental capability to several Sandia programs including Fire Science and Technology (FS&T) and Aerosciences programs in the Engineering Sciences Center (9100) and Reacting Flow Research at the Combustion Research Facility (8300).

With FRS, the flow is laser-illuminated and Rayleigh scattering from naturally occurring sources is detected through a molecular filter. The filtered transmission may be interpreted to yield point or planar measurements of three-component velocities and/or thermodynamic state. Different experimental configurations may be employed to obtain compromises between spatial resolution, time resolution, and the quantity of simultaneously measured flow variables. This capacity for multi-parameter, non-intrusive instrumentation represents an unprecedented advance beyond presently available techniques in the Engineering Sciences Center and in the larger scientific arena. Furthermore, measurements may be made using naturally occurring scattering centers, eliminating potentially intractable difficulties associated with particulate or chemical seeding in a hypersonic or reacting environment. Molecular-filter absorption of scattered light from solid boundaries also makes FRS advantageous for detailed boundary-layer measurements.

These advantages make FRS an attractive alternative to developed techniques and offer a substantial payoff impacting multiple thermal/fluids disciplines. Moreover, a virtually identical experimental configuration may be utilized for both aerodynamic and thermal diagnostic applications simply by adjusting the laser and molecular filter. These measurements are ideally suited for use in production-scale facilities, where many other techniques are difficult to implement.

In this report, we present the results of a three-year LDRD-funded effort to develop FRS combustion thermometry and Aerosciences velocity measurement systems. The working principles and details of our FRS opto-electronic system are presented in detail. For combustion thermometry we present 2-D, spatially correlated FRS results from nonsooting premixed and diffusion flames and from a sooting premixed flame. The FRS-measured temperatures are accurate to within ±50 K (3%) in a premixed CH_4-air flame and within ±100 K for a vortex-strained diluted CH_4-air diffusion flame where the FRS technique is severely tested by large variation in scattering cross section. In the diffusion flame work, FRS has been combined with Raman imaging of the CH_4 fuel molecule to correct for the local light scattering properties of the combustion gases. To our knowledge, this is the first extension of FRS to nonpremixed combustion and the first use of joint FRS-Raman imaging. FRS has been applied to a sooting C_2H_4-air flame and combined with LII to assess the upper sooting limit where FRS may be utilized. The results from this sooting flame show FRS temperatures has potential for quantitative temperature imaging for soot volume fractions of order 0.1 ppm. FRS velocity measurements have been performed in a Mach 3.7 overexpanded nitrogen jet. The FRS results are in good agreement with expected velocities as predicted by inviscid analysis of the jet flowfield. We have constructed a second FRS opto-electronic system for measurements at Sandia's hypersonic wind tunnel. The details of this second FRS system are provided here. This facility is currently being used for velocity characterization of these production hypersonic facilities.

LIST OF FIGURES

LIST OF TABLES

TABLE OF CONTENTS

This page has been intentionally left blank

INTRODUCTION

This document serves as the final LDRD report for the project "Filtered Rayleigh Scattering Diagnostic for Multi-Parameter Thermal-Fluids Measurements." This project was funded by the Engineering Sciences investment area for the purpose of cultivating a state-of-the-art diagnostic tool that would benefit both Fire Science and Aerosciences programs within the Engineering Sciences Center. Development of the Filtered Rayleigh Scattering (FRS) diagnostic at Sandia also has potential impact on convective heat-transfer and fluid-mixing measurements in the Engineering Sciences Center and for Basic Energy and Hydrogen Sciences programs at Sandia's Combustion Research Facility. The diagnostic development work has followed two parallel paths with one thrust of the project directed at temperature imaging in nonpremixed and sooting flames (Fire and Combustion Sciences thrust) and the other track devoted to FRS velocimetry in compressible flowfields (Aerosciences thrust). Both programs are heavily leveraged against one another as 80% or more of the FRS opto-electronic system was used for both Fire and Combustion and Aerosciences measurements.

This document is largely a compilation of published conference papers and submitted journal articles that have been reformatted to present a cogent presentation of the course of this 3-year project. The report has been organized such that the Fire and Combustion and Aerosciences thrusts are discussed under separate subheadings. In addition to making the report simpler to compile from existing publications, it also permits the reader who is interested in only one of these applications to readily select the pertinent information. The report begins with a discussion of previous FRS work and is followed by a description of the Sandia FRS facility. The results of FRS temperature imaging experiments for Fire and Combustion applications are then presented, followed by a discussion of FRS velocimetry for Aerosciences applications. The report concludes with a summary of accomplishments under the LDRD funding and a description of ongoing work with FRS at Sandia.

FRS for Temperature Imaging in Fire and Combustion Applications

Multi-point, nonintrusive imaging techniques are powerful methods for obtaining a quantitative understanding of complex flows. The excellent spatial resolution and spatial correlation provided by imaging methods is especially useful for development and testing of subgrid-scale models for turbulent flows and for providing quantitative visualization of highly

complex, unsteady flow fields. In most fluid dynamics experiments, the velocity field is of primary interest and, to this end, much attention has been paid to the development of laser-diagnostic approaches for velocity imaging, namely particle image velocimetry (PIV), which is now a standard in most any fluids research laboratory. In applications where convective heat or mass transfer is the engineering quantity of interest, where buoyancy forces are driving the flow, and/or in chemically reacting flows, the temperature and scalar fields are of equal or greater importance than the velocity field.

Several laser-based techniques have gained popularity for nonintrusive 2-D temperature imaging namely: linear (unfiltered) Rayleigh scattering (LRS), planar laser-induced fluorescence (PLIF), and filtered Rayleigh scattering (FRS). Linear Rayleigh scattering imaging was first demonstrated in flames by Fourguette *et al.* [1], who used a specialized fuel mixture to keep the Rayleigh scattering cross section constant throughout the flame. LRS has also been used in heat transfer studies [2] and fluid mixing experiments [3]. LRS has the advantage of simplicity but the disadvantage of weak signal strength, which can be quickly overwhelmed by Mie scattering from solid surfaces, room particulate and soot. The PLIF technique [4, 5] provides for noninvasive imaging of species mole fraction and temperature with greatly increased signal strength relative to LRS. However, full-field PLIF thermometry often requires seeding of the flowfield with a foreign chemical species, which increases the complexity of the experiment and, in reacting flows, can leave "holes" in the data field due to combustion or pyrolysis of the seed molecule and can artificially impact flame chemistry.

FRS is a modification of the LRS technique, first put forth by Miles *et al.* [6] for flow visualization. FRS takes advantage of the full-field, unseeded capabilities of LRS while providing increased rejection of Mie scattering interferences from the illuminating laser line. This significant rejection of background noise is achieved by placing a molecular iodine vapor cell in front of the detector and using an injection-seeded Nd:YAG laser to tune the laser line to an absorption maximum of the iodine spectrum. The seeded laser lineshape and associated Mie scattering from surfaces and flowfield particulate are thereby strongly rejected while a significant portion of the Doppler-broadened Rayleigh signal leaks past the filter and reaches the detector. Single-laser-pulse FRS temperature imaging has recently been applied in premixed flames by Elliott and coworkers [7, 8] and by Most and Leipertz [9]. These studies also included demonstration of simultaneous FRS/PIV for temperature/velocity imaging. Demonstration of

FRS thermometry in a lightly sooting flame has also been provided by Hoffman *et al.* [10], who present temperature data but did not quantify the soot volume fraction over which their FRS measurements were successful.

In this work, we present the construction and performance of the Sandia FRS instrument for quantitative temperature imaging. The Fire and Combustion temperature-imaging portion of this work has proceeded in a systematic fashion so that the impact of local variation in Rayleigh cross section, which is by far the largest source of systematic error in any Rayleigh measurement, can be adequately addressed. The course of the FRS thermometry program is summarized in bullet form here and explained in the next paragraph.

- Hot-air jet measurements for "shakedown" testing of the Sandia FRS facility – no variation in Rayleigh cross section
- Premixed CH_4-air flame to assess impact of moderate variations in local Rayleigh cross section and begin work in reacting flows
- CH_4-air diffusion flame to extend FRS to the most severe variations in Rayleigh cross section. Joint FRS-Raman imaging required
- Premixed C_2H_4-air flame to assess FRS diagnostic performance in a sooting combustion system with only moderate variations in Rayleigh cross section.

The temperature imaging work begins with "shakedown" type measurements in a heated air jet where there are no variations in Rayleigh cross section so that the performance of our FRS optical system can be initially assessed. Reacting flow thermometry was then commenced in a premixed CH_4-air flat flame from the Hencken burner. This flame allowed us to assess the impact of Rayleigh cross section on FRS measurements in a well characterized premixed combustion system. FRS was then extended to nonpremixed combustion using a 2-D slot diffusion-flame geometry. The variations in FRS cross section were most severe for the diffusion flame case and joint Raman imaging of the local fuel mole fraction was combined with FRS to make accurate estimates of the local scattering behavior. To our knowledge, this work is the first extension of the FRS technique to nonpremixed combustion systems and the first report of joint FRS-Raman measurements. The FRS temperature imaging experiments were concluded with an investigation of a premixed sooting C_2H_4-air flat flame on the McKenna burner. These

experiments allowed us to assess the performance of FRS thermometry in sooting combustion systems, while using a premixed flame where variations in Rayleigh cross section are less severe.

FRS for Velocity Imaging in Aerosciences Applications

One of the most important parameters towards understanding supersonic and hypersonic flows is the velocity field, for which past laboratory studies have employed a variety of measurement techniques. Traditional and somewhat venerable techniques have been Pitot probes and hot-wire anemometry, but both diagnostics suffer from their intrusive nature and are restricted to point measurements. Laser Doppler velocimetry (LDV) overcomes the intrusive nature of probe-based measurements, as well as avoiding the density-dependence of hot-wire anemometry. This was followed by the development of particle image velocimetry (PIV), which has the same advantages but offers a planar field of velocities. While both LDV and PIV have proven to be effective tools for measuring the velocity fields of supersonic flows, for the higher Mach numbers seen in hypersonic flows, particle lag arising from these techniques complicates the measurement [11, 12].

Avoidance of particle lag and other seeding challenges is one reason why Doppler global velocimetry (DGV), alternatively known as planar Doppler velocimetry (PDV), is an attractive technique for studying supersonic and hypersonic flows. DGV or PDV are the common terminology in the literature for FRS velocimetry and we will use the terms 'DGV' and 'FRS' interchangeably when referring to velocity imaging applications in this document. Like PIV, DGV provides a planar field of velocities but does so using a different physical approach: whereas PIV tracks particle displacements, DGV measures the velocity-induced Doppler shift of laser light. It also has the appeal of providing an improved spatial resolution as compared to PIV and can be transferred to studies involving different flow physics or, more challengingly, broadened to provide simultaneous measurement of other properties such as temperature and density. DGV is particularly well-suited to larger experimental facilities such as Sandia's hypersonic wind tunnel (HWT), in which particle-based velocimetry is problematic. While newer than LDV and PIV, the DGV technique has matured in recent years and is sufficiently well understood that it can provide a reliable means of gathering velocity data in supersonic and hypersonic flowfields.

In the present investigation, Doppler global velocimetry is being developed as a diagnostic tool to study supersonic and hypersonic flows. While the primary interest is application of DGV to the HWT, the development of DGV from the ground up is better accomplished in a small, inexpensive benchtop facilty. Not only does this avoid the cost and complexity of operating the HWT during the initial development effort, it also allows for more frequent operation of the facility and hence more rapid acquisition of exploratory measurements. The benchtop facility that has been chosen for the present work is an overexpanded jet exhausting from an axisymmetric supersonic nozzle with an exit diameter of 6.35 mm (0.250 inch). This flowfield is of interest in its own right because the jet captures some of the physics found on spin-up rocket motors employed on gravity bombs. If the backpressure placed on a supersonic jet is sufficiently large compared to the jet exit pressure, shock-induced separation within the nozzle itself will occur. Although in some circumstances this can actually increase the thrust, detrimental effects also are created, including a lateral component to the thrust vector and unsteady loads that may induce dangerous vibrations [13]. Many decades of research into this subject have yielded an increased understanding of nozzle separation physics [14-17] but it remains an active area of investigation for both rocket engines and thrusters used for attitude and roll control [18-21].

The present document describes the specifics of the implementation of the DGV system for the current measurements and provides velocity data concerning the jet exhausting from an axisymmetric Mach 3.7 nozzle. In addition to providing important data on flow separation within a supersonic nozzle, the development of the DGV technique in the present flowfield serves as a convenient testbed prior to future implementation in a hypersonic wind tunnel. Once a working DGV system has been constructed for the supersonic jet, it can be altered for application to the HWT based upon what has been learned during the benchtop development process. The design and construction of a duplicate DGV system specifically for the HWT is described following the presentation of the DGV results from the overexpanded benchtop-scale jet.

FRS WORKING PRINCIPLE

FRS Temperature Imaging

The working principles behind the FRS temperature-imaging technique are summarized here. Further detail can be found in papers by Elliott *et al.* [7, 8] and by Most and Leipertz [9]. A schematic explanation of the FRS method is shown in Fig. 1. FRS is an extension of the traditional LRS imaging technique in which a molecular filter is placed in front of the detector, usually an intensified CCD camera as shown in Fig. 1a. A frequency-doubled Nd:YAG laser is typically used to make the Rayleigh measurements and molecular iodine vapor, which has an atlas of absorption resonances in the vicinity of the 532-nm laser output, is employed as the filter molecule. When the Nd:YAG oscillator is injection seeded, the laser linewidth is an order of magnitude less than the I_2 absorption linewidth as seen in Fig. 1b. Injection seeding also allows for tuning of the laser output over a narrow ~ 1 cm^{-1} range so that the laser line can be made coincident with a strong absorption maximum. Strong Mie scattering interferences, which have the same spectral profile as the laser lineshape, are significantly attenuated by the filter, facilitating measurements in open laboratory air, dirty production environments and in sooting flames where LRS often fails.

For quantitative scalar imaging, the FRS signal must be related to the physical variable of interest such as temperature or mole fraction. This is done by integrating the product of the measured I_2 filter transmission spectrum and the Rayleigh light scattering spectrum, and summing the contributions from each species present locally in the flow according to this expression,

$$S(T,\underline{\chi}) = C\,I_o\,N$$
$$\times\ \sum_k \chi_k \left(\frac{\partial\sigma}{\partial\Omega}\right)_k \int_{\Delta\omega} \Re_k(\omega;T,M_k)\tau(\omega)\,d\omega. \tag{1}$$

In Eq. 1, *S* is the FRS signal which most generally depends upon temperature, pressure, and the local chemical composition, *C* is a calibration constant associated with the FRS optical system, I_o is the local laser light-sheet intensity, $N = P/k_BT$ is the local number density, χ_k is the mole fraction of the *k*th species present locally in the flowfield, $(\partial\sigma/\partial\Omega)_k$ is the differential Rayleigh
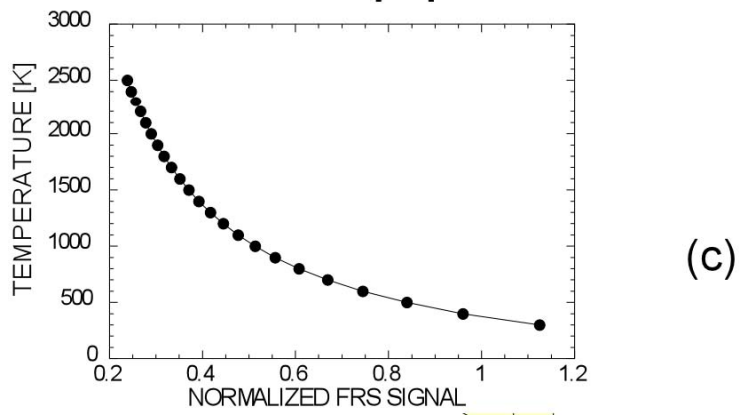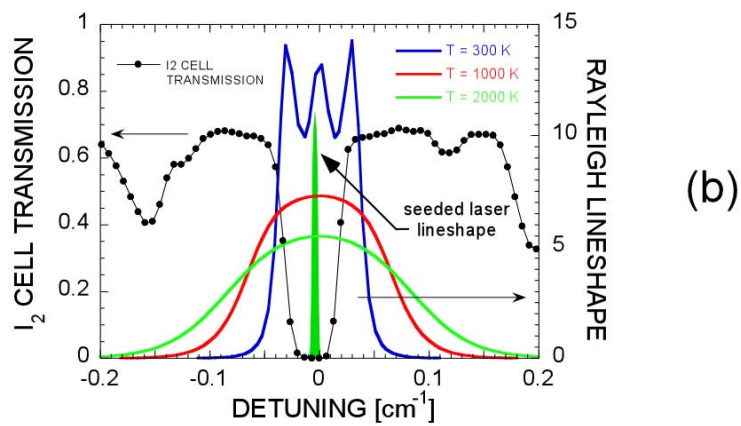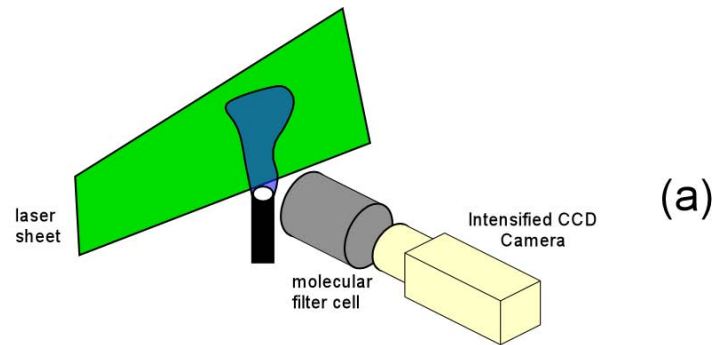
Figure 1 – FRS working principle: (a) FRS imaging configuration, (b) spectral profiles of molecular filter and nitrogen Rayleigh lineshapes, (c) representative calibration curve for FRS thermometry.

cross section for the *k*th species, M_k is the molecular weight of the *k*th species, ω is the scattered light frequency, $\tau(\omega)$ is the measured transmission spectrum of the molecular filter, and $\Re_k(\omega; T, M_k)$ is the normalized Rayleigh lineshape function for the *k*th species calculated from the S6 model of Tenti *et al.* [22]. $\Re_k(\omega; T, M_k)$ has an additional dependence on transport properties which becomes especially important at higher pressures and lower temperatures. This transport-property dependence is not expected to be significant for fire and combustion applications, where the temperatures are high, or for aerosciences applications, where the pressure and density are very low.

The reliability of the S6 model has been experimentally verified for a host of atomic, diatomic and polyatomic molecules including He, Ne, Ar, H_2, N_2, HD, CO_2, C_2F_6 [22-24]. In the S6 model, the Rayleigh lineshape is parameterized by the following dimensionless groups [22]*,

$$Y = \frac{\lambda_o P}{4\pi \mu \sin \theta/2} \sqrt{\frac{m}{2 k_B T}} \quad , \tag{2}$$

$$X = \frac{c \Delta\omega \lambda_o}{2 \sin \theta/2} \sqrt{\frac{m}{2 k_B T}} \quad . \tag{3}$$

In Eqs. 2 and 3, λ_o is the incident laser wavelength, μ is the dynamic viscosity, m is the mass of a single molecule, k_B is Boltzmann's constant, c is the vacuum speed of light, θ is the angle between the laser-sheet propagation vector and the CCD detection axis, and $\Delta\omega$ is the wavenumber shift of the Rayleigh-scattered light. The *Y* parameter given in Eq. 2 provides a relative measure of the wavelength of the exciting laser beam to the mean-free path between molecular collisions. For many molecules at atmospheric pressure, a *Y* parameter of order 1 or less, implies that the impact of collisions between different species is minimized so that light scattering from each species can be summed independently, as in Eq. 1, without considering gas-mixture properties. This approximation becomes even better at flame temperatures where mean-free paths are even longer. The *X* parameter given in Eq. 3 is essentially the wavenumber shift of scattered light from the laser line normalized by the Doppler linewidth.

---

* The Y-parameter given in Eq. 2 has been derived directly from the expressions in Tenti's original papers. This definition differs by a factor of $1/\pi$ from the expressions given by Elliot *et al.* [7, 8].

For our FRS measurements, the optical calibration constant and local laser-beam intensity dependence are removed by dividing all images by a reference FRS image recorded in room-temperature air. For constant-pressure flowfields, this process yields the following expression for the normalized FRS signal,

$$S^* \equiv \frac{S}{S_o} = \frac{T_o}{T} \frac{\sum_k \chi_k \, \sigma_k(T)}{0.21\sigma_{O_2}(T_o) + 0.79\sigma_{N_2}(T_o)} \; , \tag{4}$$

where T_o is the reference temperature (usually 293 K) and σ_k is defined as a temperature-dependent "FRS cross section,"

$$\sigma_k(T) = \left(\frac{\partial \sigma}{\partial \Omega}\right)_k \int_{\Delta\omega_k} \Re_k(\omega; T, M_k) \tau(\omega) d\omega \, . \tag{5}$$

Using the S6 model to calculate the $\Re_k$, and by measuring the filter transmission spectrum, $\tau(\omega)$, temperature and mole fraction were related to S^* via Eq. 4 for analysis of all data to be presented below. It should be noted that the reliability of the experimentally verified S6 model allows Eqs. 4 and 5 to be used to calculate FRS temperature response curves for any specified gas mixture so that no laboratory calibration of the FRS technique is required.

Sample FRS signal curves are shown in Fig. 2. Each curve has been calculated from Eq. 4 for different gas-phase chemical mixtures. Gas mixtures considered include: (1) pure nitrogen, (2) stoichiometric products of methane-air combustion, and equilibrium methane-air products for equivalence ratios of (3) $\phi = 0.7$, and (4) $\phi = 1.3$. The signal curves shown here indicate that local chemical composition can significantly impact evaluated FRS temperatures so that some *a priori* knowledge of the flowfield chemical composition or a measurement of local composition may be required.
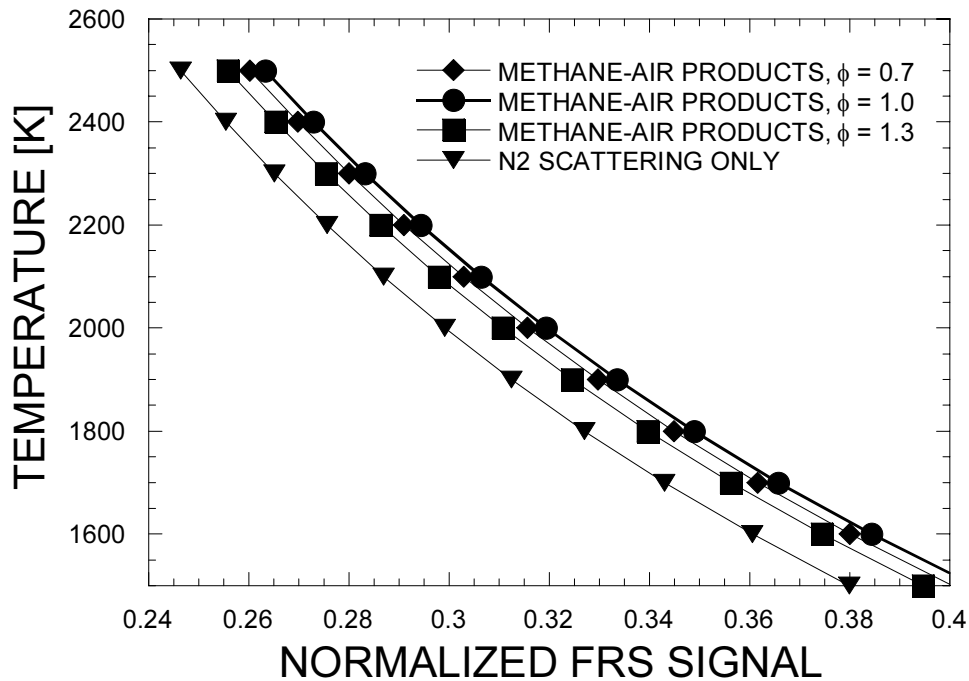
Figure 2 – FRS signal curves calculated for four different gas-phase mixtures at 0.82 atm.

FRS-DGV Velocity Imaging

Descriptions of the specifics of DGV may be found in such references as Elliott and Beutner [25] McKenzie [26], Forkey *et al*. [27] and Meyers [28]. The same fundamental equipment as used in the FRS temperature measurements is utilized for DGV; namely, an injection-seeded Nd:YAG laser, molecular iodine filter cells, and low-light sensitive cameras. In brief, DGV operates by measuring the Doppler shift induced in laser light scattered from small particles traveling with the flow. Figure 3 shows a simplified sketch of the DGV optical principle. The scattered light is observed by both signal and reference detectors, of which the signal detector views the flowfield through a filter cell containing molecular iodine vapor. Iodine has numerous absorption lines in the range of a frequency-doubled Nd:YAG laser, such as those shown in Fig. 4a predicted by Forkey's well-known computer model [27, 29]. If the laser light possesses a suitably narrow linewidth, one of these absorption lines can be chosen to act as a frequency-to-intensity transfer function by selectively absorbing the scattered light dependent upon its Doppler-shifted frequency, as indicated in the experimentally-acquired profile of one absorption
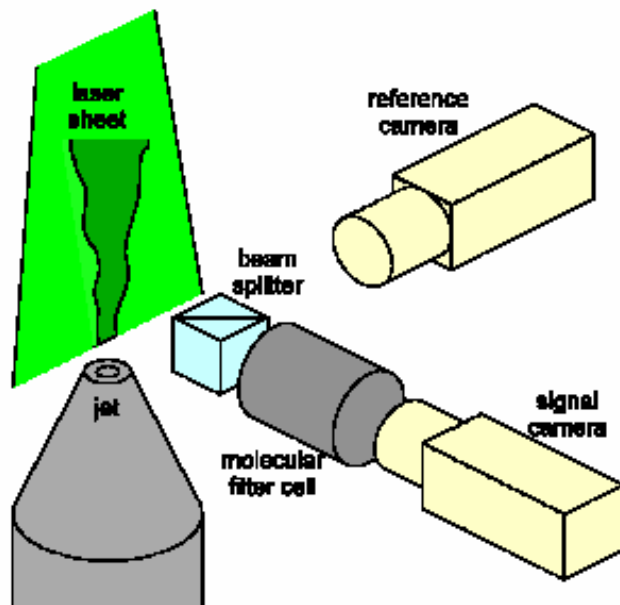
Figure 3 – A sketch of the optical principle of DGV.
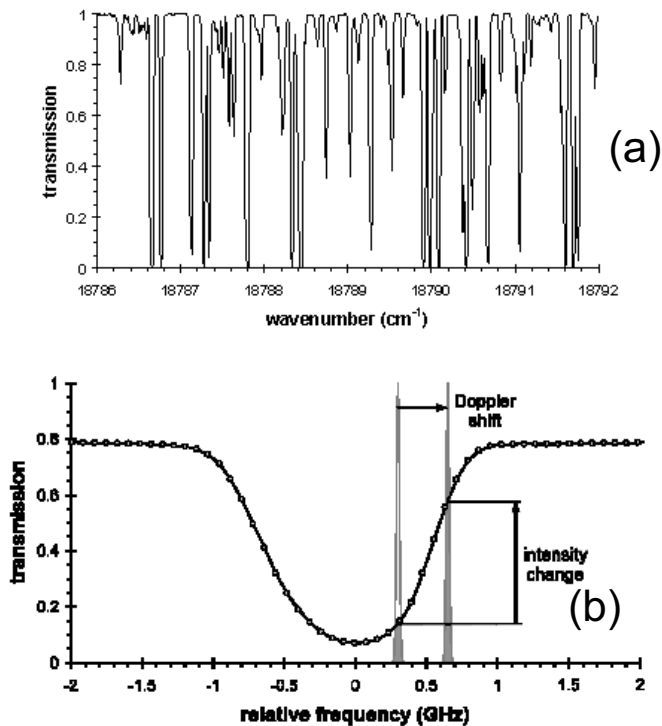
Figure 4 – (a) Iodine absorption spectra in the range of a frequency-doubled Nd:YAG laser predicted by Forkey's computer model [27, 29]; (b) An experimental profile of the line near 18789.3 cm^{-1}, including a sketch of how such a line can be used.

line in Fig. 4b. (The model used to produce Fig. 4a does not include the nonresonant background measured in practice, which accounts for the difference in absolute transmission between Figs. 4a and 4b.) The frequency of the scattered light determines its position along the slope of an absorption line and hence the intensity of the light collected after traversing the cell. Simultaneously, the reference camera collects the scattered light free of filtering. The transmission ratio calculated from the signal and reference data provides a measure of the degree of absorption through the iodine cell, which using Fig. 4b determines the Doppler shift in the frequency and hence one component of the velocity of the flow.

The directional sensitivity of the system is determined from the Doppler shift equation

$$\Delta \nu = \frac{1}{\lambda} \vec{V} \bullet (\hat{s} - \hat{i}) \tag{6}$$

where $\Delta \nu$ is the frequency change due to the Doppler shift, λ is the wavelength of the laser, $\vec{V}$ is the local velocity vector of the jet, and $\hat{i}$ and $\hat{s}$ are the unit normal vectors in the incident and scattered light directions, respectively. This indicates that the directional sensitivity is the bisector of the inverse of the incident light direction and the scattered light direction. To obtain multiple components of velocity in an instantaneous measurement, the scattered light must be observed from multiple directions, which necessitates the use of additional cameras and iodine filter cells. Alternatively, mean velocities may be gathered for multiple components by utilizing multiple laser sheet directions.

SANDIA FRS OPTO-ELECTRONIC SYSTEM

FRS Opto-Electronic System for Temperature Imaging

<u>System Optical Layout</u>
A schematic of the FRS optical arrangement is shown in Fig. 5. The frequency-doubled Nd:YAG laser (Spectra Physics Pro-350) provides an output of 1250 mJ per 10-ns pulse at 10-Hz repetition rate. The Nd:YAG oscillator is injection seeded (Spectra OEM seeder) to provide an essentially single-longitudinal-mode output, with a linewidth of 0.003 cm^{-1}. The output of the laser can be temperature tuned over a nominally ± 1 cm^{-1} range in the vicinity of 18,789.3 cm^{-1} (532.22 nm) by providing a bias voltage to the heater circuit of the Nd:YvO$_4$ seed laser. This tuning capability allows the seeded Nd:YAG output to be matched to line center of a preferred I$_2$
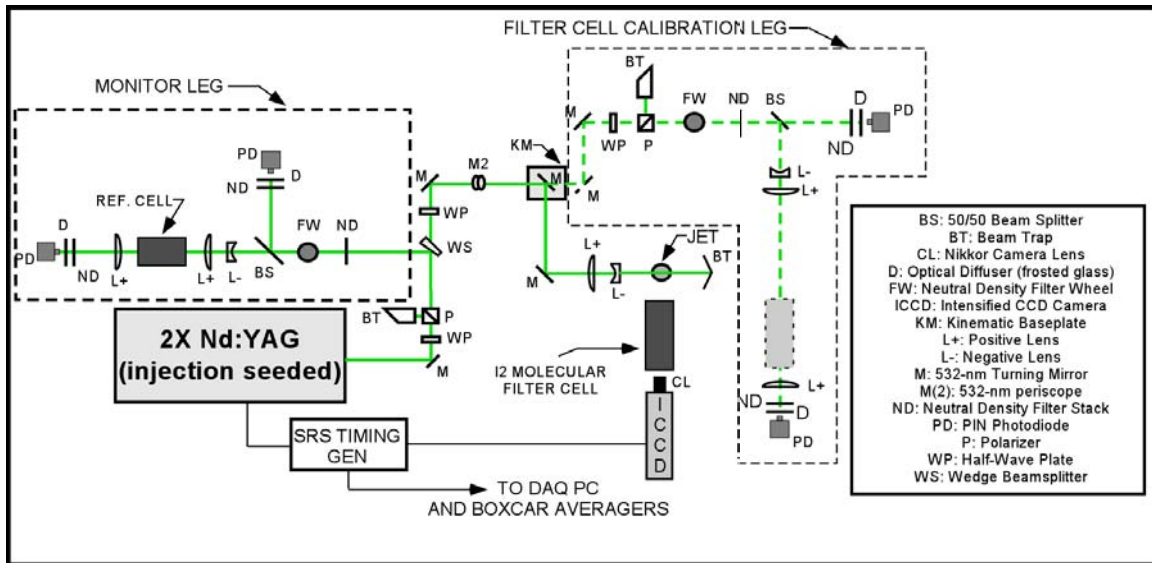
Figure 5 – Schematic of FRS optical arrangement for combustion temperature imaging.

absorption resonance to provide a high level of background rejection for the molecular scattering measurements.

A wedge beamsplitter is used to split 3% of the remaining laser beam to a "monitor leg" that is discussed below. The remaining 97% of the laser beam is passed through a half waveplate that orients the polarization of the laser beam to vertical. The beam is then periscoped to the appropriate height and passed through a $f = +750$-mm spherical lens and a $f = -50$-mm cylindrical lens to form a diverging laser sheet, which travels through the jet flow facility and is then trapped. The waist of the laser sheet is approximately 200 μm wide at the center of the field of view and the laser sheet height is nominally 50 mm. Molecular Rayleigh scattering from the flow is imaged through a 254-mm long, 76-mm diameter iodine cell onto a 16-bit, intensified CCD detector (Princeton Instruments PI-MAX Hi-Q) with a 512×512 square pixel format. The quantum efficiency of the ICCD photocathode is over 45% at 532 nm, which is exceptionally high for an intensified CCD. For the heated jet and CH_4-air premixed flame measurements the filtered Rayleigh signal is imaged at $f/1.8$ using a 50-mm focal length Nikkor glass camera lens. For the CH_4-air driven diffusion-flame and C_2H_4-air sooting premixed flame measurements the filtered signal was imaged at $f/2.8$ with a 105-mm focal length Nikkor lens.

The "monitor leg" is used to track the pulse-to-pulse fluctuations in laser power and drifts in laser-beam frequency that occur during FRS data collection. The monitor laser beam is

attenuated by neutral density filters and split 50/50 using a dielectric plate beamsplitter. One portion of the monitor beam is passed directly to an optical diffuser and PIN photodiode assembly to provide a direct measure of the single-pulse laser energy. The second portion of the beam is passed through a reference iodine cell to a similar diffuser/photodiode assembly. Both photodiode outputs are sampled by gated BOXCAR integrators and the calibrated BOXCAR outputs are ratioed to provide a measure of the transmission of the reference cell. The transmission spectrum of the reference cell is precalibrated so that the measured transmission can be related to the laser output frequency. This reference cell arrangement was used to monitor and correct any long-term drift in laser frequency over the course of the experiments. Pulse-to-pulse frequency variations were generally small compared to the linewidth of the selected I_2 transition and, while monitored, were not accounted for in the analysis of the FRS images.

A third optics train is used to calibrate a second iodine-vapor cell that is used as the molecular filter for the FRS temperature measurements simultaneously with the calibration of the above-mentioned reference iodine cell. For cell calibration, the laser power provided to the experiment is set to a minimum and the turning mirror on kinematic mount "KM" is removed to pass the beam to the "filter-cell calibration leg". In both the reference and calibration legs, the beam is expanded by 4× before entering the iodine cell in order to avoid saturation of any absorption resonances. The cell calibrations are automated using a custom LabVIEW VI that scans the seeder bias voltage and averages the BOXCAR output voltages at each seeder bias. Nominally, 100 laser shots at each bias setting were averaged to simultaneously produce transmission spectra for both the reference cell and molecular filter cell. The VI also monitors a voltage from the seed-laser control circuit which is proportional to the build-up time for the Q-switched laser pulse in the Nd:YAG oscillator. Exceptionally long buildup times indicate momentary loss of seeder lock and the data from these pulses are not included in the average. This voltage was also used to monitor seeder lock during all FRS experiments and images with poor injection seeding can be similarly discarded.

Iodine Filter Cells

The molecular iodine cells used to monitor the laser frequency and to filter the Rayleigh signal are of the starved-cell design described by Elliott and Beutner [25] . Each cell is a 76-mm diameter glass cylinder with optically flat windows on each end. In the starved-cell arrangement, each cell contains essentially pure I_2 vapor that is superheated to 100^oC by kapton resistance

heaters on the cell sidewalls. Superheating of the cell walls ensures that none of the vapor inside the cell condenses back to the solid phase so that a constant I_2 number density is kept in the cell. The reference cell is 127 mm in length and permanently sealed for enhanced longtime stability with a nominal I_2 saturation temperature of 35^oC. The molecular-filter cell is 254 mm in length and has valved ports to a vacuum line and a temperature-controlled I_2 crystal reservoir so that the amount of I_2 in the cell can be varied if desired. For the experiments reported here the I_2 saturation temperature for the molecular filter is 45^oC, with the exception of the premixed, sooting C_2H_4-air flame where a saturation temperature of $\sim53^oC$ was used to make the cell as optically thick as possible. The molecular filter has a longer length and higher I_2 concentration relative to the reference I_2 cell so that the maximum level of background rejection is provided in the Rayleigh images in conjunction with a reliably measured, nonzero transmission minimum for frequency tuning of the injection seeder.

For all of the reported temperature measurements, the laser output was tuned to line center of the R121 (35-0) transition of the $B(0^+u^3\Pi) \leftarrow X(0^+g^1\Sigma)$ electronic system of I_2 near 18789.25 cm^{-1}. Calibration data in the vicinity of this line for both the reference and molecular filter cells are shown in Fig. 6. The long-time stability of the molecular-filter cell, which has not been permanently sealed, is noteworthy.
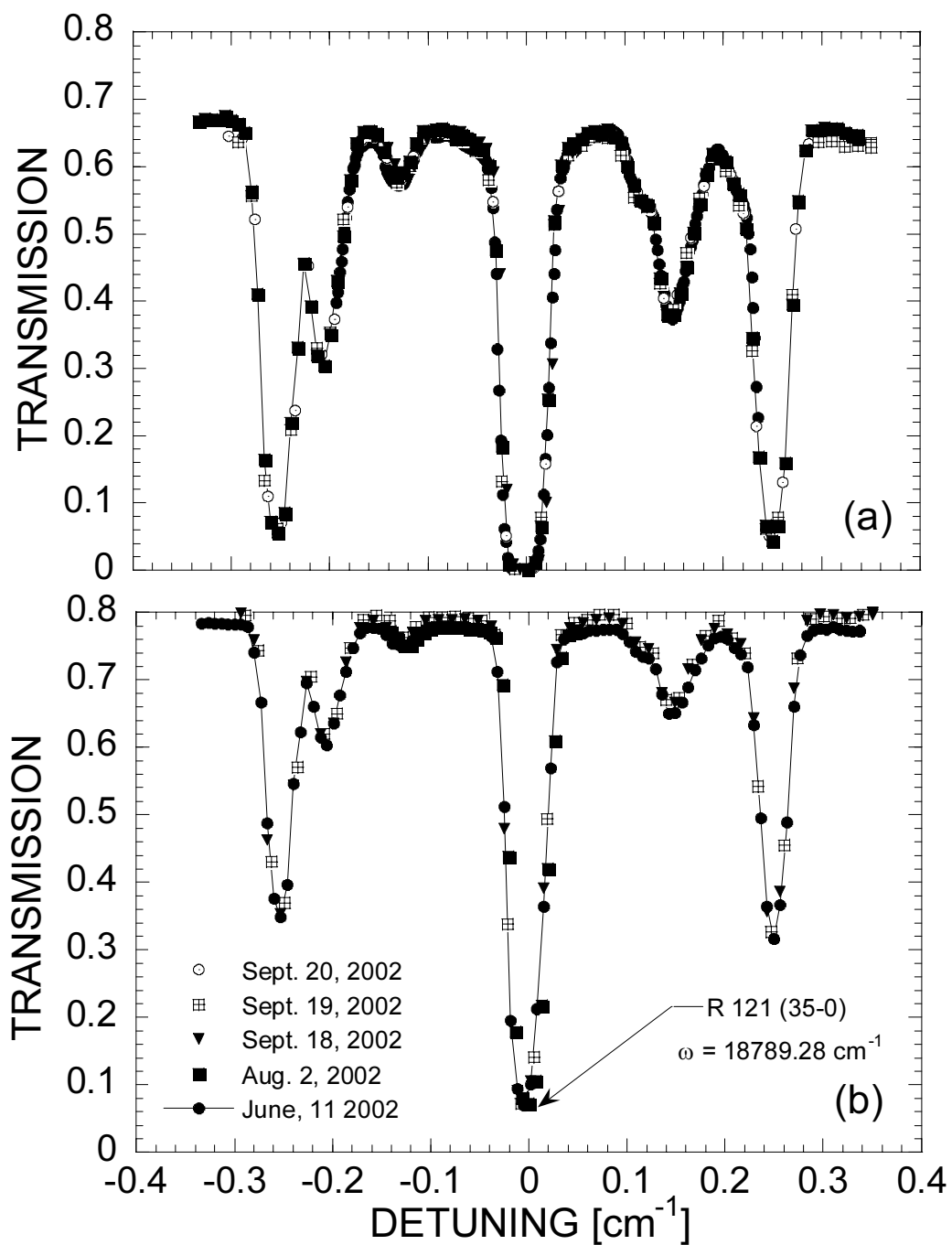
Figure 6 – Measured transmission spectra for (a) molecular-filter cell and (b) reference iodine cell. The stability of both the adjustable cell in (a) and sealed cell in (b) is noteworthy.

FRS Opto-Electronic System for Aeroscience Velocity Imaging

Optical Arrangement

    The DGV system was designed and assembled in conjunction with the planar thermometry instrument described earlier in this document, and in fact it utilizes much of the same equipment and techniques. A schematic of the optical setup is drawn in Fig. 7 and a photograph of the experiment is shown Fig. 8. Its centerpiece is an injection-seeded pulsed Nd:YAG laser (Spectra Physics PRO-350) operating at its second harmonic of 532 nm. The frequency of the beam is controlled by an external voltage supplied to the seeder, but the laser is subject to substantial jitter and occasional hops in frequency even when the voltage is constant, so a frequency monitor must be used to record such frequency changes on a pulse-to-pulse basis. A small portion of the beam is tapped off by a beamsplitter, reduced in intensity by ND filters, and beam-split once more. One of these beams is directed to a ground-glass plate and viewed by a photodiode to monitor the pulse-to-pulse beam energy, while the other is passed through an iodine cell prior to being intercepted by a second glass plate and photodiode. The beam is expanded upstream of the iodine cell such that a larger beam traverses the cell to avoid saturating the iodine vapor, then is refocused on the glass plate. The iodine cell, supplied by Innovative Scientific Solutions Inc. (ISSI), is permanently sealed after filling at a side-arm temperature of 35°C and maintained at a cell temperature of 100°C to within ±0.1°C by a digital temperature controller (Cole-Parmer DigiSense). It is 12.7 cm long and 7.6 cm in diameter.

    A second iodine cell is used for the signal camera viewing the jet and is calibrated simultaneously with the iodine cell in the frequency monitor. To accomplish this, an additional portion of the laser beam may be tapped off the primary beam and redirected to a second calibration station identical to the frequency monitor. This beam is split into a reference beam observed by one photodiode and a signal beam that is expanded, collimated through the second iodine cell, and refocused on a ground glass plate observed by another photodiode. This calibration station and the frequency monitor function identically and in parallel when scanning the absorption profile of the two iodine cells.

    The four photodiodes used in the frequency monitor and the calibration station are each sampled by a gated integrator (Stanford Research Systems SR250) to determine the energy found in each laser pulse. The integrated signals then are recorded by an analog-to-digital converter
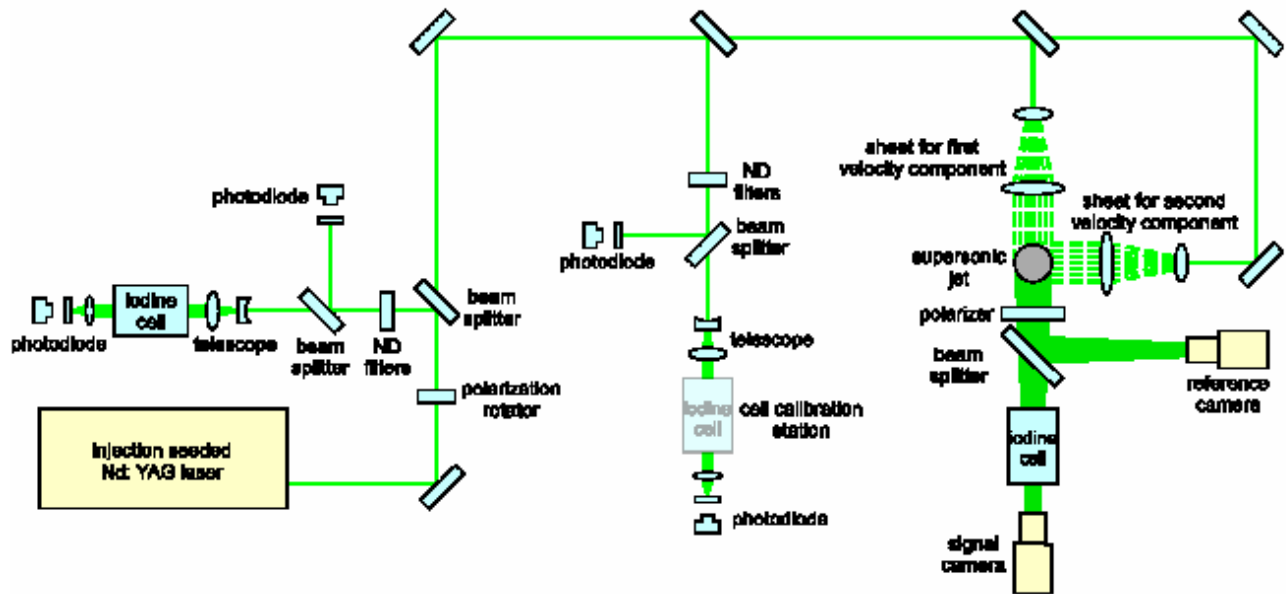
Figure 7 – A schematic of the optical configuration of the DGV system.
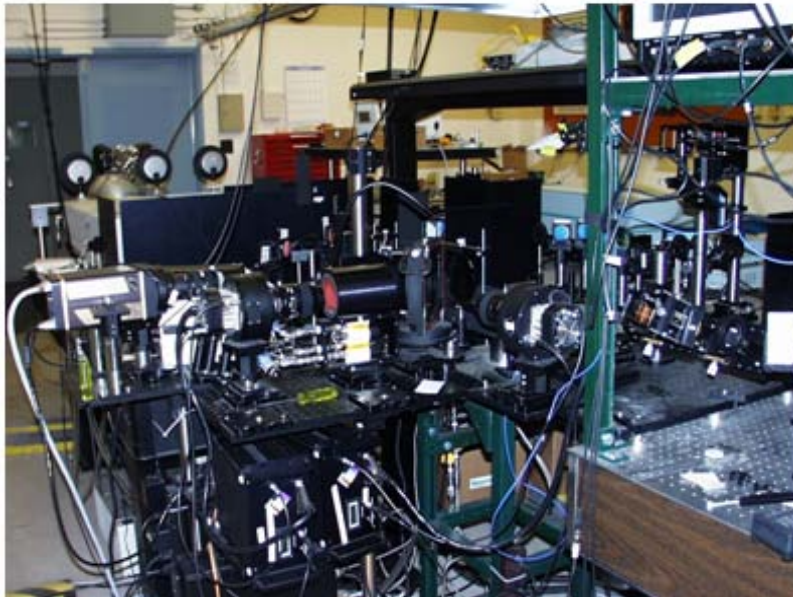
Figure 8 – A photograph of the optical configuration of the DGV system.

controlled by LabView 6.0 software. Simultaneously, the laser's Q-switch build-up time monitor is sampled to ascertain the quality of the injection seeding; data points at which the laser loses its frequency lock and emits a multi-mode pulse can be identified by a higher voltage from this monitor and are discarded. Simultaneous triggering of the laser, the gated integrators, and LabView is maintained by multiple digital delay generators (Stanford Research Systems DG535).

The primary beam is formed into a sheet and re-collimated to ensure that no significant divergence in the incident light direction occurs over the span of the laser sheet. It is deflected down towards the jet at an angle of 27° from the vertical, as shown in Fig. 9a. The cameras are positioned in the horizontal plane. The directional sensitivity of the system is determined as the bisector of the inverse of the incident light direction and the scattered light direction, or a 31.5° angle from vertical in the scattering plane as shown in Fig. 9a. Thus the velocity component measured is primarily sensitive to the jet axial direction, but retains some sensitivity to the radial direction as well. This laser sheet orientation was chosen to maximize its sensitivity to the axial velocity component without the laser sheet striking the jet nozzle, which was found to create biases from the light reflection off the surface, while still remaining near the exit of the jet.

A second velocity component can be obtained within the same plane and using the same camera alignment by directing the laser sheet from the side, but still inclined with respect to the jet axis by 27°. This is shown in Fig. 9b. The laser sheet is carefully aligned to coincide with the semi-vertical laser sheet of Fig. 9a, although of course only one sheet is operational at a time when data are gathered. The side sheet configuration yields a velocity sensitivity in the horizontal plane at 45° from the scattering direction, as shown. Thus two-component mean velocity data may be acquired for the jet.

Collection Optics

Light scattered from the jet is divided by a pellicle beam splitter and then collected by a pair of scientific-grade back-illuminated CCD cameras (PixelVision SpectraVideo) with a 512 × 512 array sampled at 16 bits. The cameras are thermo-electrically cooled for low noise performance and hence increased sensitivity. Each is equipped with Nikon 105 mm lenses operating at an f-stop of f/8 to allow sufficient depth of field to focus the inclined laser sheet. Prior to reaching the beamsplitter, the scattered light passes through a polarizer to remove the effects of any
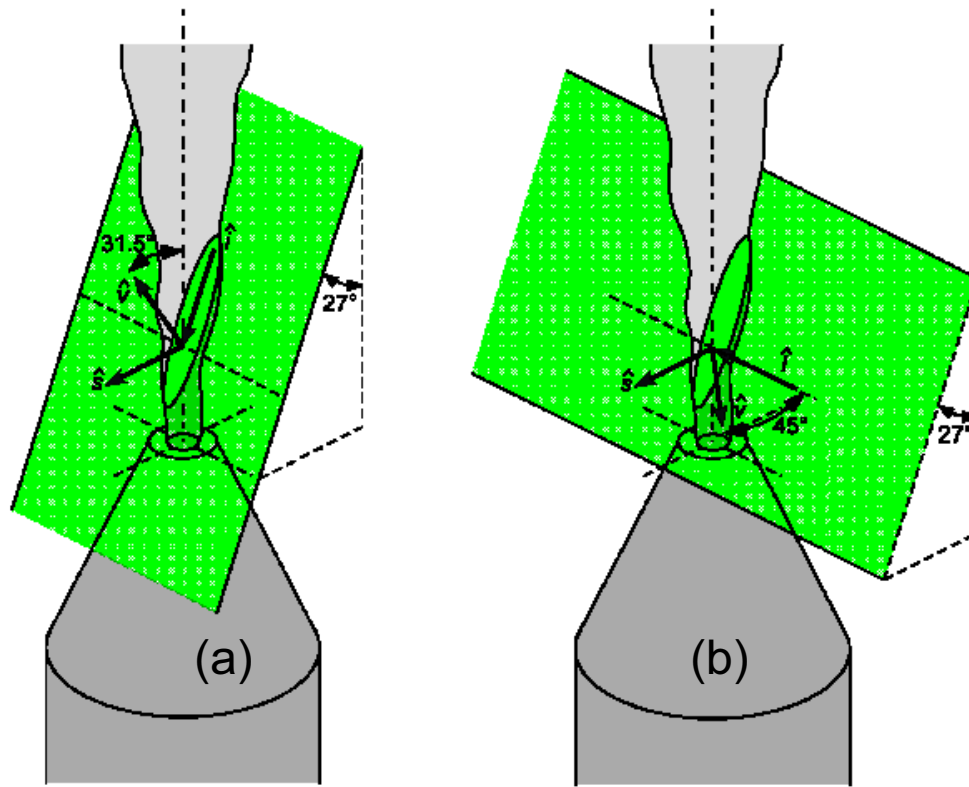
Figure 9 – Schematic of the laser sheet position relative to the jet and the resulting directional sensitivity of the velocity measurements. $\hat{i}$ and $\hat{s}$ are the unit normal vectors in the incident and scattered light directions, respectively, and $\hat{v}$ is the direction of the resulting velocity sensitivity. (a) Velocity measured principally in the streamwise direction; (b) Velocity measured in the radial direction.

polarization differences between the calibration procedure and data collection. This is critically important because the camera calibration (see below) is conducted while illuminated with laser light at a different polarization than that used to collect data, and the pellicle beamsplitter ratio is highly dependent upon the polarization of the incident light. The polarizer ensures that the pellicle and the cameras observe the same polarization of scattered light regardless of any prior polarization effects.

One of the cameras looks through an iodine filter to provide the signal image while the other has no filter and thus serves as the reference image. The iodine cell, a starved-cell design purchased from ISSI and based upon the design of Elliott *et al.* [30] typically was pressure-broadened with 50 torr of nitrogen and sealed at a side-arm temperature of 45°C. The cell-body

temperature was maintained at 100°C using a second temperature controller (also Cole-Parmer DigiSense). Introduction of nitrogen as a buffer gas increases the absorption line width to provide a useful gradient to the line found at 18789.3 cm^{-1} for the Mach 3.7 velocity measurements. The iodine crystals are located in the cell side-arm and hence control of this temperature dictates the iodine vapor pressure in the cell. The side-arm was immersed in a temperature-controlled bath of a water-glycol mixture to maintain the desired conditions until the side arm was sealed. The starved-cell design allows the cell's side-arm and its remaining iodine crystals to be isolated from the cell body and therefore eliminates the need for constant control of the side-arm temperature, which requires greater precision than the cell-body temperature to maintain a constant absorption profile.

Jet Hardware

The supersonic jet is produced by a conical nozzle with a design Mach number of 3.73 and an expansion half-angle of 15° that reaches an exit diameter of 6.35 mm (0.250 inch). The nozzle connects to a large settling chamber containing a pressure transducer and a thermocouple to measure the stagnation conditions of the jet flow. The settling chamber is supplied by a 24 MPa (3500 psi) bottle of nitrogen controlled by a dual-stage pressure regulator to maintain the stability of the flow. In all cases presented in this document, the jet was operated at a stagnation pressure of 1.41 ± 0.01 MPa (205 ± 2 psia) and a stagnation temperature of 293 ± 3 K, exhausting into ambient room air at 84.1 kPa (12.2 psia). At these conditions, flow separation will occur within the nozzle, with a predicted shock location 2.7 mm (0.11 in) upstream of the exit plane [27].

A condensate fog was created in the jet flow to serve as a scattering medium for the laser light. Ethanol was injected into the nitrogen line as it approached the settling chamber by an air atomizing nozzle; this ethanol evaporated into the nitrogen supply and then condensed during the expansion process in the jet nozzle to form a fine fog of ice crystals, which is an ideal scattering source for the incident laser light. The stability provided by the dual-stage regulator was found to be necessary to avoid saturating the flow with excess quantities of ethanol when the jet stagnation pressure might briefly decline. The ice crystals were estimated to have a diameter of approximately 100 nm by imaging the jet flowfield at two different incident laser light

polarizations and comparing the resulting polarization ratio with Mie scattering theory [31], this is sufficiently small to track the flow well [11].

FRS TEMPERATURE IMAGING MEASUREMENTS

FRS Image Preparation for Combustion Thermometry

Single-pulse FRS images were generally acquired in groups of 100 or 200 for each operating condition studied. In addition to the FRS thermal images, a reference image set in room-temperature air was obtained and the shot-averaged FRS air image was used to normalize all data so that the experimental data was consistent with the analysis of Eq. 4. An additional FRS image in pure Helium at room temperature was also acquired to estimate the degree of background light leakage past the filter. These background levels were small (typically less than 5% of the FRS signal) but significant enough to impact the results if not monitored. Helium was selected as the background reference because it has a Rayleigh cross section that is 73 times less than the cross section of air. The air and helium FRS images are then combined to solve for the background contribution utilizing an expression similar to the one first presented for LRS by Fourgette *et al.* [1],

$$B_{i,j} = H_{i,j} - \frac{\sigma_{He}}{\left(0.79\,\sigma_{N_2} + 0.21\,\sigma_{O_2} - \sigma_{He}\right)}\left(A_{i,j} - H_{i,j}\right) \quad . \tag{7}$$

In Eq. 7, i and j are the ICCD pixel indices, B is the shot averaged background light estimate, A is the shot-averaged FRS image in room-temperature air and H is the shot averaged FRS image in room-temperature helium. The second term on the RHS of Eq. 7 represents the subtraction of the Helium FRS contribution from the total image H, which includes the helium FRS signal plus the background noise.

Normalized FRS signals for use in curves like those shown in Figs. 1c and 2 are then computed from the single-pulse or shot-averaged FRS images, $F_{i,j}$, using,

$$S_{i,j}^* = \frac{F_{i,j} - B_{i,j}}{A_{i,j} - B_{i,j}} \quad . \tag{8}$$

FRS temperature data are then obtained from 4th-order polynomial fits to the FRS temperature response curves for the appropriate gas-mixture composition for each pixel in the image.

Temperature Imaging in a Heated Air Jet

Our initial sets of FRS temperature imaging experiments were performed in a heated air jet. Measurements in the nonreacting heated jet removed the complexities in data interpretation that arise in reacting flows due to gas-composition dependent variations in the local Rayleigh cross section. The jet was constructed from an approximately 1-m long section of 15.2-mm diameter stainless-steel pipe. A Sylvania electric torch was placed inside the entrance to the pipe at a sufficient distance upstream of the jet exit so that any disturbances due to the presence of the heater were damped out and a fully developed laminar pipe flow emerged from the jet. The electric torch provided a jet exit temperature of 800 K, measured using a thermocouple, with a jet flow of 6000 SLPM. These conditions resulted in a jet Reynolds number of 180 and a jet Richardson number of 1.3. Under these conditions the jet was near-field stable, laminar and in a mixed forced-free convection mode. This stable jet was useful for FRS system-evaluation purposes because it had a large, isothermal core region, which was at the jet-exit temperature.

Time-mean and single-laser-pulse FRS temperature data from the stable calibration jet are shown in Fig. 10. The in-plane spatial resolution in these temperature images is 160 μm $\times$ 160 μm, with an out-of-plane resolution dictated by the local laser-sheet thickness of approximately 200 μm. The time-mean results in Fig. 10a were obtained by averaging 200 single-pulse temperature images, and this mean field shows the extent of the uniform-temperature jet core. The single-pulse temperature field in Fig. 10b exhibits more noise (primarily intensifier MCP and photon shot noise) than the averaged temperature field and shows the impact of instantaneous jet structure caused by a sinuous-wave instability that is clearly evident at $z = 50$-60 mm or 3.3 to 4.0 jet diameters.

Radial and axial profiles extracted from the time-mean temperature image in Fig. 10a are presented in Fig. 11. The radial profiles presented in Fig. 11a for z from 1.2 to 3.7 jet diameters were selected from the stable region of the jet, and all radial profiles exhibit the expected near-Gaussian shape with no significant jet spreading and some scatter in the maximum centerline temperature. This scatter in jet core temperature is indicative of the bias error in the FRS measurements due to imperfect background noise subtraction and laser-sheet profile

normalization. An estimate of this bias can be obtained from the axial profiles of jet core temperature shown in Fig. 11b, which exhibit a mean core temperature of 816 K with an rms scatter of 10.7 K. Similar calculations in room air exhibit the same levels of scatter and a 95% confidence interval for precision of the shot-averaged air-jet data is approximately 2 rms deviations or ± 20 K.
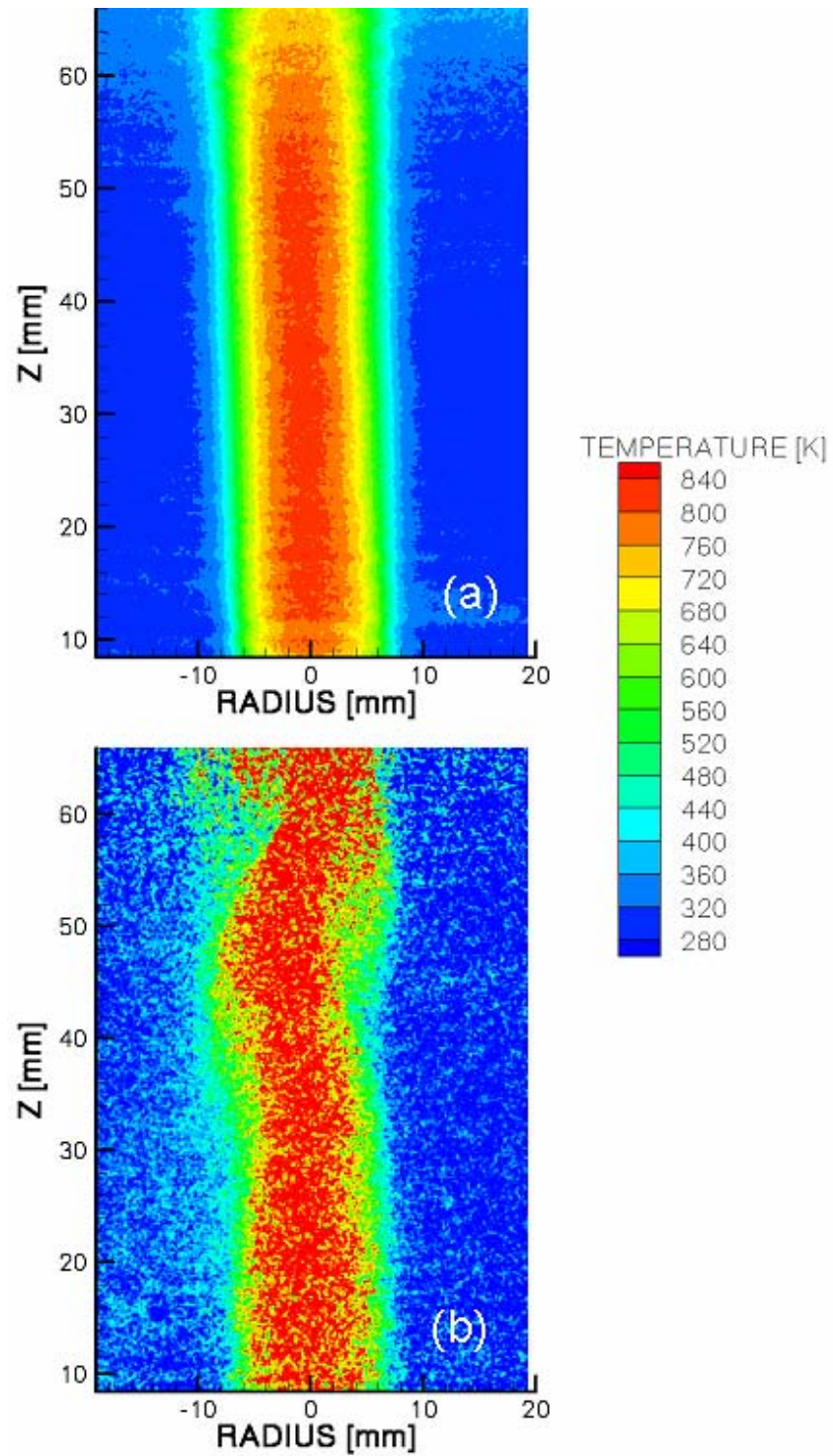
Figure 10 – Time-mean averaged for 200 laser shots (a) and single-laser-pulse (b) FRS temperature image from a stable hot-air calibration jet.
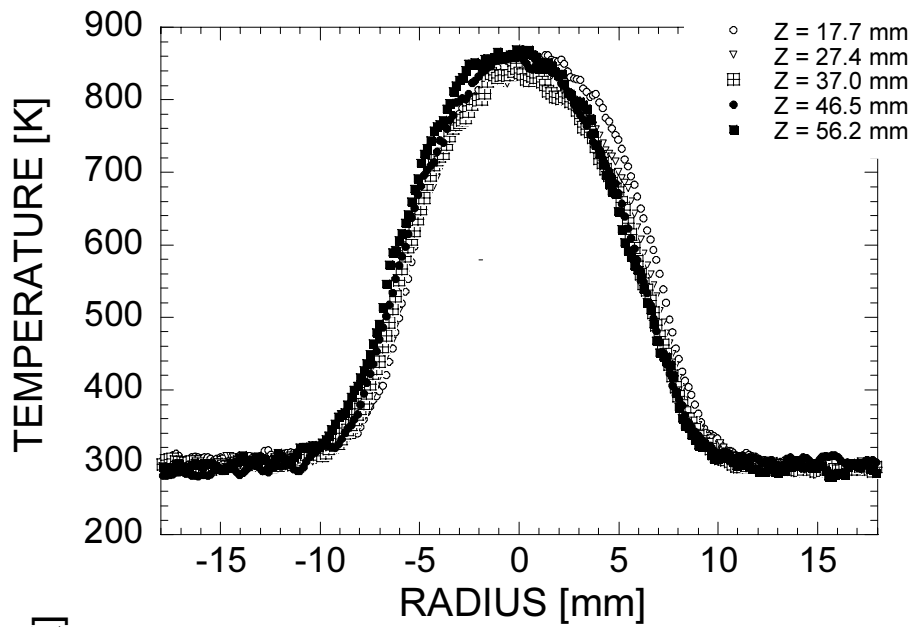
(a)
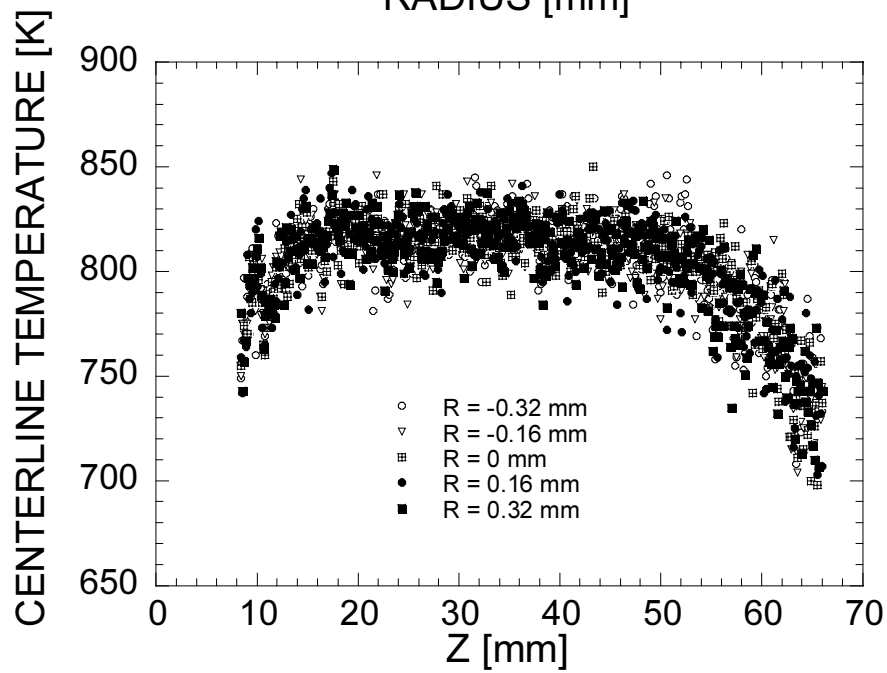
(b)

Figure 11 – Radial (a) and axial (b) temperature profiles from the stable hot-air calibration jet.

Temperature Imaging in a Premixed Flat Flame

As a first step toward applying our FRS instrument for combustion thermometry, we have mapped the temperature field in the premixed CH_4-air flame provided by a Hencken burner. The Hencken burner consists of a fine array of hypodermic fuel tubes embedded in a 50.8-mm square honeycomb matrix, through which dry air flows. The air rapidly mixes with the CH_4 fuel near the burner surface and, when the gas flow rates are sufficiently high, this arrangement results in a stable, near-adiabatic flat flame that is slightly lifted off the burner substrate. Time-mean (100-laser-pulse average) and single-pulse FRS temperature fields recorded in the post-reaction combustion products of the flat flame are shown in Fig. 12. The images in Fig. 12 clearly show that this flame provides a uniform-temperature region of products, which can be used to test the reliability of our FRS instrument for measurements in reacting flows. It should be noted that these premixed flame measurements were performed in an open lab with no coflow shield and without precautions to mitigate room particulate, which would not have been possible with conventional linear Rayleigh scattering methods.

We have obtained three FRS data sets from the Hencken burner. In the first two data sets the house-air flow rate was set to 40 SLPM and the methane flow was varied from 3.0 to 5.6 SLPM. A third FRS data set was recorded with higher flow rates, with 50 SLPM of air and 4.0 to 7.1 SLPM of methane. For these FRS experiments, the equivalence ratio, ϕ, varied from 0.71 to 1.34. For comparison, several sets of coherent anti-Stokes Raman scattering (CARS) temperature measurements were also performed with 40 SLPM air flow for ϕ from 0.86 to 1.36. The CARS measurements were performed at the Combustion Research Facility at Sandia/CA[†] while the FRS measurements were conducted at Sandia/NM. The barometric pressure difference between Livermore, CA and Albuquerque, NM was not expected to impact flame thermodynamics. This assumption was checked using adiabatic equilibrium calculations [32] for pressures of 1.0 and 0.82 atm, where the results showed less than 5 K change in the predicted flame product temperature.

FRS-measured flame temperatures were calculated for each ϕ from time-mean temperature images by averaging the mean temperatures within a 7.3 × 11 mm interrogation zone within the uniform-temperature region of the flame. The flame temperature data obtained are plotted in

---

[†] The authors wish to thank Paul Schrader and Roger Farrow of the Combustion Research Facility for their acquisition of all CARS measurements reported here.

Fig. 13. The FRS temperatures shown in Fig. 13a were inferred from the normalized FRS data using Eq. 4 and equilibrium product mole fractions for major species N_2, O_2, CO, CO_2, and H_2O, calculated from the NASA equilibrium code [32] for each value of ϕ. For the range of stoichiometries investigated, these 4 major species accounted for 95 to 98% of the total gas-phase mixture. The balance was added to the N_2 mole fraction for FRS data analysis. Using this procedure for estimation of local product composition, the FRS results for $\phi < 1.3$ deviated by no more than 50 K from the adiabatic flame temperature. For comparison, the average of several sets of CARS measurements are shown in Fig. 13a. The uncertainty in the CARS data is ±25 K. The CARS temperatures are nominally 25-50 K less than the adiabatic flame temperature for all ϕ, which is generally a result of low-levels of heat loss from the flame. FRS temperatures in Fig. 13a for $\phi < 1.3$ are generally within 50 K of the CARS results as well. For $\phi > 1.3$, the FRS temperatures are nominally 50 K higher than the adiabatic flame temperature and 75-100 K higher than the CARS measurements for all three FRS data sets. The reason for this apparent high-temperature bias in the FRS results at high ϕ is not understood at this time. One possibility is that at these fuel-rich operating conditions there is an ever-increasing concentration of H_2O in the combustion products and that potentially imperfect S6 modeling of H_2O is having a greater impact on interpretation of the FRS results.

For many practical measurements, the local chemical composition in flames is generally not as well understood as for the case of the Hencken burner. For premixed methane-air flames, the bulk of the gas species is nitrogen and an often-made simplifying assumption is that all the Rayleigh scattering results from N_2. Another potential simplification is to use a single methane-air equilibrium product composition for analysis of the results. We have used the FRS data from the Hencken burner to investigate the accuracy of these simplifying assumptions. The FRS images were analyzed assuming: (1) all of the FRS signal comes from N_2, and (2) using the stoichiometric ($\phi = 1$) product composition to analyze the data for all ϕ. The results are shown in Fig. 13b. FRS flame temperatures calculated using the N_2 scattering assumption result in a significant low-temperature bias in the results; with N_2-FRS temperatures as much as 150 K lower than the CARS measurements. Use of the stoichiometric product assumption results in a significant improvement in FRS flame temperatures as the FRS temperatures for ϕ from 0.8 to 1.2 are generally within 50 K of the curve traced by the CARS measurements. The reason for the larger discrepancy in the N_2-scattering assumption is believed to be the neglection of CO_2

38

scattering, which has a Rayleigh cross-section that is about 2.2 times greater than for N_2. The fact that CO_2 is even included in approximate amounts by using the $\phi = 1$ products assumption results in much more accurate flame temperatures over a broad range of stoichiometries. Outside of the equilibrium-product zone, both simplifying assumptions result in some degree of bias error due to uncertainty in the local chemical composition. However, the absolute temperature bias decreases at lower temperatures, such that it is nominally +50 K at most at room temperature even when assuming a stoichiometric product composition for premixed flame measurements.
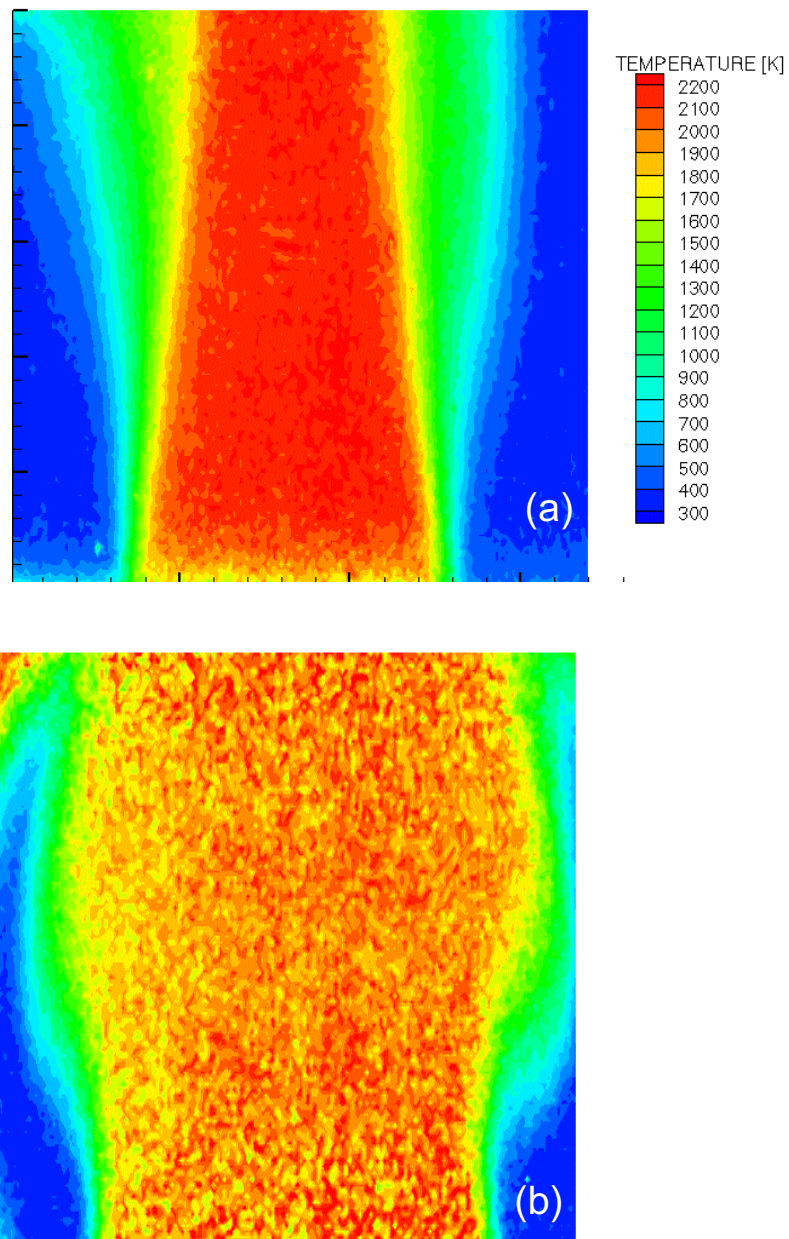
Figure 12 – Time-mean (a) and single-laser-pulse (b) FRS temperature images from the combustion-product region of the premixed methane-air flame provided by a Hencken burner for an equivalence ratio of $\phi = 1$.
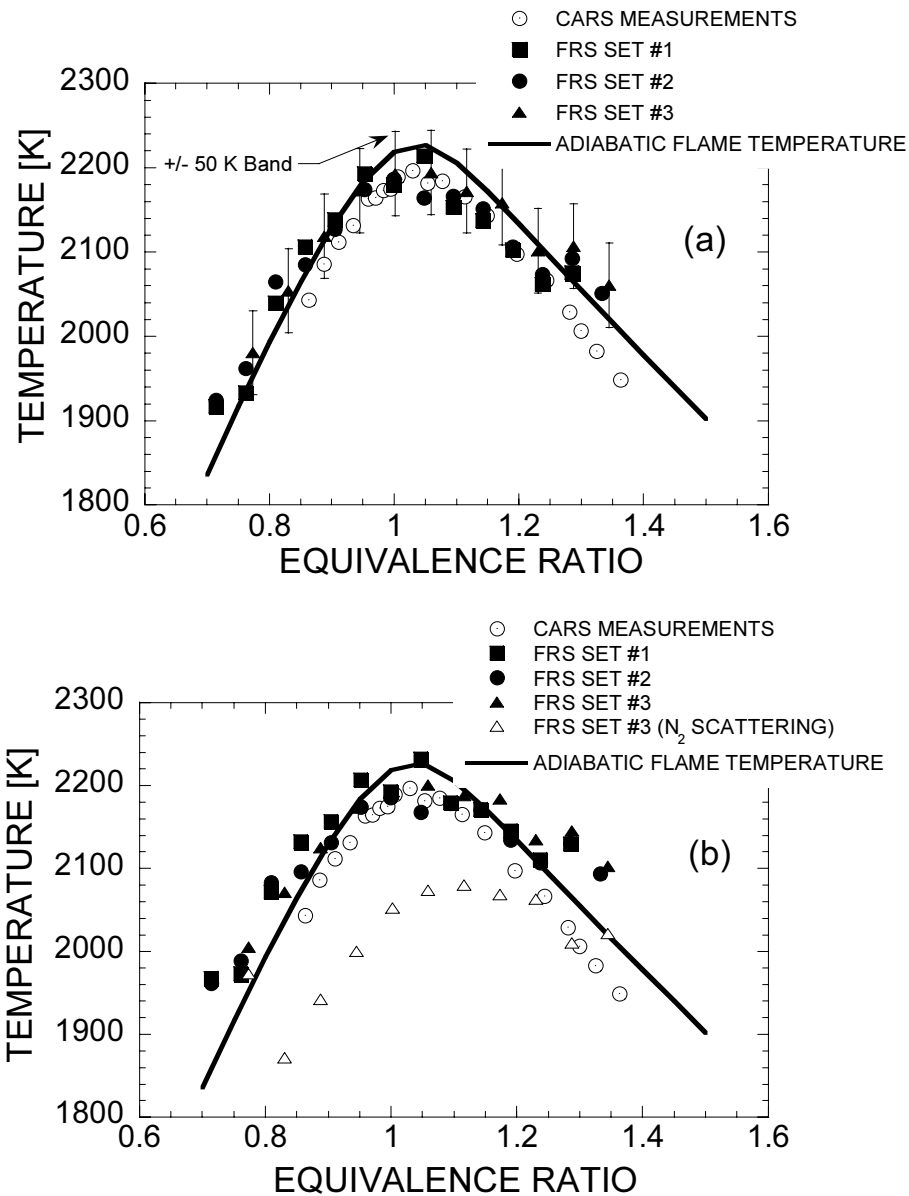
Figure 13 – Comparison of FRS- and CARS-measured flame temperatures from the Hencken burner and the calculated equilibrium product temperature for varying fuel-air stoichiometries. Part (a) shows the FRS temperatures deduced by using the calculated major product mole fractions. In part (b) the same FRS data have been reanalyzed using the following simplifying assumptions: (1) all FRS signal results from N_2 scattering and (2) all flames are stoichiometric.

An even greater diagnostic challenge is to utilize our FRS instrument for measurements in diffusion flames, whose nonpremixed nature often results in larger deviations in the local Rayleigh cross section than for the case of premixed combustion. We have utilized FRS in conjunction with time-averaged Raman scattering measurements of local fuel mole fraction to image the temperature field in a two-dimensional diffusion flame that is interacting with a vortical flowfield. The laminar flame was stabilized on a Wolfhard-Parker slot burner of the type utilized by Smyth and coworkers [33]. The burner facility is shown schematically in Fig. 14 and is briefly described here. More details of the facility are reported by Mueller and Schefer [34], who report OH PLIF measurements in this facility. The burner consists of an 11-mm wide by 80-mm long fuel slot through which a 33% CH_4, 67% N_2 fuel stream flows at a rate of 45.3 SLPM (0.86 m/s). The CH_4 fuel stream was diluted with N_2 to suppress soot formation. The fuel slot is surrounded by a 150-mm square honeycomb matrix, which is covered with several flow-conditioning screens through which an air coflow at 235 SLPM (0.18 m/s) is provided. A two-dimensional symmetric flame structure is produced with identical flame sheets located in the mixing layers adjacent to the fuel jet. The fuel stream is periodically forced by a pair of loudspeakers placed in the fuel-supply duct. This facility produces a laminar, repeatable vortex flame interaction that is amenable to phase-locked laser measurements. We have investigated two forcing frequencies: (1) a 7.5-Hz case where a single vortex stretches the flame zone followed by a long period where the flame is relaxed back to an unforced reference state and (2) a 90-Hz case where two consecutive vortices interact and lead to a local strain-induced extinction of the flame. These vortex-strained diffusion flames supplied a controlled environment that was useful for FRS diagnostic development, while still providing a sufficiently complex flowfield to push the diagnostic to its limits.

Use of Fuel Raman Images for Correction of Local Rayleigh Cross Section

As previously mentioned, the FRS cross section in flames can vary significantly with changes in local chemical composition. For the premixed flames discussed above, we found that cross-section variation is not a critical factor if an approximate gas-mixture composition is used in the interpretation of the FRS data using Eqs. 4 and 5. Diffusion flames can present a much bigger challenge if the cross section of the fuel stream differs significantly from air. For the 67/33 N_2/CH_4 fuel-stream mixture employed in the diffusion-flame experiments, the fuel-stream
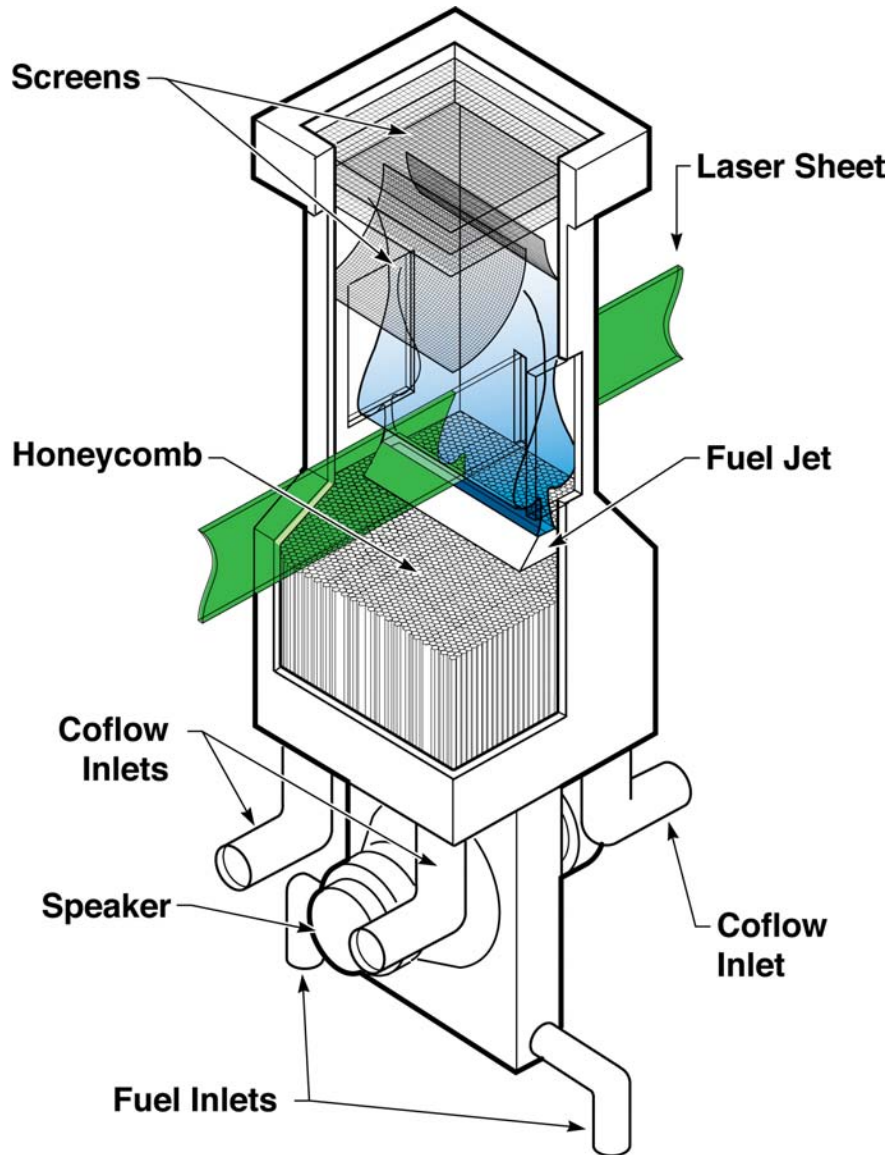
Figure 14 – Schematic of Wolfhard-Parker slot-flame burner used for FRS and CARS driven diffusion flame measurements.

FRS cross section (calculated from Eq. 5) is 1.65 times greater than for air at 300 K. The impact of such large variations in Rayleigh cross section is quantified in Fig. 15, where we have calculated FRS temperature response curves for air (79/21 N_2/O_2), the 67/33 N_2/CH_4 fuel stream, and stoichiometric products of CH_4-air combustion. These FRS "calibration" curves show that bias errors as large as 1000 K can result from a fuel-stream FRS cross section that is 65% larger than air at 300 K.
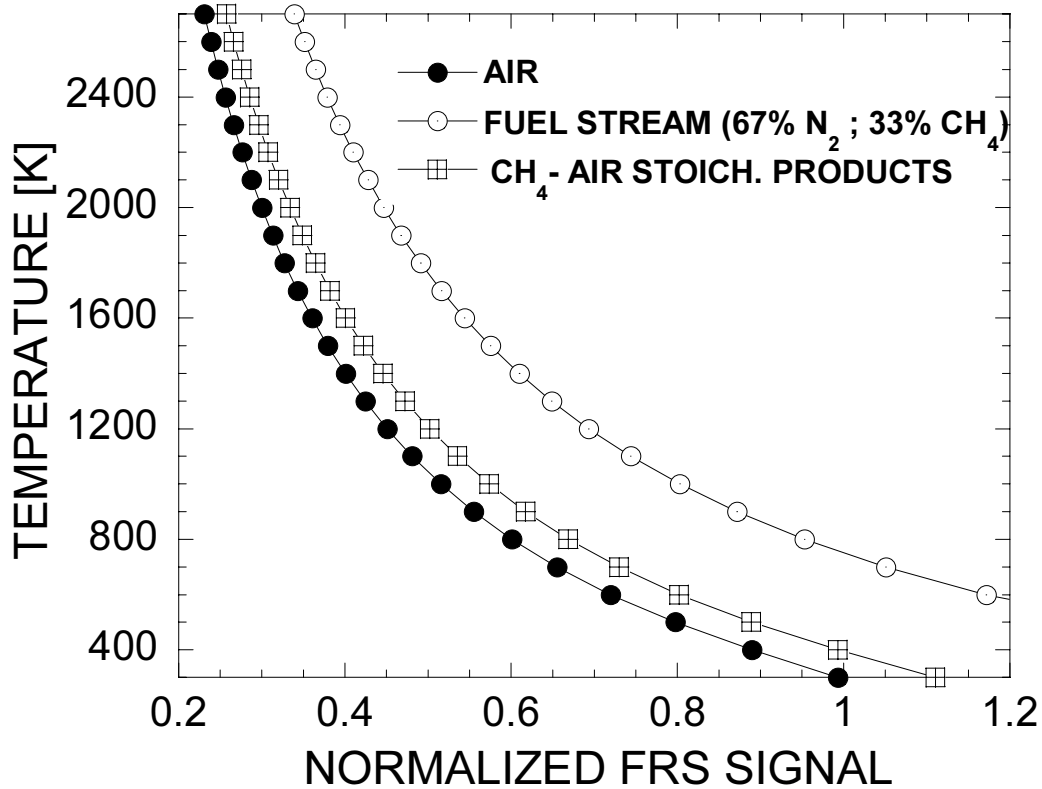
Figure 15 – FRS temperature response functions for fuel-stream, air, and methane-air combustion products.

To correct the FRS images for such large changes in scattering cross section, Raman-imaging measurements of the local number density of the CH_4 fuel molecule were performed. The Raman data were acquired using the same optical system and ICCD detector used for FRS with the I_2 molecular filter replaced by a with a 633-nm center, 10-nm bandwidth laser-line interference filter. This interference filter attenuated the Rayleigh signal by a factor of 10^5 and passed the Raman Q-branch signals arising from the symmetric and asymmetric stretch modes of CH_4 near 15,847 cm^{-1} (633 nm) and 15,780 cm^{-1} (629 nm). The difficulty associated with weak Raman signal strengths was overcome by our high laser-sheet fluence and by averaging the Raman signal for 200 laser shots, which was possible in the repeatable laminar flame system investigated. The Raman images were corrected for the laser sheet profile and scaled using a calibration Raman image obtained from a room-temperature fuel stream. Raman signal-to-noise was further enhanced by smoothing along the contours of the much stronger FRS signal using the method demonstrated by Starner *et al.* [35]. This smoothing method exploits the high degree

of correlation between the Raman and Rayleigh signals and allows for improved signal-to-noise without significant alteration of gradients in the measured fuel number density. The local CH_4 fuel mole fraction was computed from the processed Raman signal using,

$$\chi_{i,j}^{(f)} = R_{i,j} \frac{T_{i,j}}{T_{ref}} g\left(T_{i,j}\right) \; , \tag{9}$$

where i and j are the ICCD pixel indices, $\chi_{i,j}^{(f)}$ is the fuel mole fraction, $R_{i,j}$ is the processed Raman signal, $T_{i,j}$ is the FRS-measured temperature, $T_{ref} = 293$ K is the room-air temperature, and $g\left(T_{i,j}\right)$ is a function that accounts for small, temperature-dependent changes in the Raman cross section of CH_4.

The Rayleigh cross section of hydrocarbon-fueled diffusion flames is primarily determined from the local mole fraction of fuel, air, and the major product species CO_2, CO, and H_2O. Since 2-D imaging of the local concentrations of all of these species was not feasible, we have used a flamelet-based approach [36] to correlate the concentrations of CH_4, N_2, O_2, CO_2, CO, and H_2O based on information gleaned from the joint Raman/FRS data. This approach is similar to the conserved scalar approach of Starner and coworkers [37-39], where joint Raman and LRS results are used to track a conserved scalar, but it instead relies upon a more simple set of rules.

The required species mole fractions were computed as unique functions of the fuel-stream mixture fraction, Z, for a laminar, opposed-flow, 67/33 N_2/CH_4 – air diffusion flame. Flamelet-based modeling [36] postulates that temperature and species mole fractions are unique functions of Z for a given local flame strain. The calculation was carried out for a moderate strain[‡] of 390 sec^{-1}. We used the results of this calculation to correlate all major species mole fractions to the Raman-measured CH_4 mole fraction on the rich side, and the FRS-measured temperature on the lean side. These correlation functions are plotted in Fig. 16. When the Raman-measured CH_4 mole fraction was 1% or larger, the "rich-side" model of Fig. 16a was used to compute the mole fraction vector for use in Eq. 4, from which an appropriate FRS temperature response curve was calculated. For Raman-measured fuel mole fractions less than 1%, the required mole fractions were correlated with the FRS-measured temperature and the "lean-side" model of Fig. 16b was

---

[‡] We have analyzed the results using opposed-flow calculations for several different strain rates between equilibrium and extinction. The results showed less than a 50-K change in the FRS-measured temperature over this range of strains, so that the selection of strain rate should not significantly impact the data.
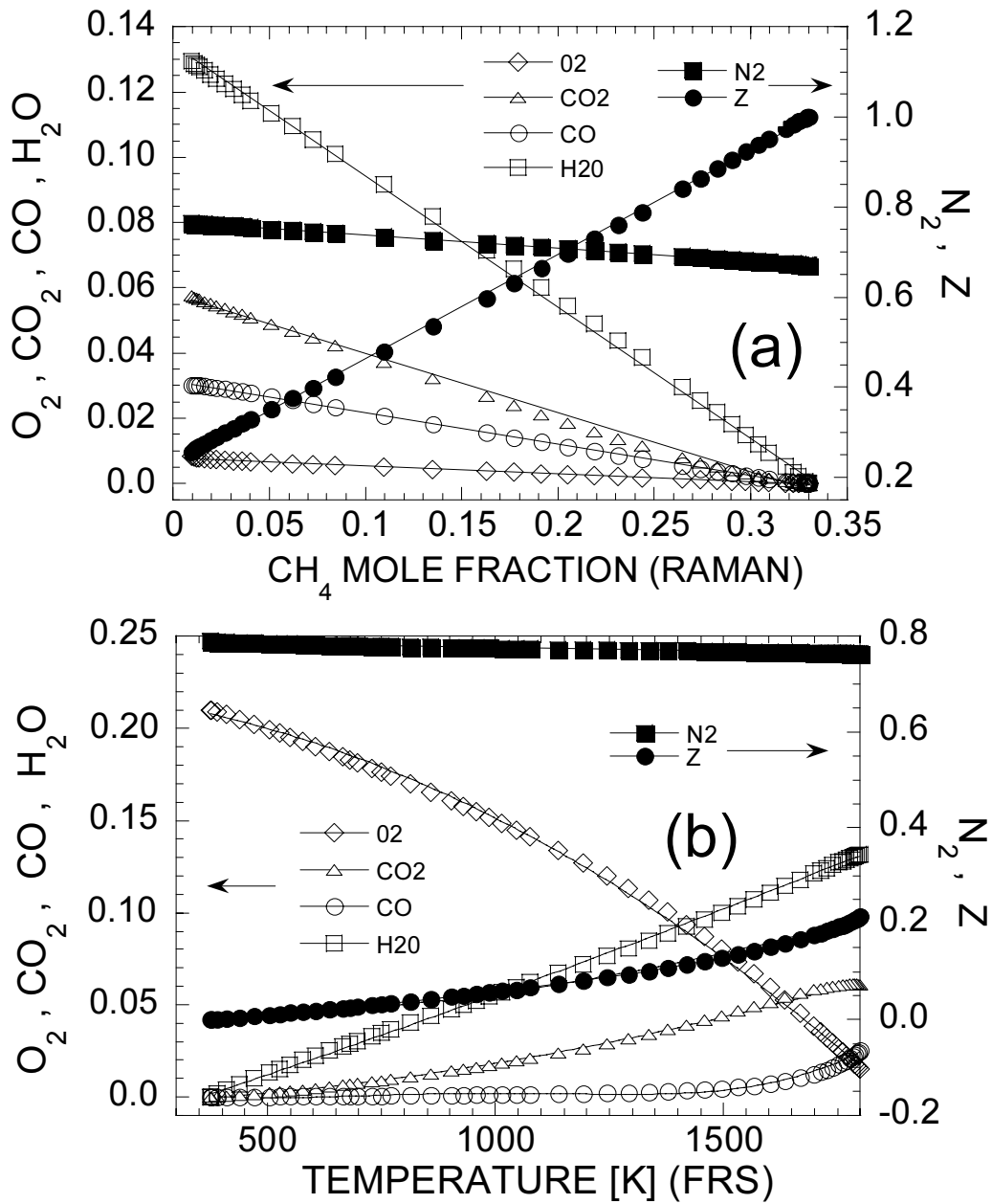
Figure 16 – Correlation functions derived from opposed-flow diffusion-flame calculations and used in analysis of the joint Raman/FRS data. The rich-side model is shown in (a) and the lean-side model in (b). Data points indicate the results of the diffusion flame calculation and lines represent curve fits to the calculated results used for analysis of the Raman/FRS data.

used. An iterative process utilizing Eqs. 4, 5 and 9 and the correlations plotted in Fig. 16 was then applied to obtain maps of temperature and fuel mole fraction. Typical convergence of this process required 4-5 iterations.

We have applied the above data-analysis procedure to all of the results from the vortex-strained diffusion flame. As a demonstration of the effectiveness of this procedure we first present sample data from the "steady" reference condition where the vortex at 7.5-Hz forcing has passed through the field of view and the flame has relaxed to its unforced state. Results from this unforced base condition are presented in Fig. 17, where the normalized FRS signal is shown in Fig. 17a, and the corresponding temperature (color contours) and fuel-mole-fraction (black line contours) data are displayed in Fig. 17b. The in-plane spatial resolution of the FRS data is 101 μm × 101 μm. The significant difference in Rayleigh cross section between the fuel stream and the coflow air is clearly seen in the FRS signal data in Fig. 17a. The joint FRS-Raman imaging scheme is very effective in minimizing this potentially untenable bias error.

Horizontal profiles of temperature and fuel mole fraction at 10, 20, and 30 mm above the fuel slot have been extracted from the image data in Fig. 17b and plotted as "set 1" in Fig. 18. An additional set of FRS temperature profiles, which were acquired several months earlier, are also displayed as "set 2". We estimate that the fuel-mole-fraction results are accurate to ±3% mole fraction, or ±10% of the mole-fraction difference between the fuel and air streams. The CH_4-mole-fraction profiles in Fig. 18 reveal 1 to 2% fuel mole fraction at the location of peak FRS-measured flame temperature. For this unforced laminar diffusion flame the fuel is surely consumed at the location of peak temperature. This bias is due to small amounts of jitter in the flame, which smear the Raman signal that has been averaged for 200 laser pulses and due to small Raman SNR at the very low fuel number densities encountered in the reaction zone. At the FRS signal levels encountered in the reaction zone, a 2% bias in the measured fuel mole fraction results in a + 40 K increase in the FRS-measured temperature when using the flamelet-based model described above.

For comparison, nitrogen CARS measurements were performed at heights of 10, 20, and 30 mm above the fuel slot. The spatial resolution of the CARS measurements is 50 μm and the uncertainty in the CARS data is ±25 K. The CARS measurements in the slot burner were performed at the Combustion Research Facility at Sandia/CA, which is near sea level, while the

Table 1 – Comparison of peak flame temperatures from the Wolfhard-Parker slot flame. The CARS measurements were performed at sea level at Sandia/CA while the FRS measurements were conducted at Sandia/NM at an altitude of 1650 m.

Y [mm]	T, FRS [K] set1/set2	T, CARS [K]	X_{peak}, FRS [mm] set1/set2	X_{peak}, CARS [mm] set1/set2	ΔT [K] set1/set2	ΔT [%] set1/set2
10	1809/1722	1872	8.6/8.0	8.05	63/150	3.3/8.0
20	1836/1820	1848	9.1/9.2	8.10	12/28	0.6/1.5
30	1829/1771	1849	8.8/10.0	8.10	20/78	1.1/4.2

joint FRS/Raman data were acquired at Sandia/NM at an altitude of 1650 m, where the nominal barometric pressure is 0.82 atm. The data in Fig. 18 show the impact of barometric pressure on diffusion flame structure, with the high-altitude FRS data exhibiting a broader temperature profile than the sea-level CARS results. A similar trend with altitude has also been reported in unforced Wolfhard-Parker flames with an undiluted methane fuel stream by Chen *et al.* [40]. Chen *et al*. observed a broader flame structure with little change in peak flame temperature, which suggests that barometric pressure impacts fluid dynamics, but not flame thermodynamics. Similarity of flame thermodynamics is also given credence by the good quantitative agreement of the flame temperatures at high-altitude (FRS) and sea level (CARS) from the premixed flat flame, which are shown in Fig. 13. With this evidence in mind, a quantitative comparison of the peak flame temperatures measured with CARS and FRS is still useful.

A quantitative comparison of the FRS-measured peak flame temperatures with the CARS results is summarized in Table 1. The tabulated data show that the agreement in peak flame temperatures is generally within 5% or 75 K. The worst-case agreement is at $Y = 10$ mm, where the signal-to-noise in the joint FRS-Raman data is weakest because the flow is illuminated by the low-energy tails of the Gaussian laser sheet at this location. The agreement between the two data sets is exceptional at $Y = 20$ mm, where the laser sheet energy is near its maximum. In all cases, the FRS-measured temperatures are lower than the CARS temperatures. It is unclear if this impact is real or if it is indicative of a small low-temperature bias in the FRS results.
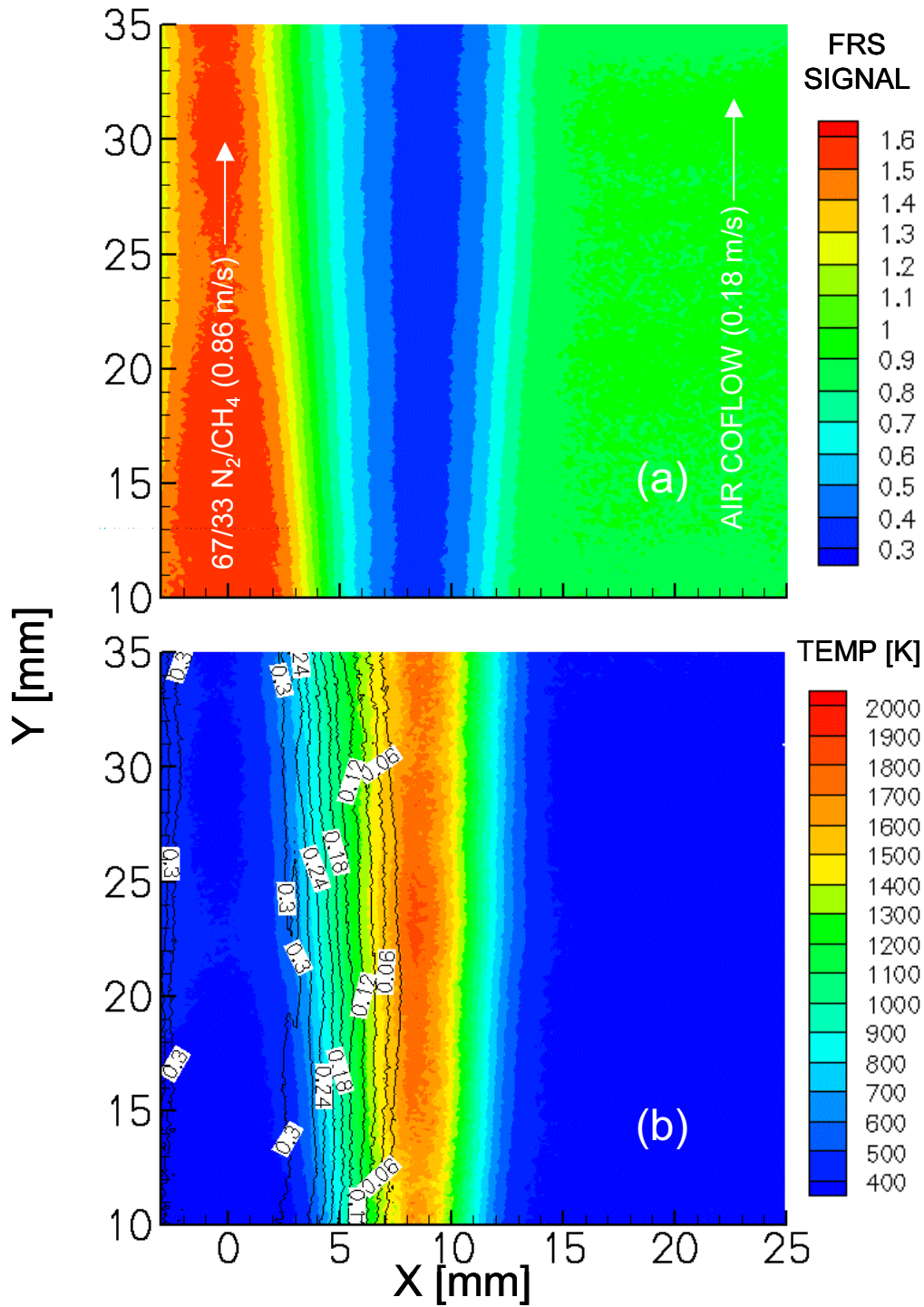
Figure 17 – Joint FRS-Raman results from a steady diluted CH_4-air slot diffusion flame. Normalized FRS signal contours, (a) and contours of temperature (color) and fuel mole fraction (black lines) shown in (b).
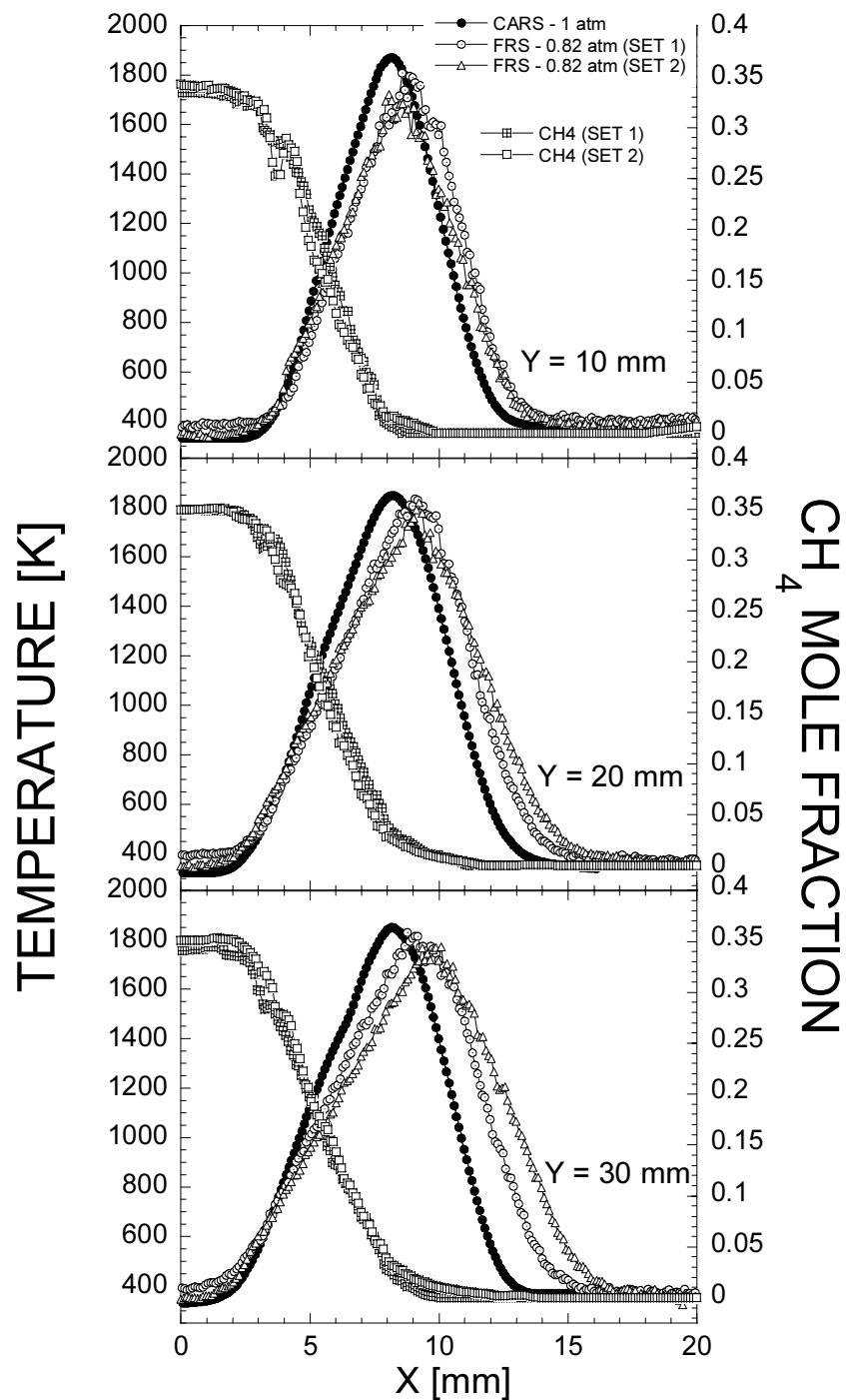
Figure 18 – Profiles of FRS-measured temperatures and Raman-measured fuel mole fraction from a diluted CH_4-air flame on a Wolfhard-Parker slot burner. The FRS and Raman data were recorded in Albuquerque, NM at 0.82 atm. For comparison, temperature profiles obtained by N_2 CARS in Livermore, CA at 1.0 atm are also shown.

7.5-Hz Forcing: Single Vortex-Flame Interaction

To demonstrate the effectiveness of the joint FRS-Raman imaging approach in a more complicated flame we have used the technique to image temperature and fuel mole fraction in vortex-strained slot flames. Forcing frequencies of 7.5 and 90 Hz were used. At 7.5-Hz forcing, a single vortex stretches the flame zone. CH chemiluminescence from the 7.5-Hz flame was recorded to visualize the structure of the reaction zone using a 50-μs ICCD gate. Four representative chemiluminescence images are shown in Fig. 19. The CH chemiluminescence images are simple to acquire, but they do display some artifacts of path averaging due to edge flames at the boundaries of the fuel slot and collection lens vignetting. This small amount of path averaging was deemed acceptable for purposes of reaction-zone characterization in light of the simplicity of the technique and the primarily 2-D nature of the slot burner. A previous investigation in the same burner by Mueller and Schefer [34] has shown that positive strain rates exist in the region around the outer, downstream edge of the vortex, while negative strain rates exist in the highly curved region at the upstream edge of the vortex where the flame appears to be folded. These regions are labeled for reference in Fig. 19. The CH images in Fig. 19 show that positive strain results in thinning of the CH layer while negative strain results in thickening of this layer. This result for CH is similar to the OH PLIF images presented by Mueller and Schefer [34], which are not impacted by path averaging effects.

The impact of the local strain rate on the temperature field can be quantified using the joint FRS-Raman imaging approach. Normalized FRS signal images and the corresponding temperature and fuel-mole-fraction results are shown in Figs. 20 and 21 at $t = 22.2$ ms, 25.9 ms, 33.3 ms, and 44.4 ms relative to the emergence of the disturbance from the fuel nozzle. All four images display a high-temperature region where the CH layer is thick and folded and a negative strain field exists. The peak temperature in this negative strain region ranges from 1850 K at $t = 22.2$ ms to 1950-2000 K at the three later times. This increase in temperature with time is consistent with the development of the negative-strain region that is evident in the increasing thickness of the folded portion of the CH layer with time. In all of the 7.5-Hz images shown in Figs. 19-21, the temperature monotonically decreases as one progresses downstream from the high-temperature, negative-strain region along the contour of the CH layer. The CH contour thins with downstream distance as the vortical "fuel tongue" begins to place increasingly positive stretch on the reaction zone. At $t = 22.2$ ms, the minimum FRS-measured peak flame temperature

is of order 1500 K in the vicinity of $x = 17$ mm and $y = 25$ mm, where the fuel tongue has penetrated farthest from the jet core. No local extinction of the flame is observed to occur at this location. As time increases, peak flame temperatures in the stretched region of the flame rise to 1650, 1675, and 1800 K ($\pm$ 50 K) for $t = 25.9$, 33.3, and 44.4 ms, respectively. The vortex appears to weaken and place decreasing strain on the reaction zone so that the minimum flame temperature increases with time and downstream distance. Support for the hypothesis of a weakening vortex is also given by the observed decreases in fuel-mole-fraction gradients in the vortex core, which are especially weak at $t = 44.4$ ms. A more quantitative assessment of the temperature-strain correlation in this well-controlled flame is possible with PIV imaging of the velocity field. Simultaneous velocity/temperature imaging in this flame is also possible with joint FRS-PIV [8, 9], as the molecular filter will strongly block particle Mie scattering from contaminating the temperature images. While possible, this work was not undertaken due to time and scope constraints associated with this FRS diagnostic development effort. Schefer [41] has recorded PIV images from this flame in his laboratory at Sandia/CA. Joint analysis of his FRS/PIV results may be possible to obtain a more quantitative picture of the temperature-strain behavior.
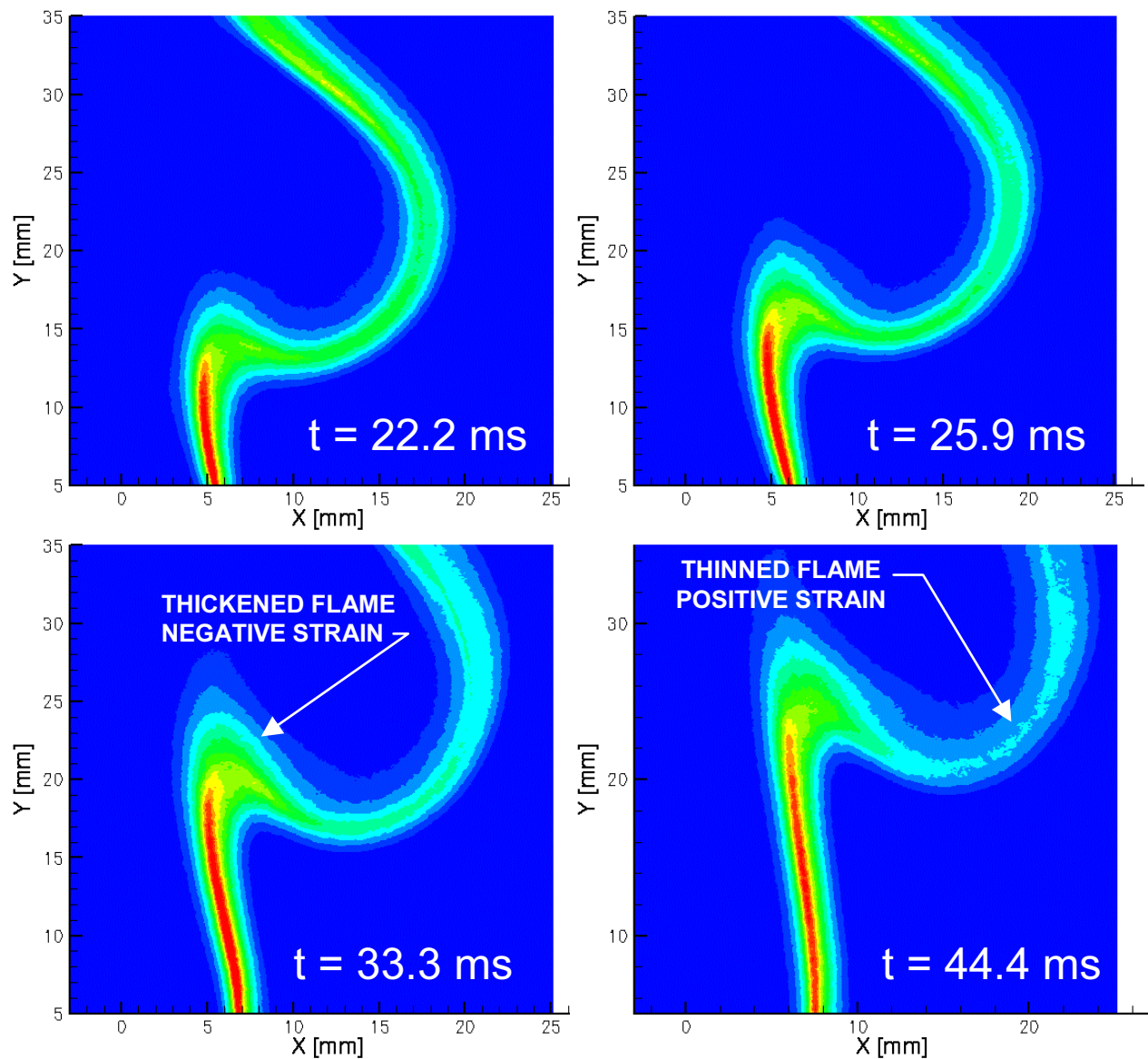
Figure 19 – CH chemiluminescence images (arbitrary units) at four selected phase angles from a vortex-strained Wolfhard-Parker slot diffusion flame. The flame is forced at 7.5 Hz where a single vortex strains the reaction zone. Red regions indicate the highest chemiluminescence signal while deep blue represents essentially no chemiluminescence.
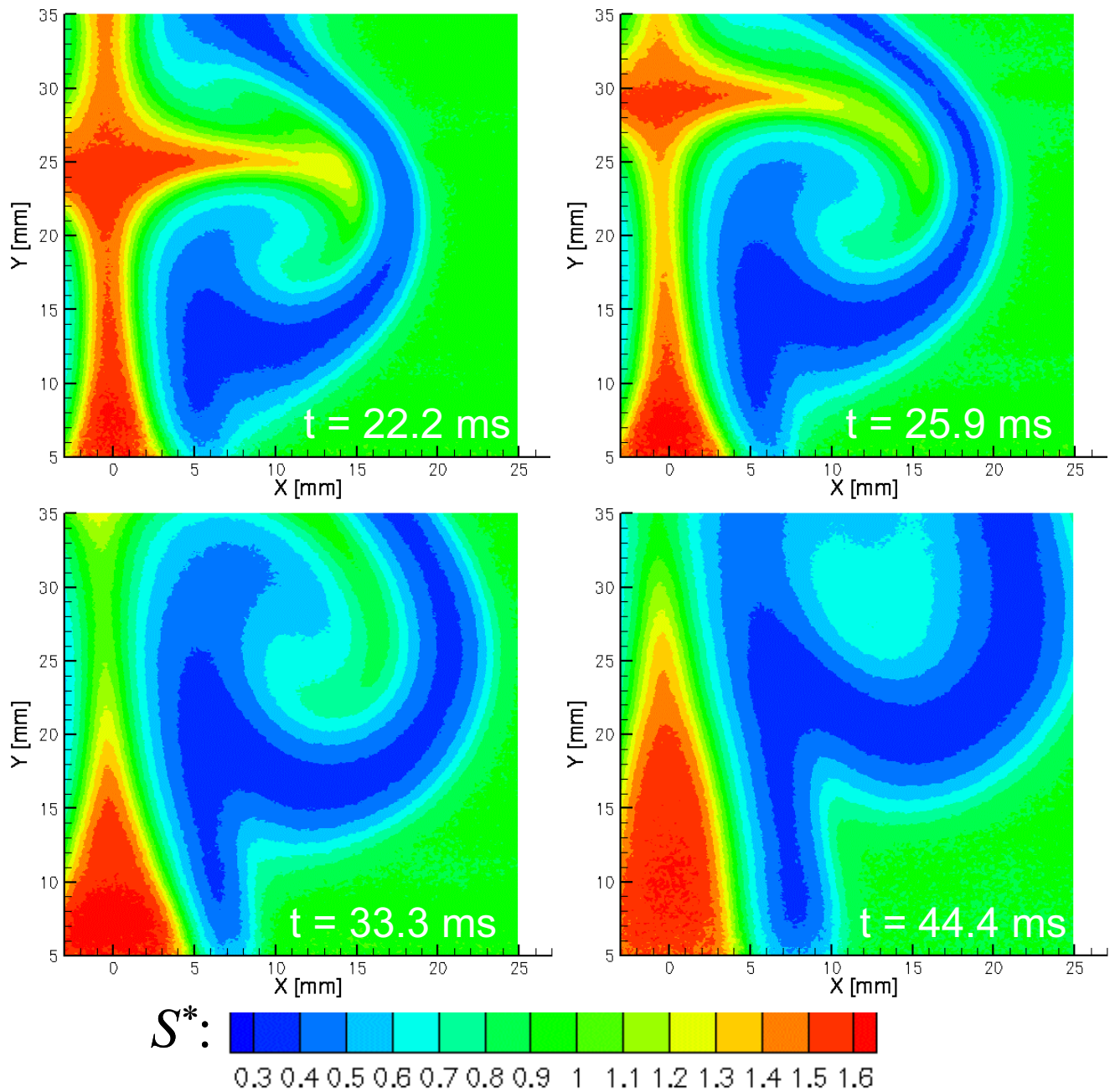
Figure 20 – Normalized FRS images at four selected phase angles from a vortex-strained Wolfhard-Parker slot diffusion flame. The flame is forced at 7.5 Hz where a single vortex strains the reaction zone. The data show the combined impact of temperature and varying Rayleigh cross section throughout the flowfield. The fuel stream can be seen in red, the high-temperature region in blue and the coflow air in green.
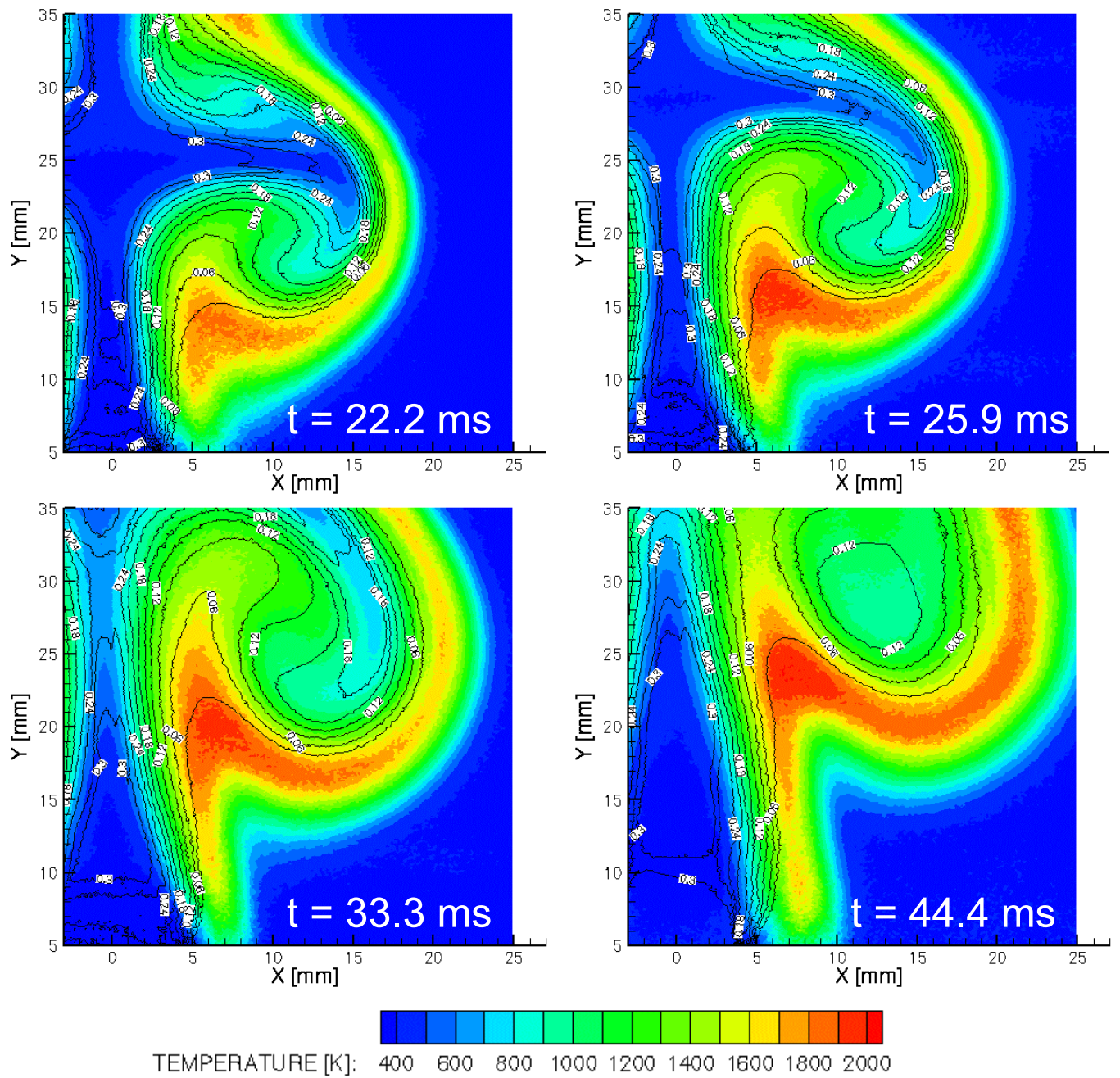
Figure 21 – Contour plots of temperature (color) and fuel mole fraction (black lines) at four selected phase angles from a vortex-strained Wolfhard-Parker slot diffusion flame. The flame is forced at 7.5 Hz where a single vortex strains the reaction zone.

90-Hz Forcing: Multiple Vortices and Flame Extinction

When the acoustic forcing frequency is increased to 90 Hz, while keeping all flow rates constant, the forcing is sufficiently rapid so that two consecutive vortices interact. This dual-vortex interaction produces strain rates that are sufficiently high to cause localized quenching of the flame. Localized quenching at 90-Hz forcing in this burner configuration was previously observed via OH PLIF by Mueller and Schefer [34].

CH chemiluminescence images and the corresponding normalized FRS signal images for the 90-Hz case are shown in Figs. 22 and 23, respectively, for 4 different phase angles. The CH chemiluminescence images have been averaged for 20 shots, while the FRS images have been averaged over 100 shots. The factor of 1.65 difference in the FRS cross section of the fuel and air streams allows for visualization of the fuel-side vortices using the normalized FRS signal data. Observation of the chemiluminescence images provides a qualitative description of the reaction zone behavior over the forcing cycle. At $t = 0$ ms (arbitrary reference) the corotating vortices create a region of strong, positive strain, which pulls a reacting fuel tongue toward the rich side of the diffusion flame. By $t = 0.6$ ms the CH images show that the fuel–side vortices have significantly weakened the flame and the quenching event occurs near this time. By $t = 1.2$ ms an isolated, fuel-rich reacting "island" is observed on the rich side of the flame and the CH data show that this island experiences burn out by $t = 5.9$ ms.

The corresponding results for temperature and fuel mole fraction for the 90-Hz case are displayed in Fig. 24. At $t = 0$ ms, the peak temperature of the reacting fuel tongue is in the vicinity of 1650 K, with a fuel mole fraction of 2 to 3 percent in the burning fuel tongue. This 1650-K temperature is in good agreement with the 1640-K value at extinction obtained from opposed-flow diffusion-flame calculations [42] and is an indicator that localized extinction is imminent. The main vertical portion of the diffusion flame exhibits peak temperatures of 1750-1800 K for $y < 20$ mm and 1800-1900 K for $y > 30$ mm, which is downstream of the second fuel-side vortex. In this downstream region the high temperature zone appears to be thicker and the local strain is potentially decreased, although this is not accompanied by an increase in thickness of the CH layer.

By $t = 0.6$ ms the chemiluminescence data in Fig. 22 show that the reaction zone in the vicinity of the fuel tongue has broken. The FRS-measured peak temperatures in this region are

on the order of 1550-1600 K, which is below the 1640-K extinction threshold for this flame. The fuel mole fraction in the extinguished region remains on the order of 2 to 3 percent. At t = 1.2 ms, the peak temperatures in the extinguished region of the fuel tongue are even lower at 1475-1500 K, and the fuel mole fractions in this region have increased to 4-5 percent as a likely consequence of diffusion from the nearby fuel vortices. The isolated island of burning fuel mixture is at a peak temperature of 1775-1850 K with a fuel mole fraction of about 3 percent in this region. The chemiluminescence images of Fig. 22 show that the isolated island burns out near t = 5.9 ms. At burnout, the temperature of the reacting fuel island is 1650 K, while the measured fuel mole fraction at burnout is 5 percent, which shows that the burnout mechanism is consumption of oxygen rather than fuel.
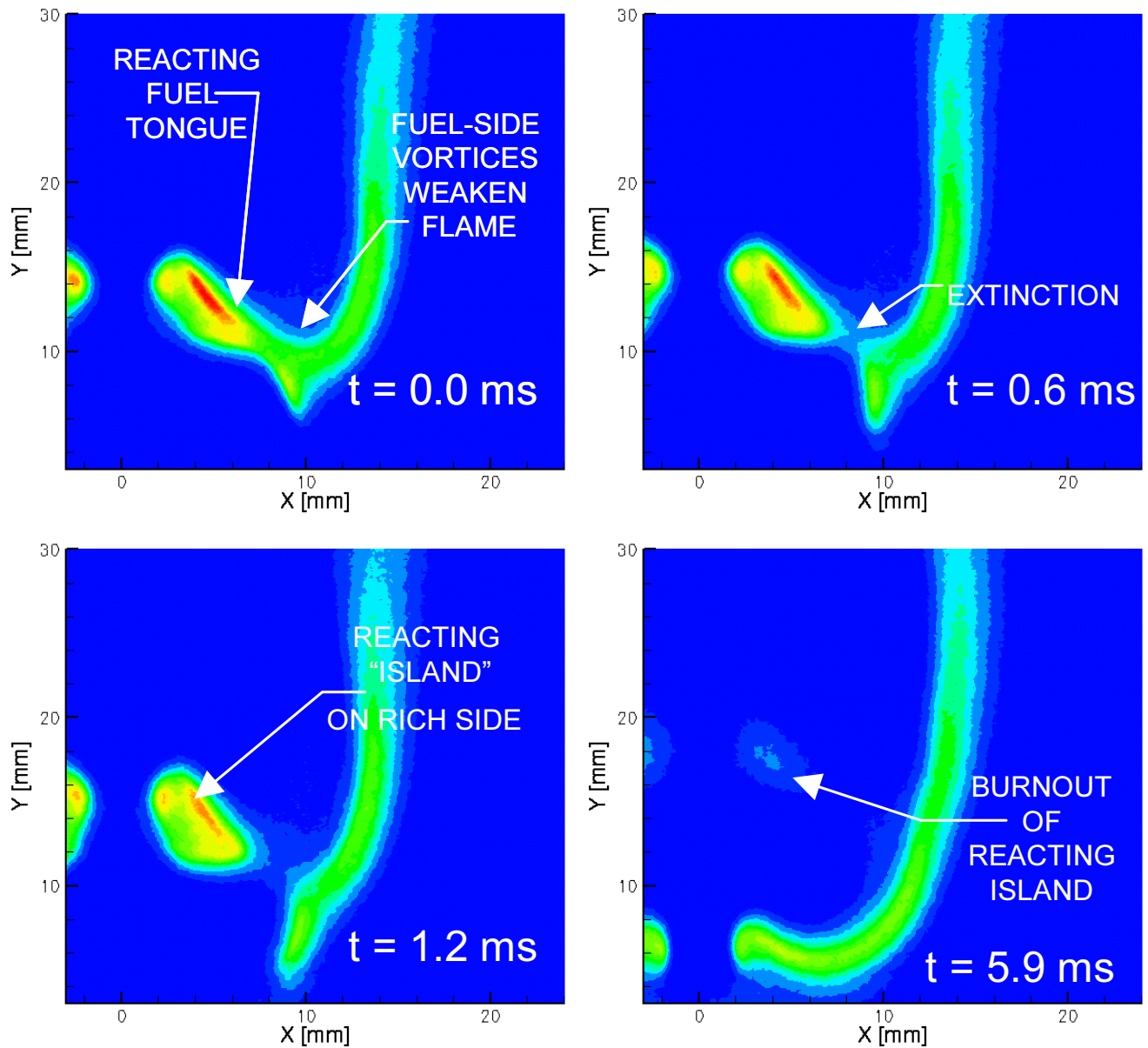
Figure 22 – CH chemiluminescence images (arbitrary units) at different phase angles from a CH_4-N_2-air Wolfhard-Parker slot diffusion flame that is periodically forced at 90 Hz. Red-yellow regions indicate the highest chemiluminescence while blue regions indicate essentially no chemiluminescence. The CH luminosity serves as a marker of the reaction zone and these images show evidence of a strain-induced flame extinction event at $t = 0.6$ ms.
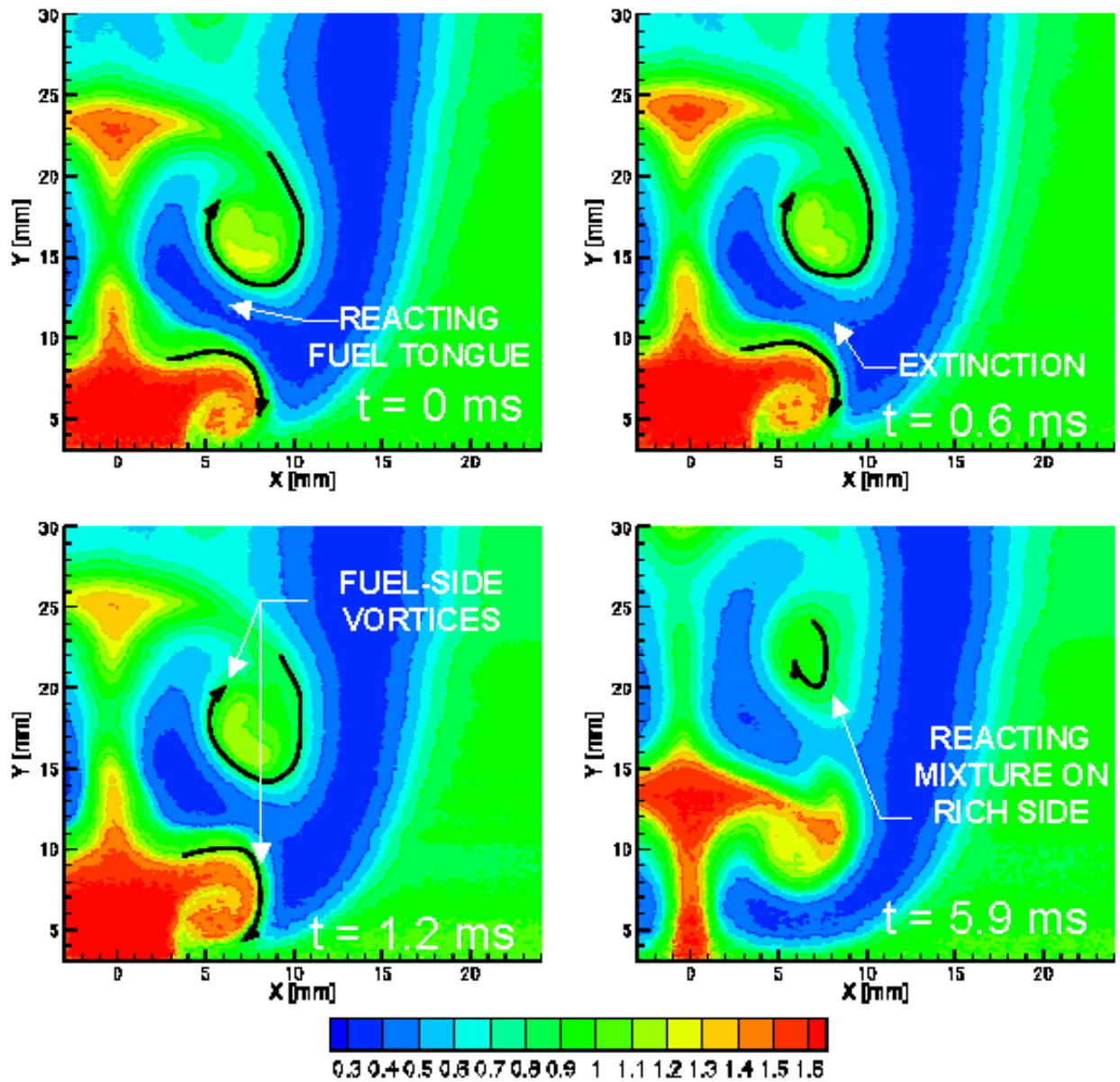
Figure 23 – Normalized FRS signals from a CH$_4$-N$_2$-air Wolfhard-Parker slot flame that is periodically forced at 90 Hz. The nominal factor of 1.6 difference in the FRS cross section of the fuel and coflow air streams allows for the structure of the fuel-side vortices that strain and quench the flame to be visualized.
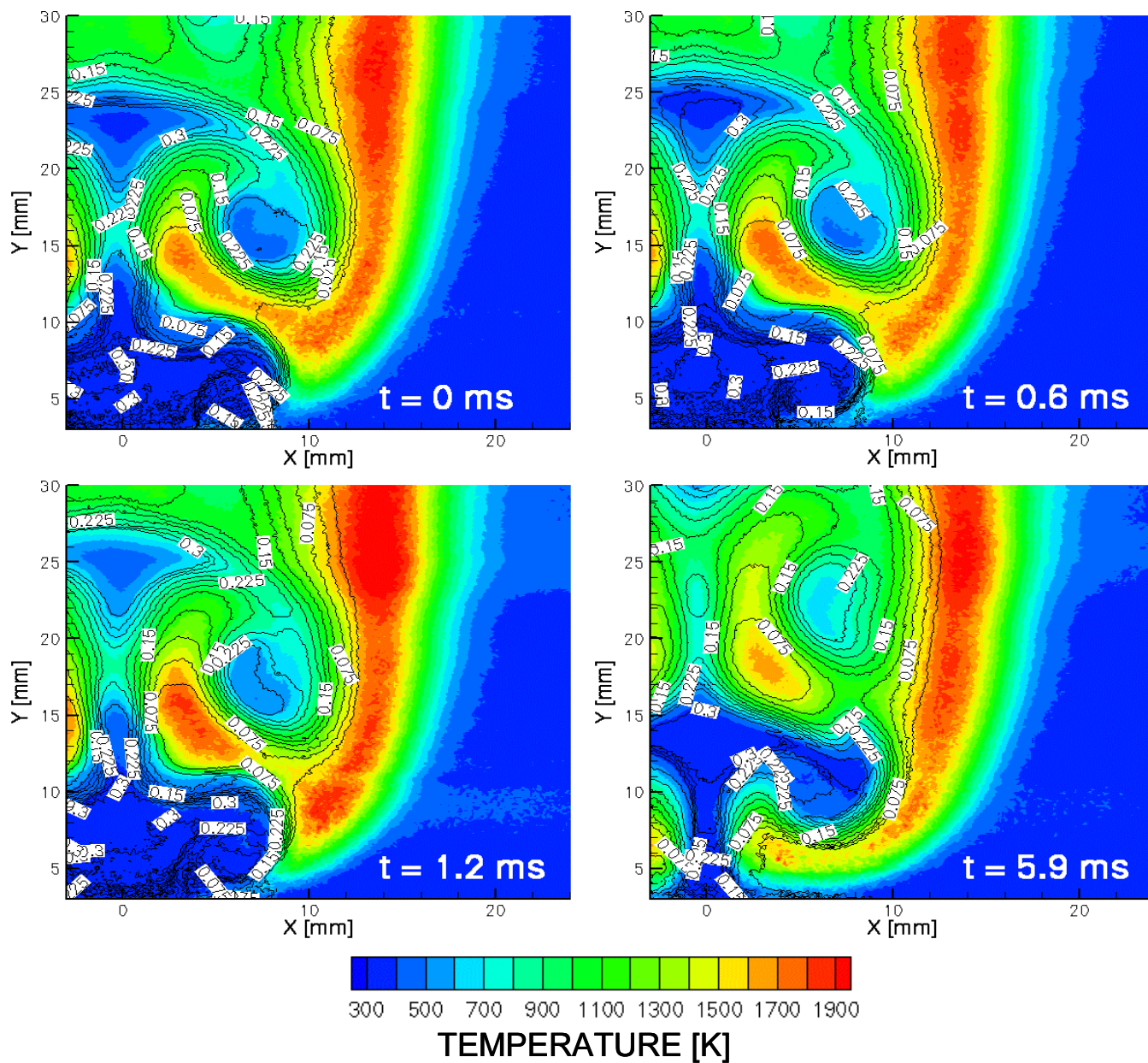
Figure 24 – Joint FRS/Raman measurements of temperature (color) and CH_4 mole fraction (line contours) from a CH_4-N_2-air Wolfhard-Parker slot flame that is periodically forced at 90 Hz.

Temperature Imaging in Sooting Premixed Flames

Background

In this section we present the results of our FRS temperature-imaging studies in a premixed, sooting ethylene-air flame. While laser-diagnostic approaches have become popular for a multitude of combustion measurements in clean flames, optical interferences from particulate have often precluded their use in sooting and other particle-laden combustion systems. For noninvasive temperature measurements, a few select laser-diagnostic approaches have been applied in sooting flames with some degree of success. Most notably, coherent anti-Stokes Raman scattering (CARS) has proven quite successful for point temperature measurements in highly sooting flames [43-45], coal-particle-laden combustion [46-48], and in extremely luminous propellant-fueled flames [49, 50]. The success of CARS in "dirty" combustion environments is mainly due to its coherent laser-like and spectrally narrow signal beam. These features permit collection of the full CARS signal at extremely small aperture and spectral bandwidth, which lead to highly efficient rejection of incoherent and broadband interferences from particulate and renders the measurement insensitive to absorption by soot. The chief disadvantage of CARS relative to other modern laser-based approaches is that CARS is limited to point or line-imaging data and cannot be used for 2-D, spatially correlated temperature imaging.

For quantitative temperature imaging, two laser-based approaches – two-line indium PLIF [51] and Filtered Rayleigh Scattering [10] – have been recently demonstrated by a group at the Division of Combustion Physics at the Lund Institute of Technology, Sweden. With two-line indium PLIF, an atomic indium seed molecule is added to the reacting flowfield and an exciting laser source is tuned to two separate absorption-emission transitions. When the upper level states of the two transitions are the same, the LIF signals can be ratioed to eliminate uncertainties arising from chemistry-dependent collisional signal quenching. Indium or other metal atoms are an attractive choice for sooting flame temperature imaging because of their simple electronic structure and because the required fluence of the exciting laser beams can be well below the threshold for interference from soot laser-induced incandescence and emission from laser-produced C_2. Drawbacks vis-à-vis FRS include: the required seeding of the flame, where metallic seed atoms may artificially reduce soot levels by facilitating soot oxidation, and the

increased experimental cost and complexity as two separate dye and/or OPO laser systems and two intensified detectors are required for single-pulse temperature imaging.

FRS does not require chemical seeding and only requires a single laser source and detector for experiments in premixed flames, where the variations in local scattering cross section are small. To our knowledge, the only demonstration of FRS in sooting flames has been reported by Hoffman and Leipertz [10], who provide time-mean temperature imaging in a partially premixed CH_4-air flame. These researchers characterized the flame as "weakly sooting" and did not provide detailed measurements of the range of soot volume fractions where FRS is expected to succeed. They did, however, mention successful FRS temperature imaging at a local soot volume fraction of 0.25 ppm in a subsequent paper on UV Raman scattering [52].

In the present work, our goal is to more systematically assess the applicability of FRS temperature imaging in premixed sooting flames. To achieve this, we have performed time-averaged FRS measurements in the premixed C_2H_4-air flat flame provided by a 60-mm diameter McKenna burner. A premixed flame was selected so that the large variations in Rayleigh cross section associated with diffusion-flame structure could be avoided. Quantitative profiles of soot volume fraction in these flames were measured using extinction-calibrated laser-induced incandescence (LII). It is hoped that this work will provide increased understanding of the capabilities and limitations of the FRS technique for quantitative temperature imaging in sooting combustion environments.

Sources of Interference for FRS Thermometry in Sooting Flames

The chief potential sources of interference for FRS in sooting flames are: (1) Mie scattering from soot particles, (2) laser-induced incandescence (LII) from soot, (3) C_2 Swan-band radiation, and (4) laser-induced fluorescence (LIF) of polycyclic aromatic hydrocarbons (PAH-LIF). By design, FRS minimizes soot Mie-scattering interference, which is spectrally identical to the injection-seeded line of the illuminating Nd:YAG laser pulse and is strongly attenuated by the I_2 molecular filter. The remaining sources of interference are often weaker than soot Mie scattering, but they are spectrally broadband and can pass through the I_2 filter to contaminate measurements even with complete rejection of the soot Mie interference.

The spectral nature of soot LII and C_2 Swan-band emission is shown in Fig. 25. Both of these interferences are broadband with components in the vicinity of the 532-nm Rayleigh signal and
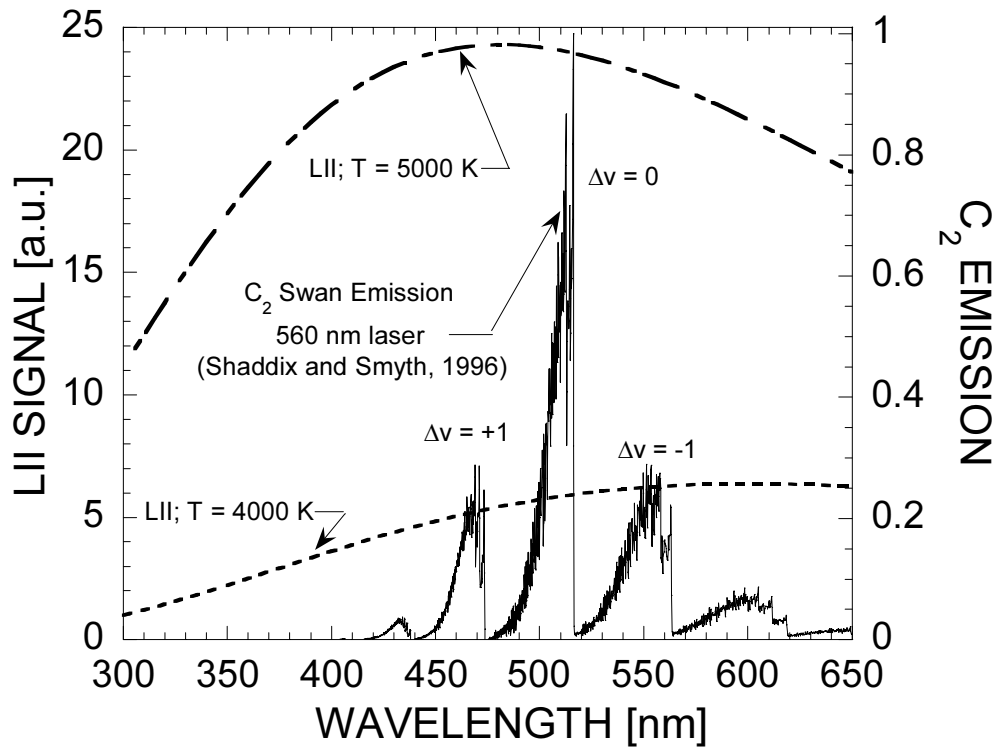
Figure 25 – Spectral characteristics of optical interferences to FRS thermometry in sooting flames. Representative soot LII spectra are shown as dashed lines for soot vaporization temperatures of 4000 K and 5000 K. The C_2 Swan band emission spectrum computed by Shaddix and Smyth [53] is also shown.

both largely arise as a result of laser-induced vaporization of in-flame soot particles. With LII, the soot particles are rapidly heated by the laser pulse to temperatures between 4000 K (near graphitic soot vaporization) and 5000 K [53], from which they cool primarily by particle vaporization and conduction over a period of several hundred nanoseconds. The T^4 dependence of the emitted thermal radiation from soot ensures that the LII signal is much more intense than background luminosity from soot at naturally occurring temperatures, which are typically less than 2000 K. The spectral profile of the LII signal is well represented by a function of the form, $S_{LII} \sim i_{\lambda,b}/\lambda$, where $i_{\lambda,b}$ is the Planck function and λ is the emission wavelength. The factor of $1/\lambda$ reflects the spectral dependence of the soot emissivity in the Rayleigh limit for a constant index of refraction. LII emission is sufficiently intense to be detected with an intensified CCD camera and this effect is often exploited for measurements of soot volume fraction [53-57]. For

FRS imaging applications, this LII signature is an interference that must be minimized and/or approximately measured and subtracted from the measured FRS signal.

In addition to enhanced thermal radiation, the laser-induced soot vaporization process also results in the production of the gas-phase C_2 radical. C_2 is a source of interference for many laser-diagnostics because of its "Swan band" electronic resonances, which result in broadband fluorescence signatures that span the majority of the visible spectrum. The fluorescence spectrum of C_2 for near-resonant 560.3-nm laser excitation has been adopted from Shaddix and Smyth [53] and plotted alongside the LII spectra in Fig. 25, where it can be seen that C_2 fluorescence interference spans from 420 nm past 650 nm and into the near infrared. The strongest interference occurs at the $\Delta v = +1, 0$, and -1 bandheads near 473, 514, and 563 nm, respectively.

PAH species in flames are large molecules with mass of several hundred AMU, which have been documented as important precursors to soot formation [56]. Laser-induced fluorescence (LIF) from PAH species using both UV and visible laser wavelengths is well established [56, 58]. Spectrally, PAH peaks just to the red of the exciting laser line and then decays to the red of the laser peak over a range of several hundred nanometers [59]. Like LII, PAH fluorescence can be exploited for diagnostics purposes or it can be a nuisance background source.

In this study, we expect soot LII to be the largest source of broadband interference. The 532-nm wavelength the FRS signal is off resonance of the C_2 Swan system (Fig. 25) and C_2 emission signals with 532-nm Nd:YAG excitation have been reported to be more than an order of magnitude less than for near resonant C_2 excitation [60]. With visible laser wavelengths, PAH-LIF signatures have been observed to be smaller than with UV excitation sources [59] and LII has been reported to dominate PAH-LIF even for even the light 0.1-ppm-level soot volume fractions encountered in our study [56].
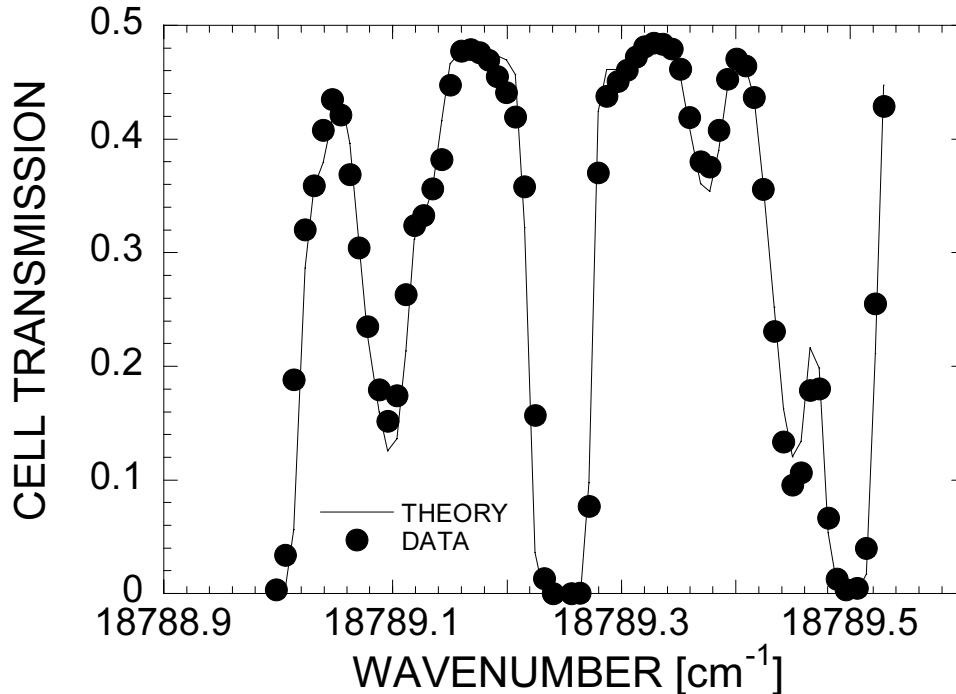
Figure 26 – Transmission spectrum of the optically thick I_2 molecular filter used for measurements in a premixed sooting C_2H_4 flame. The transmission data are compared to the theoretical model of McKenzie [26] with a best-fit iodine saturation temperature of 53 $^{\circ}$C. This level of I_2 loading resulted in a line-center rejection of 10^3 for the R121 (35-0) transition near 18789.25 cm^{-1}.

Procedure for FRS Thermometry in the Premixed Sooting Flame

We have performed a series of FRS temperature-imaging experiments in a laminar, flickering, premixed C_2H_4-air flame provided by a 60-mm-diameter McKenna burner. This burner is a simple sintered-metal plug embedded in a water-cooled substrate. Fuel and air were premixed upstream of the plug and the burner provides a flat flame adjacent to the sintered metal surface. FRS and LII measurements were made in the combustion-product gases in a region spanning 60 mm parallel to the burner and heights from 3 to 30 mm above the burner surface. The objectives of this series of measurements was to perform quantitative temperature imaging using FRS while also documenting the levels of soot loadings in these flames using 1-D LII imaging of the soot volume fraction. With these complementary FRS/LII data, we hope to quantify the maximum degree of soot loading for which FRS is a viable imaging thermometer in

sooting flames. A premixed flame has been selected so that complexities associated with large spatial variations in Rayleigh cross section are not an issue. Ethylene has been selected as the fuel because it readily provides for a wide range of soot loadings from soot inception to heavily sooting flames at ppm-level volume fractions.

The optical arrangement for FRS imaging in the sooting flames was similar to the arrangement used for the nonsooting flame investigations, which is shown in Fig. 5, with a few minor modifications. To increase the level of rejection provided by the I_2 molecular filter, we have increased the nominal iodine vapor pressure in the cell from 1.49 to 2.65 Torr (corresponding to an increase in I_2 saturation temperature from 45 to 53°C). The resulting transmission spectrum for the filter is shown in Fig. 26. This increase in I_2 number density resulted in a line-center rejection of 10^3 for the R121 (35-0) transition near 18,789.25 cm^{-1}, but with an overall decrease in transmitted FRS signal as the nonresonant background transmission was decreased by about 33% relative to the cell condition used for the nonsooting flame work shown in Fig. 6a. A laser-line interference filter with a 10-nm band pass centered at 532 nm was also placed in front of the ICCD camera lens to spectrally filter broadband background interference from soot LII, C_2 Swan emission, and PAH LIF. This laser-line filter had an out of band rejection of 10^4 and pass band transmission of 45%. To minimize broadband interferences the laser power for the sooting flame FRS measurements was limited to 200 mJ/pulse. The net effect of increased nonresonant I_2 molecular-filter rejection, use of the 532-nm laser-line interference filter, and limited laser pulse energies resulted in a factor of 7 to 10 decrease in FRS signal levels as compared to our investigations in nonsooting flames. Averaging of the FRS signal over 100 laser shots helped to increase SNR, but the resulting FRS images were still of lower quality than those acquired in the nonsooting flames.

FRS images were acquired from the sooting premixed flame for 5 different equivalence ratios, which are summarized in Table 2. At each equivalence ratio, 100 FRS images were accumulated on the ICCD, along with 100 images with the laser blocked to record any background flame emission at 532 nm and 100 images with the 532-nm laser-line filter replaced by a 633-nm laser line filter. All images were recorded with an ICCD gate of 200 ns. The measured flame emission signatures at 532 nm were found be a negligible fraction of the FRS signal level. The 633-nm images were acquired to estimate the level of LII and C_2 Swan background. The reduced laser fluence used in these experiments kept these contributions low,

Table 2 – Test matrix for FRS temperature imaging measurements in a sooting, premixed ethylene-air flame supplied by a McKenna burner.

Flame #	Q_{air} [SCCM]	Q_{fuel} [SCCM]	ϕ	C/O
1	9.2	1.3	2.10	0.67
2	9.0	1.3	2.14	0.69
3	8.8	1.3	2.19	0.70
4	8.6	1.3	2.24	0.72
5	8.4	1.3	2.29	0.74

however, some broadband interference did contaminate the FRS images. The 633-nm wavelength was selected for approximate measurement of these nuisance signals because the chief source of background from soot LII was expected to be of similar magnitude at 532 and 633 nm, with the expected LII levels at the two wavelengths within 4% at a soot temperature of 4000 K and within 16% at 5000 K. This procedure does not account for any C_2 Swan-band emission or PAH LIF, but was viewed as acceptable since the measured background signals at 633 nm were less than 10% of the FRS signal for flames 1 through 4 and since soot LII was expected to be the main source of background. Current work in this flame is relying on a much faster ICCD gate of 20-30 ns so that broadband interferences are more efficiently rejected.

The FRS temperature-response curve for the combustion product gases of the premixed C_2H_4-air flame was computed using Eqs. 4 and 5 and using major species mole fractions measured by Xu *et al.* [61] for a similar premixed C_2H_4-air flame. The tabulated mole fractions and the resulting FRS temperature-response curve are shown in Fig. 27. The 100-shot-averaged FRS signals were then normalized according a modified version of Eq. 8 above,

$$S_{i,j}^* = \frac{F_{i,j} - B_{i,j} - E_{i,j} - L_{i,j}}{A_{i,j} - B_{i,j}} \quad , \tag{10}$$

where $F_{i,j}$ is the FRS signal, $A_{i,j}$ is the FRS reference signal recorded in room-temperature air, $B_{i,j}$ is the background laser light scattering estimated using Eq. 7, $E_{i,j}$ is the measured flame-emission background at 532 nm and $L_{i,j}$ is the measured broadband interference signal at 633 nm.

Species	Mole Fraction [%]
N_2	56.6
CO	19.1
CO_2	2.3
H_2O	10.0
H_2	10.0
CH_4	1.0
C_2H_2	1.0
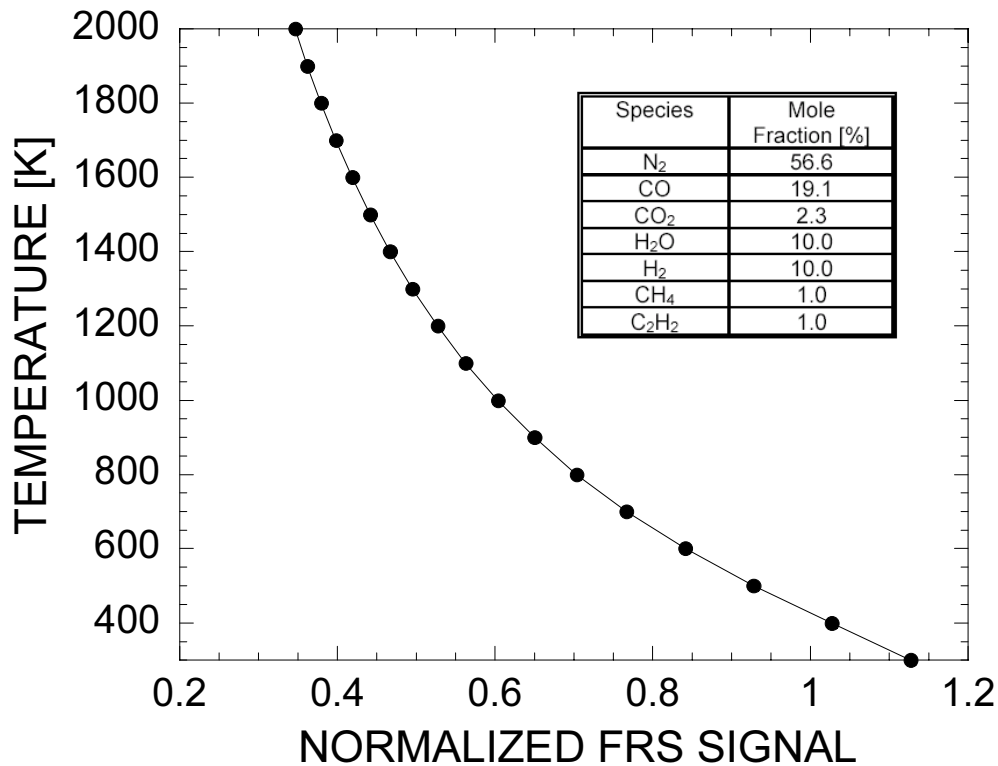
Figure 27 – FRS temperature-response function used for analysis of data from the premixed, sooting ethylene-air flame. The species mole fractions used with Eq. 4 for computation of this function are shown in tabulated form on the plot.

LII Measurements of Soot Volume Fraction in the Premixed Sooting Flame

The same LII signal that is an unwanted background in the FRS measurements can also be exploited for measurements of soot volume fraction. The working principles of the LII technique are explained in detail in several excellent sources [53-56, 62] and are only discussed in minor detail here. In the Rayleigh limit, where laser and soot-particle emission wavelengths are significantly larger than the soot-particle diameter, the detected LII signal is represented by $S_{LII} \sim d^{(3+0.154/\lambda[\mu m])}$ [53], where d is the soot primary particle diameter and λ is the LII detection wavelength in microns. For the 633-nm bandpass filter used for LII detection in our experiments this results in a $d^{3.24}$ dependence, so that the detected LII signal is nearly proportional to the local volume fraction of soot.

Interference with the LII signal from C_2 Swan emission was expected to be low because the 633-nm wavelength, at which the LII signal is sensed, is detuned from any C_2 Swan resonances (see Fig. 25). For 532-nm laser excitation some degree of PAH-LIF background may also be present in our LII data [58], but soot LII is expected to be significantly larger than PAH-LIF [56]. Detection at wavelengths near 400 nm, as was used by Shaddix and Smyth [53], is often more preferable because this region is also off resonance of the C_2 Swan system and is significantly lower than the laser wavelength, which would eliminate any interference from PAH LIF as well. However, the quantum response of our ICCD detector was nearly zero in the blue region of the spectrum so 633-nm detection was viewed as the best available compromise between minimal interference and LII signal detection.

We have performed our LII experiments using the same optical system as for FRS with the I_2 molecular-filter cell removed and the LII signal imaged through the same 10-nm bandpass, 633-nm center laser-line interference filter that was used to estimate background signals in the FRS measurements. The LII data were recorded in a 2-D laser-sheet imaging configuration and in a 1-D line imaging mode obtained by removing the cylindrical lens from the FRS sheet-forming optics shown in Fig. 5. The 2-D LII images to be presented here are qualitative in nature due to difficulties associated with correcting for the weak, nonlinear dependence of the LII signal on the local laser-sheet intensity and due to the long 200-ns gate times employed, which bias the measurement toward slow-cooling large soot particles [55]. For a more quantitative measure of soot volume fraction, 1-D profiles at heights of $y = 15$ and 30 mm above the McKenna burner surface have been extracted from 1-D LII images of the focused beam propagating through the flame. These "line" LII images are much less sensitive to flat-field correction and they have also been acquired with a much shorter 25-ns ICCD gate, which opened coincident with the laser pulse, so that any measurement bias toward large particles has been minimized.

The line LII measurements have been calibrated using a laser-beam extinction measurement. The beam from a HeNe laser at 632.8 nm was propagated through the premixed C_2H_4-air flame at $y = 15$ mm above the burner surface for an equivalence ratio of $\phi = 3.06$. This flame was much richer than any of the flames that could be interrogated using FRS, but it was used for LII calibration because the soot loadings were sufficiently high (0.5 ppm peak) to provide a reliably measured extinction signal. A wedge beam splitter sent a portion of the HeNe laser beam to a reference photodiode that monitored any fluctuations in the laser power while the remainder of

the beam was propagated through the flame to a detection photodiode. Both photodiodes were equipped with 633-nm laser-line interference filters to minimize background soot luminosity and frequent reference calibration measures of the laser transmission through a soot-free path near the burner surface were recorded. In the Rayleigh limit, where the soot particles are much smaller than the laser wavelength, scattering may be neglected and the measured laser-beam extinction is entirely due to absorption. A horizontal profile of the HeNe laser-beam absorption was recorded and the absorption data were deconvolved using the 3-point numerical Abel inversion developed by Dasch [63]. The local laser-beam extinction could then be related to the soot volume fraction by the following equation, which is valid in the Rayleigh limit.

$$f_v = -\ln\left(\frac{I}{I_o}\right)\frac{\lambda}{K_e\Delta r}$$
(11)

In Eq. 11, I/I_o is the local laser-beam extinction ratio obtained from the Abel inversion, $\lambda = 632.8$ nm is the HeNe laser wavelength, Δr is the grid-spacing of the deconvolved extinction data (2.54 mm here) and K_e is the dimensionless extinction coefficient which, in the Rayleigh limit, is given by,

$$K_e = \frac{36\pi nk}{4n^2k^2 + \left(n^2 - k^2 + 2\right)^2} \quad ,$$
(12)

where n and k are the real and imaginary parts of the soot refractive index, respectively. We have used the values $n = 1.57$ and $m = 0.56$, which have been attributed to Dalzell and Sarofim [64] as discussed by Smyth and Shaddix [65]. A line LII profile was then acquired in the $\phi = 3.06$ calibration flame and a calibration constant (soot ppm per LII signal count) for the LII images was obtained by comparing the LII signal counts to the extinction-measured soot volume fraction and in the peak sooting region of the calibration flame.

Premixed Sooting Flame Results

Results for each of the five flames listed in the test matrix of Table 2 are displayed in Figs. 28-32. As listed in Table 2, the flames have been numbered 1 through 5 in order of increasing equivalence ratio and soot loading. In each figure, part (a) is an unfiltered Rayleigh image

70

recorded with the image intensifier at very low gain to avoid damage to the ICCD, and with the burner surface moved out of the field of view to avoid intense reflections from the burner substrate. Part (b) is a filtered Rayleigh image from the sooting flame recorded with the image intensifier at maximum gain. Part (c) of the figures is a 2-D soot LII image recorded in a 10-nm band centered at 633 nm, with the I_2 filter removed, and at a 532-nm laser-sheet energy of 600 mJ/pulse (3.9 J/cm^2 average fluence) using a 200-ns ICCD gate that opened coincident with the laser pulse. Part (d) of the figures is the FRS-measured temperature field, and parts (e) and (f) are 1-D profiles of FRS-measured temperature and quantitative soot volume fraction obtained from the 1-D LII measurements at $y = 15$ and 30 mm above the burner surface.

In all of the figures, the unfiltered and filtered Rayleigh images in parts (a) and (b) are the average of 10 laser shots. No pixel binning has been performed on the optical data and the resulting in-plane spatial resolution of the FRS and LII results is 110 μm/pixel. All of the raw Rayleigh images have been scaled so that the 5% and 95% levels of their respective image-intensity histograms represent the violet and white color cutoffs. In each of the Rayleigh images, the laser-sheet propagates from left to right and the nominally Gaussian profile of the laser-sheet energy density is clearly visible in the filtered Rayleigh images in part (b). In the filtered Rayleigh images, the high intensity levels at the left- and right-hand edges of the images represent cold-gas regions while the hottest regions of the premixed flame are in the image center where the relative image intensities are lowest.

In Flames 2-5 the unfiltered Rayleigh images in part (a) are clearly degraded by intense Mie scattering from soot and/or laboratory dust. Flame 1, shown in Fig. 28a, has the lightest soot loading of all the flames studied. The profile of the laser-sheet is still discernable in Fig. 28a and the scattering signal in the hot-gas region is much lower than for the cold-gas zone. Both of these observations suggest that the unfiltered Rayleigh image from Flame 1 is minimally impacted by soot Mie scattering. As the soot levels are increased in Flames 2-5 we see that soot Mie scattering begins to overwhelm the molecular Rayleigh signal. At the burner centerline and 25 mm above the burner surface, the measured unfiltered scattering levels in Flames 2-5 are 1.2, 4.7, 34, and 98 times larger than the measured values in Flame 1. The I_2 molecular filter used in our experiments provides a measured line-center rejection of 1,000 ($\pm$30%), which clearly results in a cleaner set of filtered images shown in part (b) of the figures. If we assume that the signal from the hot-gas regions of the unfiltered Flame 1 image is a reasonable approximation of the

71

molecular Rayleigh signal, and that the increase in scattering in the other unfiltered images (Figs. 29a, 30a, 31a, and 32a) is from soot Mie scattering, then the Mie interference is reduced to 0.02, 0.36, 3.3, and 10% of the molecular Rayleigh signatures for Flames 2-5, respectively. At higher soot loadings, such for Flames 4 and 5, the upper regions of the filtered Rayleigh images in part (b) are contaminated by soot Mie-scattering and LII/C_2 interferences. This contamination causes a distortion in the upper portion of the near-Gaussian vertical laser-sheet profile, which appears to be broadened at the $x = 0$ flame centerline.

For all 5 flames, the 2-D LII images in part (c) of the figures have been left in terms of arbitrary units and have not been converted to soot volume fractions due to the difficulties cited in the above discussion of the LII technique. Because the LII signal displays only a weak dependence on local laser fluence, the raw LII images do serve as a semi-quantitative guide for the location of soot relative to the temperature and the more quantitative 1-D soot profiles presented in parts d-f of the figures. At the laser fluence levels used for 2D LII imaging, we have measured an LII power dependence of $S_{LII} \sim fluence^{0.5}$ at the vertical center of the laser sheet. The 2-D LII images shown in part (c) of the figures have been normalized by the square root of a background-subtracted FRS image acquired in room air as an approximate compensation for the laser-sheet profile. The soot LII signal in these flames is then observed to increase monotonically with vertical distance from the burner and begins to reach a maximum level by $y = 20$ or 25 mm. This observation is consistent with the extinction-based soot volume-fraction measurements of Xu *et al.* [61] obtained in similar C_2H_4-air premixed flames.

FRS temperature imaging results are displayed in part (d) of the figures. The temperatures have been obtained from FRS signal images that have been averaged on the CCD chip for 100 laser shots. The resulting FRS temperature fields display a flat-flame structure that is similar to the nonsooting measurements from the Hencken burner shown in Fig. 12. The horizontal temperature profiles in parts e and f of the figures show an increased level of data scatter relative to the results from nonsooting flames. This is likely a result of the factor of 7-10 decrease in FRS signal that results from the use of increased signal filtering and the factor of 5 drop in laser-sheet energy to minimize broadband LII, C_2 and PAH interferences. To better quantify the measured temperatures and the degree of scatter in the FRS results, we have computed mean temperatures and rms temperature fluctuations for -10 mm $< x < +10$ mm at $y = 15$ and 30 mm and for a larger square region of the flame defined by 10 mm $< y < 20$ mm. The horizontal extent of 10 mm on

Table 3 – Results of FRS/LII imaging study in a sooting, premixed ethylene-air flame supplied by a McKenna burner.

Flame #	T_{ad} [K]	$\bar{T}$ [K]/σ_T [K] -10 mm< x < +10 mm 10 mm < y < 20 mm	$\bar{T}$ [K], σ_T [K] y = 15 mm	$\bar{T}$ [K], σ_T [K] y = 30 mm	$f_{v,max}$ y = 15 mm	$f_{v,max}$ y = 30 mm	LII Backgd [% of FRS signal]
1	1849	1660 / 90.7	1640 / 82	1707 / 118	6.0×10^{-9}	9.0×10^{-9}	1.7
2	1828	1590 / 89.4	1579 / 86	1692 / 115	1.2×10^{-8}	3.0×10^{-8}	2.5
3	1802	1498 / 85	1489 / 76	1627 / 117.4	2.0×10^{-8}	5.5×10^{-8}	4.2
4	1777	1535 / 91.9	1541 / 83	1312 / 137	5.5×10^{-8}	1.1×10^{-7}	7.4
5	1751	1811 / 120	1845 / 98	1058 / 160	1.0×10^{-7}	1.8×10^{-7}	16.3

either side of flame centerline was chosen based on inspection of the FRS data, which exhibit a nearly flat temperature profile over this horizontal extent for all vertical heights above the burner. The results of these calculations for all 5 flames are shown in Table 3. The adiabatic equilibrium temperature and the magnitude of the correction for background LII at 633 nm are also listed in Table 3.

It is expected that the measured temperatures in each of these flames will be less than adiabatic equilibrium due to heat losses to the water-cooled burner substrate and from soot radiation. The 100-shot-averaged FRS temperature will also be decreased because the flickering flame investigated entrained some cold gas into the core on some of the laser shots. The on-chip averaged images are then slightly biased toward cold temperatures as a result of the nonlinear FRS temperature response and the higher FRS signal associated with colder gas. For Flames 1-3 and for y < 22 mm in Flame 4, the FRS-measured flame temperatures shown in Table 3 are about 180 K to 250 K less than adiabatic equilibrium. The measured temperatures decrease, as would be expected, with increasing ϕ both as a result of richer flame chemistry and increased heat loss from soot radiation. Xu *et al.* [61] report temperatures of 1750 K ($\pm$50 K) and 1600 K ($\pm$50 K) at y = 15 and 27 mm above the burner surface for a steady premixed C_2H_4-air flame at ϕ = 2.34 on the same type of McKenna burner used here. With this in mind the FRS-measured temperatures in the core of the flame are likely about 100 to 200 K (5 to 11%) too low. The bulk of this temperature bias is likely due to imperfect (underestimated) levels of background correction for LII and C_2-Swan interferences and the cold-gas density-weighting bias associated with on-chip FRS signal averaging.

At $\phi = 2.29$, Flame 5 was the richest operating condition investigated using FRS. At this operating condition the evaluated temperatures were too high. The reason for this is unclear. At 16% of the nominal measured FRS signal, the estimated correction for broadband interference is by far the largest for Flame 5. Overestimation of this correction would indeed cause an overestimate of the FRS-measured temperature. However, the uncorrected FRS signals in Flame 5 were actually lower than their counterparts for Flame 4. This issue is currently being resolved with repeat FRS measurements. These repeat measurements are also utilizing better-stabilized flame and a shorter, 20-30 ns detection gate, which will significantly reduce the required corrections for broadband optical interferences.
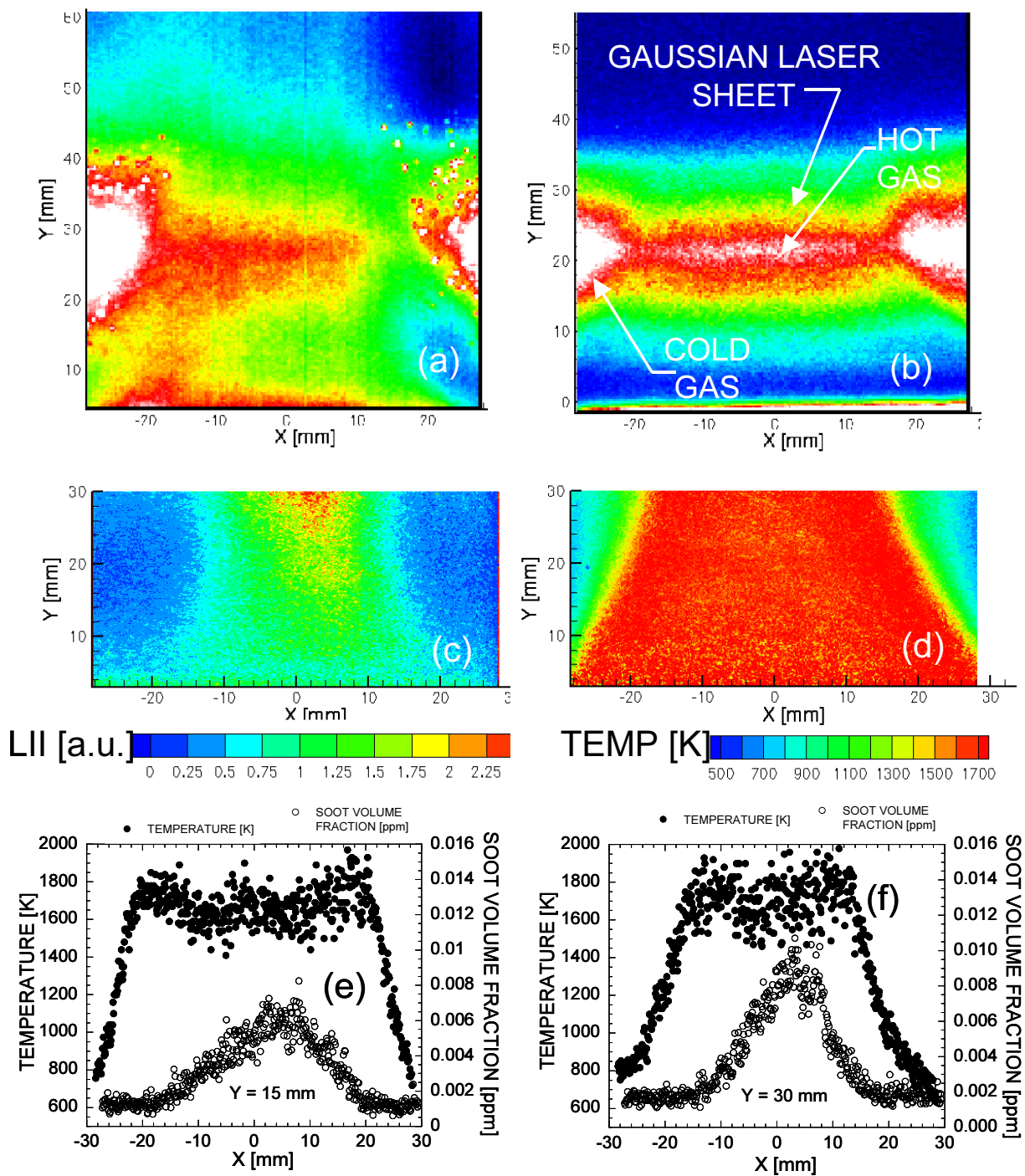
Figure 28 – FRS/LII results from a premixed, sooting C_2H_4-air flame. Flame 1 results at $\phi =$ 2.10: unfiltered Rayleigh image (a), FRS image before background subtraction and normalization (b), qualitative soot imaging by 2-D LII (c), FRS-measured temperature field (d), horizontal profiles of FRS-measured temperature and soot LII at y = 15 and 30 mm (e,f).
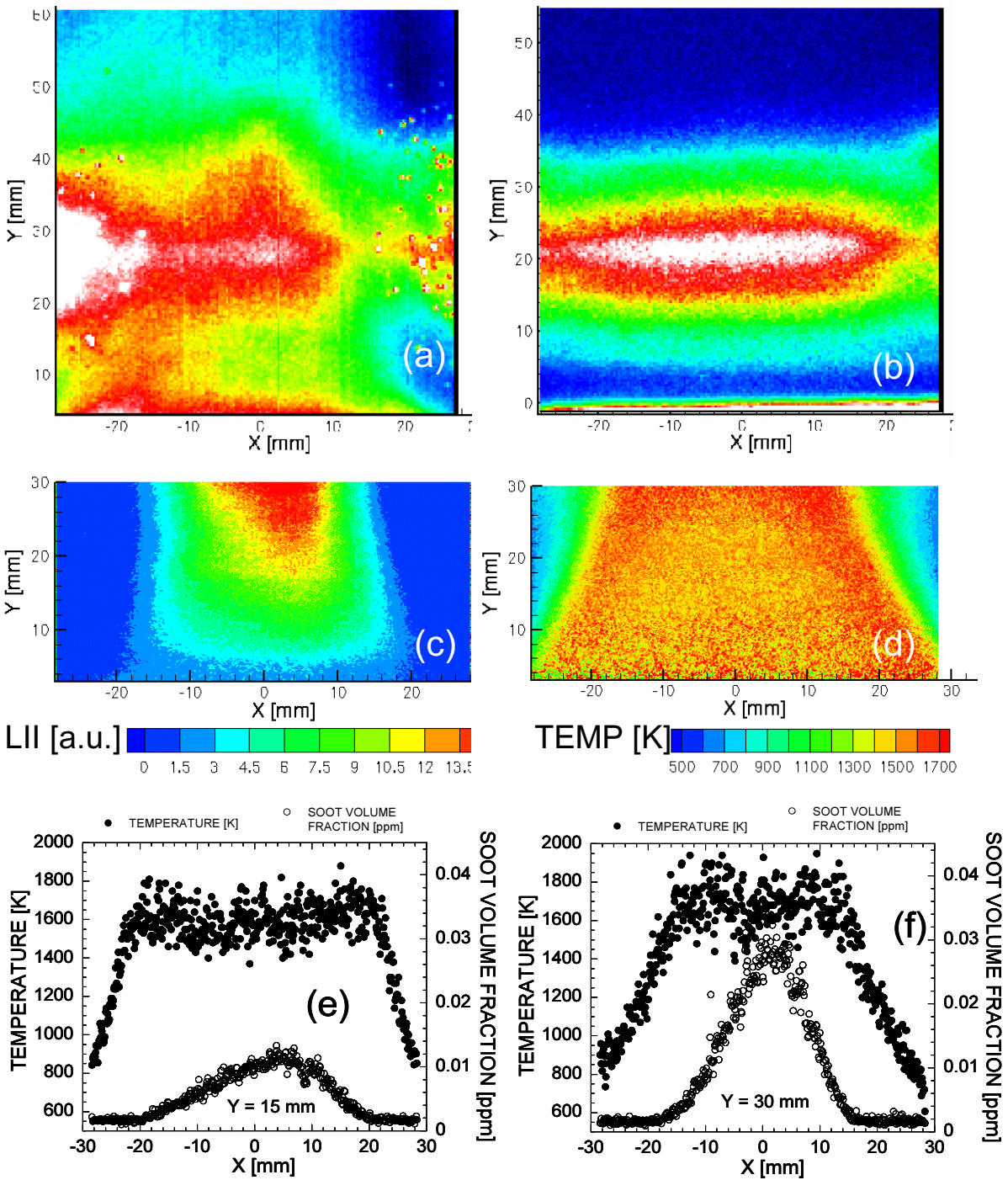
Figure 29 – FRS/LII results from a premixed, sooting C_2H_4-air flame. Flame 2 results at $\phi =$ 2.14: unfiltered Rayleigh image (a), FRS image before background subtraction and normalization (b), qualitative soot imaging by 2-D LII (c), FRS-measured temperature field (d), horizontal profiles of FRS-measured temperature and soot LII at y = 15 and 30 mm (e,f).
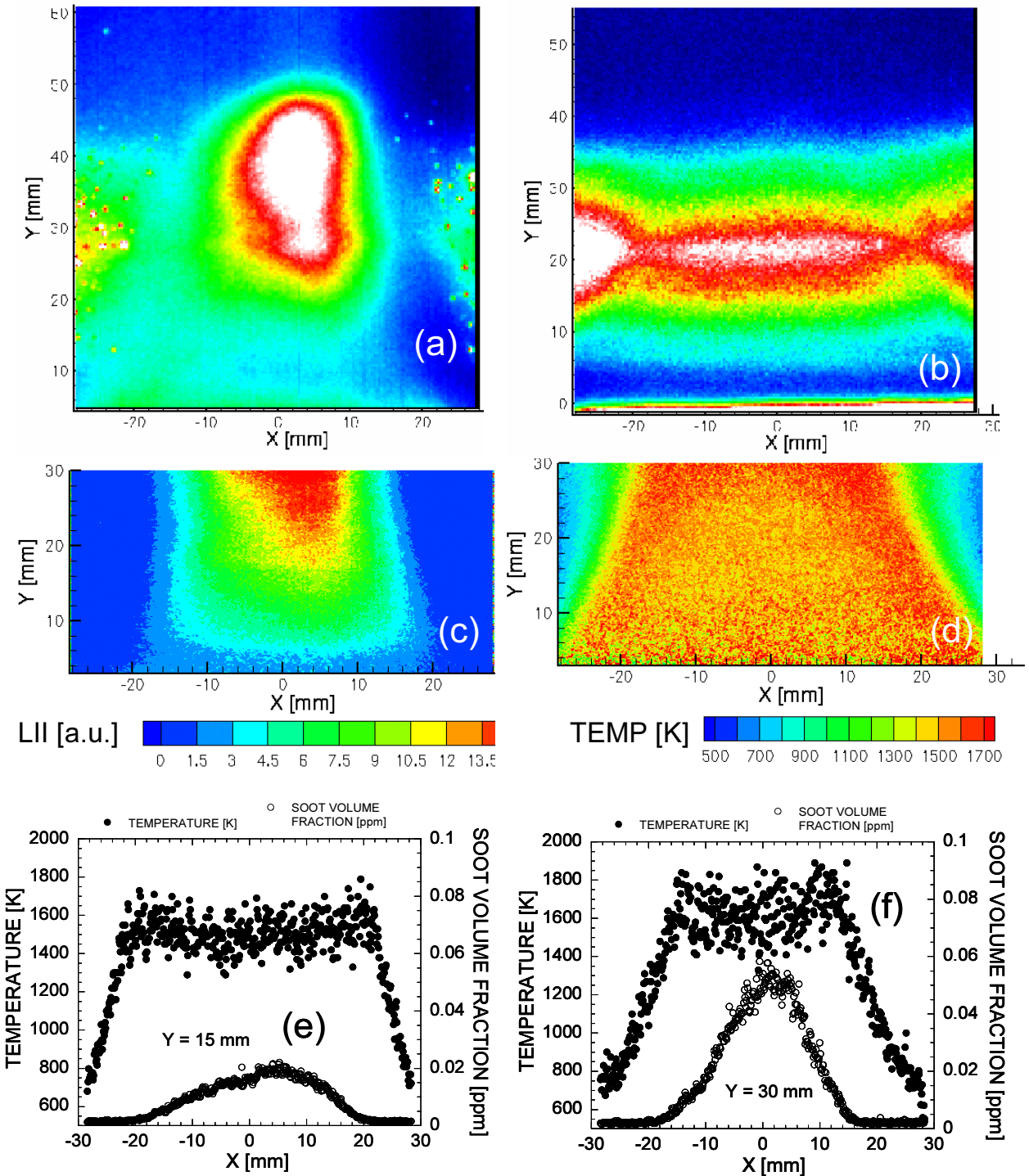
Figure 30 – FRS/LII results from a premixed, sooting C_2H_4-air flame. Flame 3 results at $\phi =$ 2.19: unfiltered Rayleigh image (a), FRS image before background subtraction and normalization (b), qualitative soot imaging by 2-D LII (c), FRS-measured temperature field (d), horizontal profiles of FRS-measured temperature and soot LII at $y = 15$ and 30 mm (e,f).
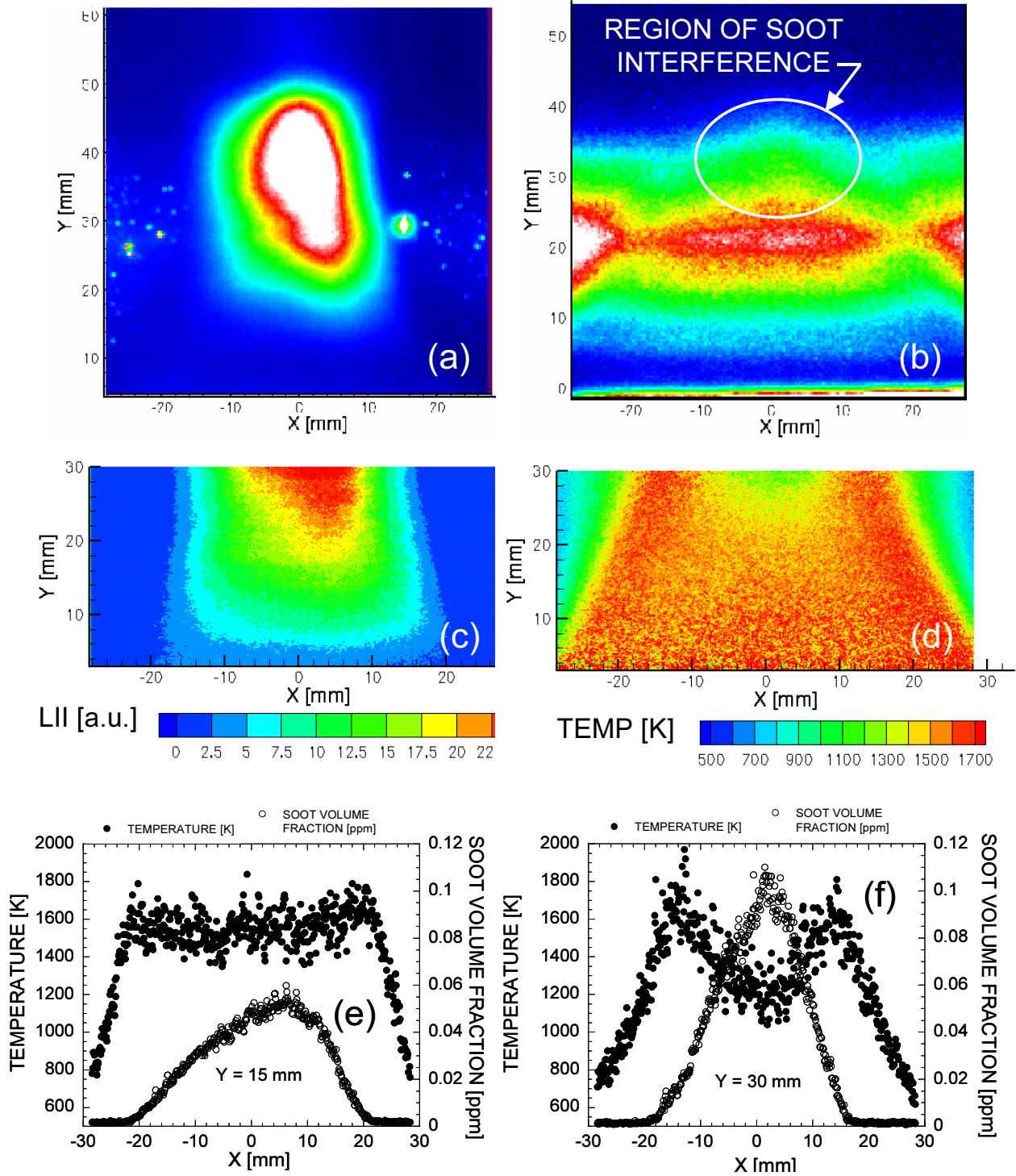
Figure 31 – FRS/LII results from a premixed, sooting C_2H_4-air flame. Flame 4 results at $\phi =$ 2.24: unfiltered Rayleigh image (a), FRS image before background subtraction and normalization (b), qualitative soot imaging by 2-D LII (c), FRS-measured temperature field (d), horizontal profiles of FRS-measured temperature and soot LII at $y =$ 15 and 30 mm (e,f).
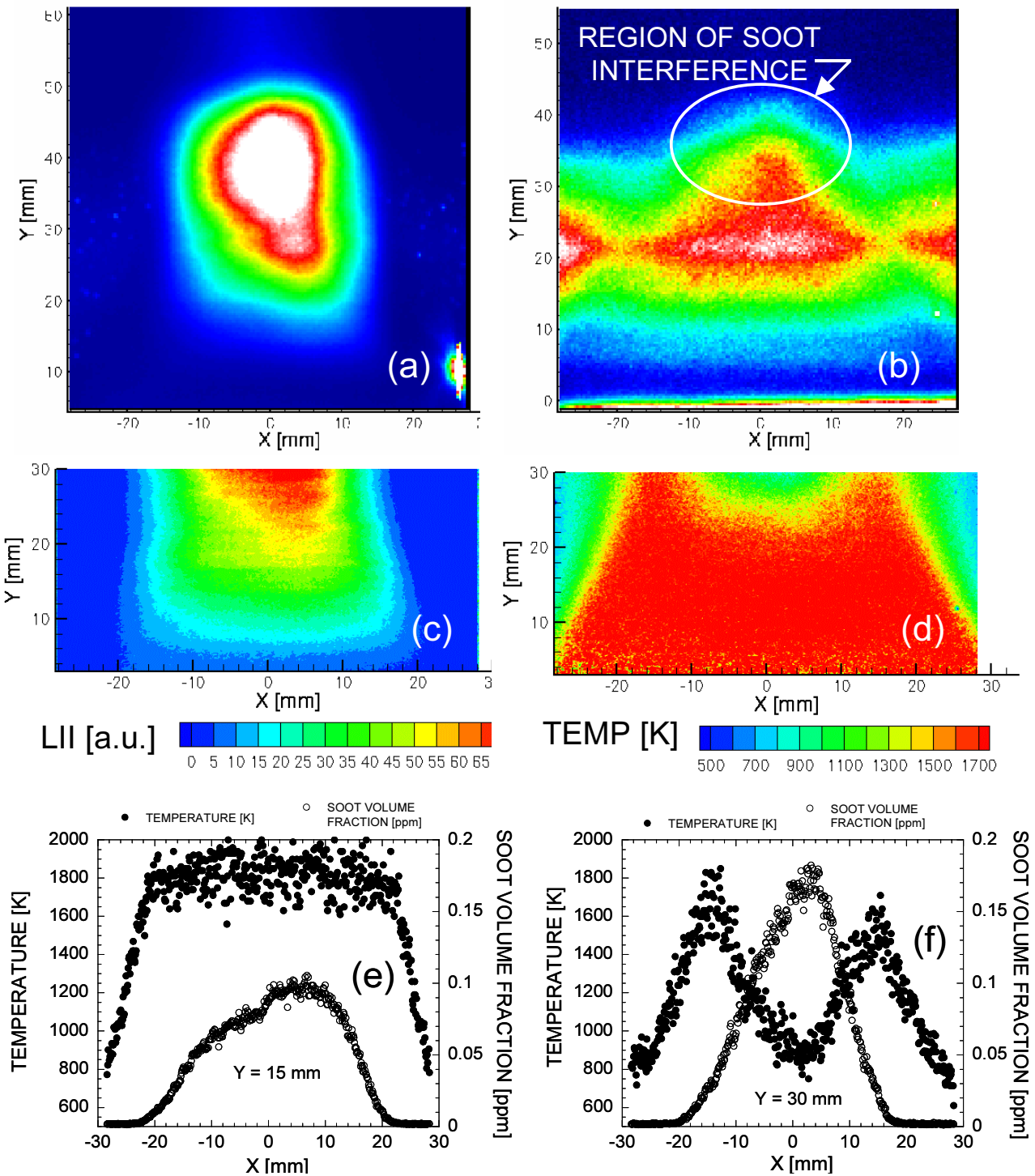
Figure 32 – FRS/LII results from a premixed, sooting C_2H_4-air flame. Flame 5 results at $\phi =$ 2.29: unfiltered Rayleigh image (a), FRS image before background subtraction and normalization (b), qualitative soot imaging by 2-D LII (c), FRS-measured temperature field (d), horizontal profiles of FRS-measured temperature and soot LII at $y =$ 15 and 30 mm (e,f).

Preliminary Assessment of an Upper Soot Loading for FRS Thermometry

One of the chief goals of our FRS investigation in sooting flames is to estimate the maximum level of soot loading for which FRS thermometry remains viable. In principle, the absorption line strength of the R121 (35-0) transition in the 50.8-mm-long I_2 cell used in our work is greater than 10^8 as calculated from the theoretical model of McKenzie [26]. Comparable absorption strengths have been experimentally verified using CW laser sources of extremely narrow linewidth [25]. With an absorption strength of this magnitude, flames with soot loadings of several ppm volume fraction could be investigated with FRS. However, the measured rejection measured with our pulsed Nd:YAG laser is only 10^3. Similarly degraded molecular-filter performance with pulsed lasers has also been reported elsewhere [25, 66].

We believe that this nonideal filter performance is a result of residual mode competition in the Nd:YAG oscillator[+]. This situation is shown schematically in Fig. 33. Fig. 33a depicts the shape of the nominally 1 cm^{-1} wide (FWHM) gain curve of the Nd:YAG laser medium. Within this gain envelope are the different longitudinal modes supported by the laser cavity. When the laser resonator operates without injection locking, all modes within the gain envelope compete for the flashlamp energy stored in the Nd:YAG medium and the laser operates in a multimode fashion. When injection locking is used, the CW seed laser is introduced to the cavity along the resonator axis and tuned to a selected high-gain longitudinal mode. The energy pumping the seeded longitudinal mode is then many orders of magnitude greater than its competitors and the cavity "locks in" to the seeded frequency with greater than 99% of the output in a near Fourier-transform-limited 0.003 cm^{-1} (100 MHz) bandwidth, which is the linewidth that is typically quoted for commercial injection-seeded Nd:YAG systems. The remaining high-gain longitudinal modes then compete for the remaining energy fraction and the resulting spectrum of the laser pulse exhibits a spectrally narrow peak with low-energy "wings" as shown in Fig. 33b. In most laser-diagnostic applications, the small fraction of energy in the pulse wings is not significant. The implications for FRS are more important because the spectral location of the profile wings lies outside the width of the selected I_2 transition. Scattering from soot at these wing frequencies

---

[+] The Fourier-transform linewidth for a 10-ns laser pulse is $\sim 3 \times 10^{-3}$ cm^{-1}. This is roughly a one order of magnitude less than the I_2 absorption linewidth. We have convolved a transform-limited Gaussian laser line with the theoretical I_2 transmission using the code provided by McKenzie [26] and found a negligible degradation of filter performance, thus eliminating the possibility that the decreased coherence of pulsed lasers relative to cw sources is the reason for degraded molecular-filter performance.
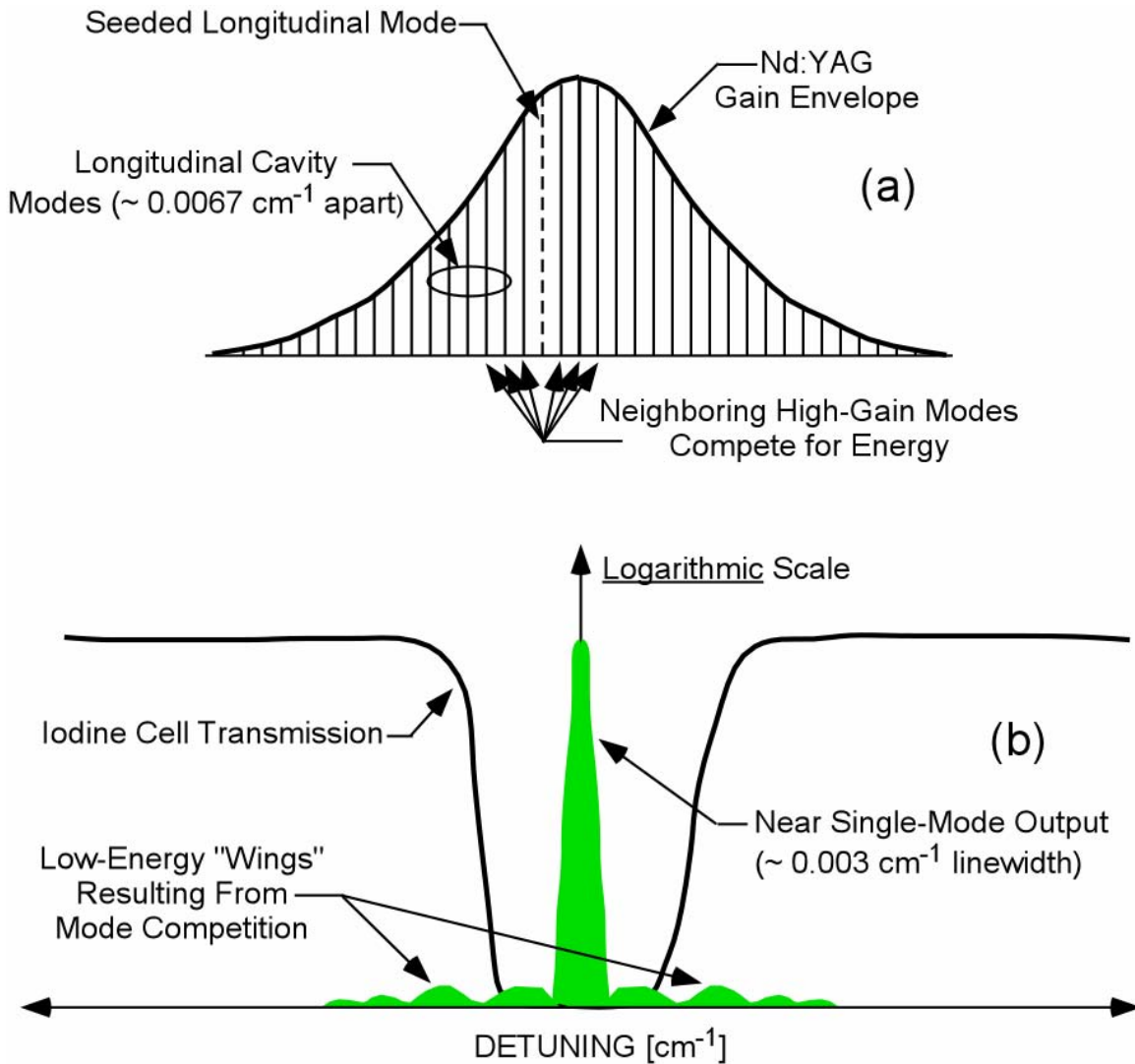
Figure 33 – Illustration of the causes of leakage of pulsed laser light through an optically thick I_2 molecular absorption filter. A schematic of the Nd:YAG gain envelope and the associated cavity modes is shown in part (a). The resulting narrow-linewidth output from the seeded longitudinal mode with low-energy side-lobe leakage resulting from residual energy competition from unseeded longitudinal modes is shown in (b).

can then "bleed" past the I_2 filter and contaminate the FRS images when the soot loading is sufficiently high. This residual-mode-competition explanation is consistent with our observations of the temporal pulse shape of Nd:YAG laser radiation that leaks past line center of optically thick I_2 transitions. The leakage pulse shape was consistently ragged while the unfiltered laser pulse was temporally smooth and indicative of narrow linewidth.

The combined FRS/LII data introduced in the previous section can be interpreted to obtain a first estimate of the upper sooting limit for FRS. Visual inspection of the filtered Rayleigh images in part (b) of Figs. 28-32 can be used to qualitatively assess the performance of the FRS technique for a given flame. In Flame 1, the nominally Gaussian shape of the vertical laser sheet profile is readily observable. The appearance of the laser-sheet profile in Flame 1 is consistent with FRS images recorded in room-temperature air and in nonsooting C_2H_4-air flames, which is a strong indicator that the FRS images from Flame 1 are uncontaminated by Mie scattering from soot. The qualitative appearance of the FRS images from Flames 2 and 3 in Figs. 29(b) and 30(b) is also similarly unaffected. The consistency of the FRS images and the resulting temperature fields for Flames 1-3 suggests that these data sets are minimally impacted by soot Mie scattering, with only imperfect compensation for broadband interference from LII/C_2 playing a potential role.

Flames 4 and 5, which have the highest soot loadings and the most intense unfiltered scattering signals, begin to display an altered vertical laser-sheet profile in the hot-gas zone of the upper portions of the laser-sheet, as indicated in Figs. 31(b) and 32(b). In fact, the FRS signal levels in the hot-gas zone in Figs. 31(b) and 32(b) are larger than the cold-gas signals for the same height above the burner, which is not possible unless the increased signal comes from soot interference. These qualitative observations obtained from the raw FRS images in part (b) of Figs. 28-32 are consistent with soot volume-fraction and particle-size distributions that reach critical levels in Flames 4 and 5 along the $x = 0$ mm flame axis in the vicinity of $y = 20\text{-}25$ mm above the burner surface.

Peak soot volume fractions from the 1-D LII measurements at $y = 15$ and 30 mm are listed in Table 3. The peak soot volume fraction measured with 1-D LII at $y = 30$ mm in Flame 3 is 5.5×10^{-8}, or 0.055 ppm ($\pm 30\%$), and is certainly within the range of applicability for the FRS measurements presented here. The FRS measurements appear to succumb to soot Mie scattering interference along the axis of Flames 4 and 5 for y greater than about 22 mm, where the FRS-measured temperature along the flame axis begins a rapid and physically unrealistic decay. In Flame 4, the peak soot volume fraction at $y = 30$ mm is 1.1×10^{-7}, or 0.11 ppm, and the FRS technique has clearly failed at this location. A similar peak soot volume fraction of 1.0×10^{-7}, or 0.1 ppm, is measured near the flame axis at $y = 15$ mm in Flame 5, where the FRS image in Fig. 32(b) does not appear to be contaminated and the corresponding FRS temperature field in Fig.

32(d) does not exhibit a significant drop in temperature on the flame centerline until $y > 20$ mm. All of this strongly suggests that the FRS signal is not yet contaminated at this location in Flame 5. The similarly measured 0.1-ppm peak soot volume fractions at $y = 30$ mm in Flame 4, where FRS has failed, and at $y = 15$ mm in Flame 5, where the FRS data appear useable, suggests that particle size also plays an important role since younger soot particles of smaller size exist at lower heights in these premixed flames [61].

The corrected 2-D LII images in Figs. 31(c) and 32(c) can be used to obtain an approximate interpolation of the soot-volume-fraction data in the vicinity of the more quantitative 1-D LII results available at $y = 15$ and 30 mm. The initial failure of FRS appears in both Flames 4 and 5 along the flame axis and near $y = 22$ mm. The sheet-corrected 2-D LII images display flame-axis signal levels at 22 mm which are both about 80% of the $y = 30$ mm signal for interpolated volume fractions of 0.83×10^{-7} and 1.1×10^{-7} volume fraction for Flames 4 and 5, respectively. Both of these estimated critical values at $y = 22$ mm suggest that quantitative FRS temperature imaging is possible in lightly sooting flames for soot volume fractions up to about 1.0×10^{-7}, or 0.1 ppm with some secondary dependence on the soot particle-size distribution.

Present Directions for FRS Thermometry for Fire and Combustion at Sandia

Work in FRS thermometry in sooting flames is currently proceeding in the Engineering Science Center at Sandia/NM. The experiments in the sooting, premixed C_2H_4-air flame on the McKenna burner have been repeated with a modified commercial Nd:YAG laser at the Air Force Research Laboratory (AFRL) Propulsion Directorate at Wright-Patterson AFB, Ohio[#]. The laser at AFRL is an injection-locked, pulsed Nd:YAG with an etalon placed in the oscillator cavity. The etalon provides additional line-narrowing to reduce the energy in the spectral "wings" of the Nd:YAG laser pulse (Fig. 33). We have measured a factor of 7-10 improvement in I_2 filter rejection with this etalon-equipped laser system, which has promise for FRS thermometry in more heavily sooting flames. Analysis of the results from the AFRL experiments is ongoing and the data have not been prepared for publication at the time of this writing. Repeat FRS measurements and a more vertically resolved quantitative 1-D LII characterization of the soot

---

[#] We would like to thank Cam Carter of the Air Force Research Laboratory, Wright-Patterson AFB, OH and Jim Crafton of Innovative Scientific Solutions Inc., Dayton, OH for their generous help in performing these sooting flame measurements with their specialty Nd:YAG laser.

field in the C_2H_4-air McKenna flames is also being conducted as part of an ongoing ESRF Tech-Base effort at Sandia/NM. As part of this effort a significantly shorter ICCD gate will be used to better reject broadband interference from soot LII, C_2, and PAH and the premixed flame will be better stabilized to minimize any cold-gas density weighting bias in the results. As part of this ESRF effort, the FRS data will also be supplemented by CARS-measured temperatures so that a better quantitative assessment of the FRS accuracy in sooting flames may be obtained.

It is also our plan to utilize FRS for temperature imaging in moderately sooting, vortex-strained diffusion flames supplied by a Wolfhard-Parker slot burner that is similar to the one shown in Fig. 14. These measurements will be supplemented with UV Raman imaging of the fuel molecule using the approach reported by Rabenstein and Leipertz [52] in which a 355-nm third harmonic of the Nd:YAG laser is used to provide fuel Raman signals in the blue that can be spectrally separated from soot optical interference. These UV fuel-Raman data will be used to correct the FRS images for local variations in Rayleigh cross section using the same tools developed for the nonsooting vortex-strained flames and presented in this report. The sooting diffusion-flame work supports ongoing efforts at Sandia that are directed toward modeling soot formation in nonpremixed flames and in large-scale pool fires. FRS thermometry for clean combustion systems is also being introduced for DOE/BES programs at the Combustion Research Facility at Sandia/CA [42].

FRS VELOCITY IMAGING MEASUREMENTS

Experimental Procedure

Iodine Cell Calibration

Prior to collecting data, the iodine cells must be scanned in frequency to provide the transmission profiles of each cell, a process referred to as calibration. Before this can be initiated, however, the two photodiodes in the frequency monitor must be calibrated to one another to ensure that the reference photodiode responds to the laser beam identically to the signal photodiode. Variations in the optical arrangements for each beam path, nonuniform beamsplitter ratios, differing photodiode responses, and slightly different integration times for the gated integrators all contribute to discrepancies from one photodiode signal to another. Similarly, the two photodiodes in the calibration station must be calibrated to one another; this calibration station and the frequency monitor function independently though simultaneously and therefore the four photodiodes need not all be calibrated to one another. The calibration was accomplished by removing both iodine cells from their calibration positions, then recording the signals from the gated integrators for each photodiode as the incident laser power was cycled through a range of intensities. Background signals can pose a difficulty and must be accounted; curtains and beam blocks were employed to shield each photodiode from stray laser light and the remaining background signal was subtracted from each photodiode by adjusting the zero offset on each gated integrator. Once data points were collected for a range of laser intensities, the response of one signal photodiode was mapped to its reference photodiode using a linear least-squares fit.

Subsequent to the photodiode calibration, the two iodine cells were calibrated by replacing the cells into their calibration positions and spectrally scanning the laser frequency by sequentially adjusting the seeder input voltage. The gated integrator signal from each of the now-calibrated photodiodes was recorded, transformed by the linear least-squares fit found for each photodiode pair, and reduced to a frequency-dependent transmission ratio that provides the spectral characteristics of each iodine cell. The cell calibrations can be a time-consuming process because the laser must be given adequate time for the injection seeding to stabilize between each adjustment of the frequency. Hence, the iodine cells were scanned thoroughly at the start of the experiments and then only briefly each day during actual data collection to be

certain that the experimental apparatus was functioning properly and that the pressure-broadened cell had not leaked.

The pressure-broadened iodine filter used for the signal camera was scanned at several different buffer-gas pressures to evaluate different absorption line shapes for use in velocity measurements both in the present work and in future hypersonic endeavors. To establish the cell conditions, first the temperature at the cell's side arm was reduced to 1°C so that all the iodine solidified into crystal form at this location, then the remaining gaseous contents were evacuated using a vacuum pump. An ultra-pure nitrogen source was bled into the cell until the desired buffer-gas pressure was achieved, then the temperature of the side arm was raised back to 45°C. It was found that at substantial buffer-gas pressures, approximately one day's time was required for the iodine to penetrate back into the cell from the side arm and return to equilibrium. The cell was sealed from the side arm after such time had elapsed, eliminating the need for continued control of the side-arm temperature.

Camera Calibration

Analogous to the photodiode calibrations, the two cameras must be calibrated to one another to ensure that each pixel on one camera views the same physical location as the corresponding pixel in the other camera and possesses an identical response to the intensity of the scattered light. In practice, it is not possible to position each camera such that they achieve identical imaging regions, so the two cameras are digitally aligned to one another in post-processing, a procedure that also corrects any perspective distortion due to the camera viewing angle with respect to the laser sheet. To achieve this, a dot card is temporarily placed in the same position as the laser sheet, providing a uniform array of tie-points at which the images from each camera can be matched. This procedure by necessity was performed with the iodine filter cell in place before the signal camera, because it provides a small but distinct lensing effect that would alter the images and hence the spatial mapping if it were removed.

The software used to map one camera to the other was developed in-house. Dots in each image were located using a polynomial fit to find the center, then were matched to one another with the aid of user input. This information allowed a bilinear interpolation to warp each image onto a uniform rectilinear grid common to each of the two cameras. A similar algorithm is described in detail in Elliott and Beutner [25] or Crafton *et al.* [67].

To map the intensity response of the two cameras, the dot card was replaced by a white card and illuminated by an expanded and spatially filtered beam from the laser. Because the illumination is dependent upon the laser frequency and its absorption by the iodine cell, the white card is not a standard flat-field correction and thus is often called a green card. The laser frequency was tuned to a point outside any iodine absorption wells so that small variations in the laser frequency would not appreciably influence the absorption of the cell (note that even away from an absorption line, significant absorption of a constant magnitude occurs due to the nonresonant background of the iodine molecule [26, 29]). The laser was stepped through ten intensity values over the range anticipated for the laser light scattered from the ethanol-seeded jet and ten images were acquired at each intensity.

The green card data processing was begun by lightly filtering the images to reduce laser speckle effects (a small amount of filtering was found to significantly improve the intensity match between the two cameras achieved by the transformation), then background images were subtracted from each green card image to correct for room light and camera dark current. Each set of ten images was averaged together to produce a single image at each laser intensity, further reducing the impact of laser speckle, while bypassing pixels that were saturated or nearly so. The build-up time reduction of the laser was continuously monitored to remove images at which the injection-lock of the laser was lost, which could impact the absorption through the iodine cell even though the laser is tuned outside an absorption line. Once all ten averaged image pairs were obtained, they were spatially transformed using the results from the dot card images to give both images in each pair an identical field of view. Finally, they were subjected to a linear least-squares fit on a pixel-by-pixel basis analogous to the one utilized for the photodiodes, wherein the measured intensities of the signal camera were fit to those of the reference camera. This array of linear transformations allowed each signal image to be mapped to its matching reference image in intensity following its spatial transformation.

Data Reduction

The initial step in reducing the pairs of signal and reference data images was to lightly filter each image to reduce laser speckle effects, in the same fashion as with the filtering of the green card images. Background images were acquired with the laser operating but the jet dormant to account for stray laser illumination, room light, and the camera dark current; these were

subtracted from each data image. These backgrounds were obtained with the laser tuned to the same frequency at which the data images would be acquired to ensure that absorption of stray laser light through the iodine cell would be consistent. Each image pair was spatially and intensity transformed according to the procedure described above using dot card images and green card images collected just prior to data acquisition.

Each pixel in the transformed signal image was divided by the identical pixel in the reference image to yield a transmission ratio, from which the frequency of the scattered light was found by consulting the iodine cell calibration for the signal camera, as in the sketch in Figure 4b. The frequency of the incident laser light for the corresponding laser pulse was found from the transmission ratio recorded from the frequency monitor and the cell calibration for that iodine cell. The difference between these two frequencies provides the Doppler shift. The velocity in the direction of the system sensitivity is then found from the equation

$$V_c = \frac{\lambda}{2\sin\left(\frac{\phi}{2}\right)}\left(\nu_s - \nu_i\right) \tag{13}$$

where V_c is the velocity component to which the DGV system is sensitive, λ is the wavelength of the laser, ϕ is the angle between the incident light vector and the scattered light vector (which is known from the experimental configuration), and ν_s and ν_i are the frequencies found for the scattered and incident light respectively.

Strictly speaking, ϕ is not constant, as it can vary if the incident or scattered light vectors change. Because the laser sheet has been collimated before reaching the jet, the incident light vector is constant. However, the collection angle varies across the image, creating a variation in the scattered light vector $\hat{s}$ that induces a small alteration in ϕ and in the velocity sensitivity direction. This effect is a function of the pixel location and hence can be calculated at each point to remove the associated error, but this capability has not yet been introduced into our software. Operating the 105-mm lenses at f/8, the variation in $\hat{s}$ is $\pm 7°$, which yields a significant error if this bias is neglected. However, because the jet is small and the optical path length is fairly large to accommodate the required collection optics, the jet filled only a portion of the images. The variation in $\hat{s}$ over just this region is only about $\pm 1°$, which induces a similar change in the velocity sensitivity direction, for which the estimated error in the measured velocity is 1%.

Results

Iodine Cell Calibration

Prior to acquiring data, frequency scans were taken of each iodine cell, including scans of the pressure-broadened cell at various buffer gas pressures to select the best conditions for the present experiment and for future hypersonic studies. Figure 34 shows scans of the absorption line near 18789.3 cm^{-1} for four cases, in which one has no pressure broadening and the remaining three display the effects of increasing the partial pressure of nitrogen. In each case, the side-arm temperature was 45°C and the cell body temperature was maintained at 100°C. The vertical scale of the plot has not been normalized to the maximum transmission and the frequency axis is relative to the minimum of the absorption line recorded by the frequency monitor iodine cell, which was scanned simultaneously. This allows the permanently sealed cell to serve as a fixed frequency reference to the changing conditions in the pressure-broadened cell, whose line position does not necessarily match that of the sealed cell. The scale of the frequency axis was determined by matching a wider scan of the sealed cell to the theoretical spectrum predicted by Forkey's model [27, 29] to convert to frequency the voltage scale specific to our laser. The profile of the iodine cell used in the frequency monitor appears similar to the profile with no nitrogen addition shown in Figure 34, but has less absorption because the side-arm temperature was 35°C as compared to 45°C for the camera filter cell.

Because the absorption profile has not been normalized, any additional losses from the filter cell windows are included. These losses will be small; the maximum transmission is well below unity due to a background nonresonant absorption present in the iodine spectrum [26, 29]. The strength of this nonresonant background appears to increase as the nitrogen pressure is increased, but this is probably because the broadening of adjacent lines blends with the line shown in Figure 34. The figure also shows the line shift evident at the minimum of the absorption lines that occurs when a line is broadened due to the presence of a buffer gas. This effect has been previously reported in iodine by such authors as Padrick and Palmer [68], Mukhtar *et al.* [69] and Fletcher and McDaniel [70] but has not been discussed previously by DGV users. The centers of the shifted absorption lines are marked with dashed lines in Figure 34.

The line shift shown in Figure 34 demonstrates the importance of calibrating the frequency monitor iodine cell simultaneously with the pressure-broadened camera iodine cell. If the cells
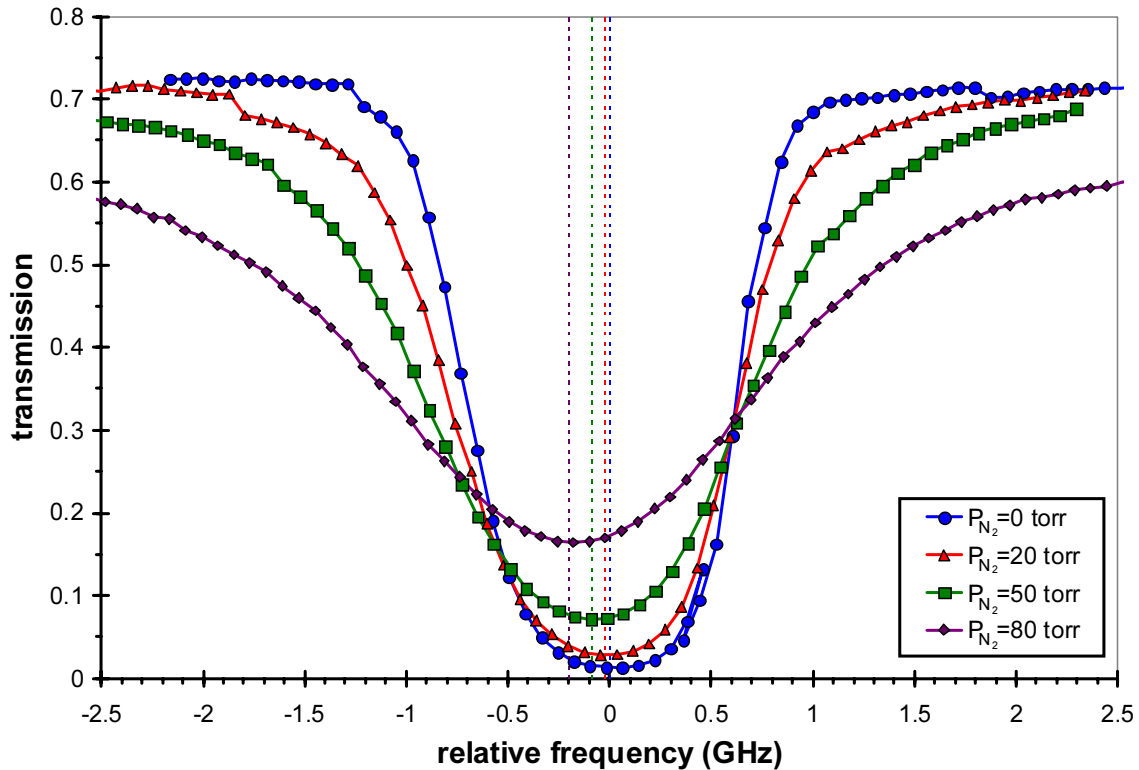
Figure 34 – Frequency scans of the iodine absorption line near 18789.3 cm^{-1} showing the effects of pressure broadening as the partial pressure of nitrogen buffer gas is increased. The vertical dashed lines show the line shift of the minima for each condition.

were calibrated independently and then each referenced to its own minimum, the line shift would be overlooked and a bias would be introduced into the velocimetry measurements. This arises because the velocity is measured by the frequency difference between the transmission ratio determined from the camera iodine cell and the transmission ratio determined from the frequency monitor. Thus the frequency scales of each cell must be referenced to a common point and the presence of line shift in a pressure-broadened cell inhibits use of the absorption line location as such a reference.

Mach 3.7 Jet Measurements

For the purposes of flow visualization, initial images were taken in a plane aligned with the jet axis and therefore normal to the jet exit plane (not the skewed laser sheet shown in Figure 9). A sample instantaneous image and a mean image are shown in Figure 35 for the Mach 3.7 jet. The exit plane of the jet lies just below the images. The initial shock diamonds are distinctly
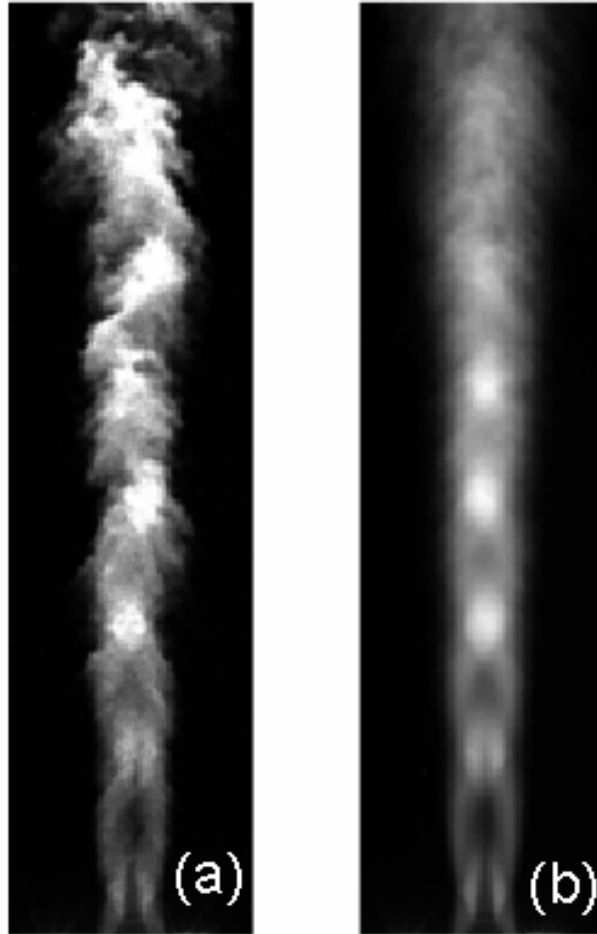
Figure 35 – Unfiltered Rayleigh scattering images acquired in a plane aligned with the jet's centerline axis. The jet exit plane lies just below the bottom of each image. (a) sample instantaneous image; (b) mean image. The position of the inclined laser sheet is shown in (b).

visible in both the instantaneous and the mean image, which gradually erode further downstream as the effects of mixing become strong.

Figure 36 displays sample instantaneous and mean unfiltered images acquired using the inclined laser sheet drawn in Figure 9. The approximate position of this sheet is shown in Figure 35b for reference. The images shown have been spatially and intensity transformed, which removes the perspective distortion created by angling the laser sheet with respect to the camera. The shock diamonds seen in Figure 35 are visible within the inclined imaging plane of Figure 36 as well, seen as the greater intensity region in the central portion of the images. This must lie downstream of oblique shocks where the gas density is higher and hence the ethanol fog density is greater.
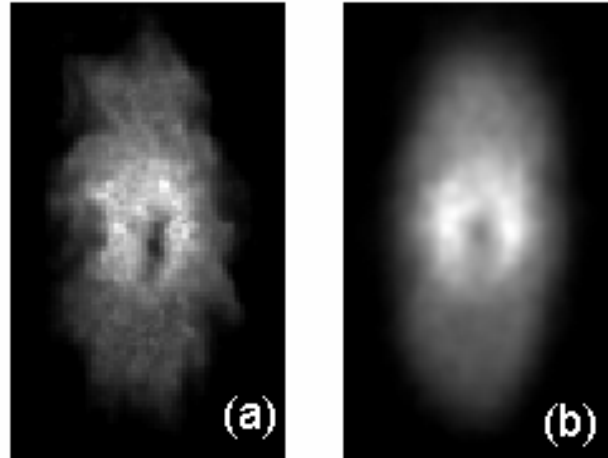
Figure 36 – Unfiltered Rayleigh scattering images of the Mach 3.7 jet acquired in the inclined laser sheet plane shown in Figure 9a. (a) sample instantaneous image; (b) mean image.

Both images shown in Figure 36 were acquired by the signal camera but with the laser tuned outside any absorption line. Images taken by the reference camera were subject to a significant degree of defocus. As the focus was ideal during the set-up procedure, this apparently was the result of a distortion of the pellicle beamsplitter induced by pressure changes when the jet was operated. Efforts to protect the pellicle using additional windows on the beamsplitter mount did not appreciably improve the situation. The signal camera was never affected and attempts to compensate for the focal change by adjusting the camera focus prior to running the jet were unsuccessful. Fortunately, DGV does not require a sharp focus to obtain velocity measurements and the loss of focus principally acted as an additional filter on the images. Subsequent experiments have utilized a cubic beamsplitter to avoid this difficulty, but this change to the system components could not be instituted in sufficient time for application to the jet measurements.

Velocity data have been acquired with the directional sensitivity in the imaging plane shown in Figure 9a. About 30 runs were conducted and mean velocities were computed for quantities between 15 and 36 image pairs per run. Figure 37 shows an instantaneous velocity map for one of the DGV images as well as the mean velocities for the run in which it is a part. Such results are representative of other runs.
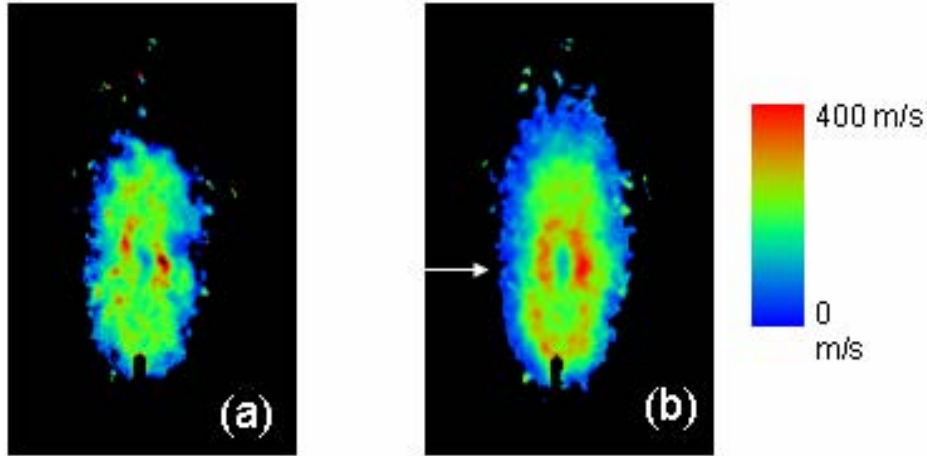
Figure 37 – Velocity images of the Mach 3.7 jet acquired from a sequence of DGV image pairs. Data are shown with the directional sensitivity and imaging plane shown in Figure 9a. The notch at the bottom of the jet was caused by a reflection of the laser sheet. (a) sample instantaneous image; (b) mean image. The white arrow in (b) indicates the position of the horizontal cut plotted in Figure 38.

Figure 38 shows a horizontal cut through the mean velocity data of Figure 37 at the point where the inclined imaging plane crosses the nominal centerline axis of the jet. This point is indicated with an arrow in Figure 37b and occurs 11.3 mm above the exit plane of the jet. The solid line is the mean velocity of the entire run, formed from 27 instantaneous DGV images. The open circles are the data points from each of those instantaneous images. Clearly, a substantial degree of scatter exists for the instantaneous data, which is a result of both measurement uncertainty and turbulent fluctuations in the jet. The shock diamond structure of the jet is sufficiently unsteady that the shocks and expansions are located in different positions for each data realization, contributing greatly to the data scatter. This shock unsteadiness can be observed in sequences of Rayleigh scattering images such as that shown in Figure 35a and in the blurriness of the second shock diamond in the mean image of Figure 35b. Turbulent mixing also is a contributor. The asymmetry across the jet centerline is real and repeatable, not a result of a misalignment of the laser sheet or other optics.

At first glance it seems conceivable that this asymmetry actually may be a result of the off-axis direction of velocity sensitivity, which may incorporate a positive radial velocity component on one side and a negative component on the other, thus skewing the velocity profile from what may be symmetric in the streamwise direction. However, the radial velocity component to which the optical configuration is sensitive lies normal to the linear slice shown in Figure 38, which
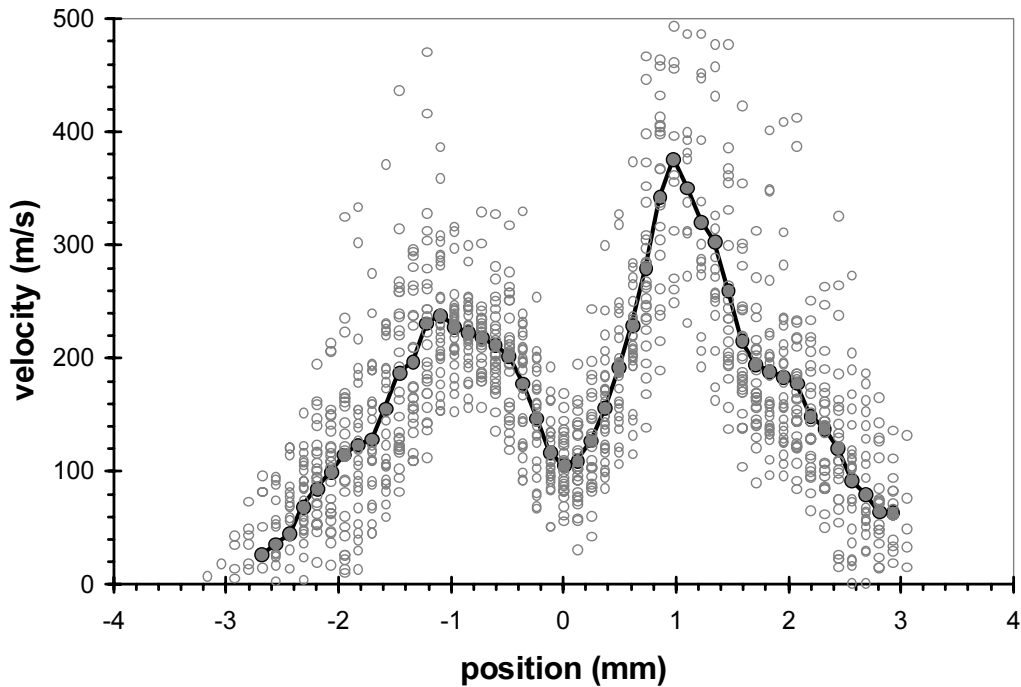
Figure 38 – Plot of the velocities along a horizontal cut through the mean velocity data of Figure 37 at the point where the inclined imaging plane crosses the centerline axis of the jet. The solid line represents the mean velocity and the open circles are the data points from the individual instantaneous DGV images comprising the mean.

would require a significant degree of swirl to induce the asymmetry. Such swirl seems unlikely for the present jet apparatus, and therefore the observed asymmetry is likely not a product of the instrumentation.

Fifteen different runs were taken with the jet stagnation pressure at the same condition. Mean velocity images were compiled from the instantaneous DGV images for each of these runs, then the mean of these means was computed. Figure 39 plots the same horizontal cut through the data as was shown in Figure 38, displaying the mean of these 15 runs and each of the runs comprising it. The data scatter is much less than Figure 38, indicating that the repeatability of the jet flow and the measurements is fairly good, again displaying the same jet asymmetry. Horizontal cuts taken at other vertical positions (which therefore do not lie on the jet axis) are shown in Figures 40 and 41. These show that 0.5 mm downstream the jet becomes much more symmetric, then another 0.5 mm thereafter becomes asymmetric in the direction opposite that seen in Figure 38. However, because these downstream horizontal cuts occur off the nominal jet axis, they experience more complex radial velocities. The varying asymmetry seen in Figures 39
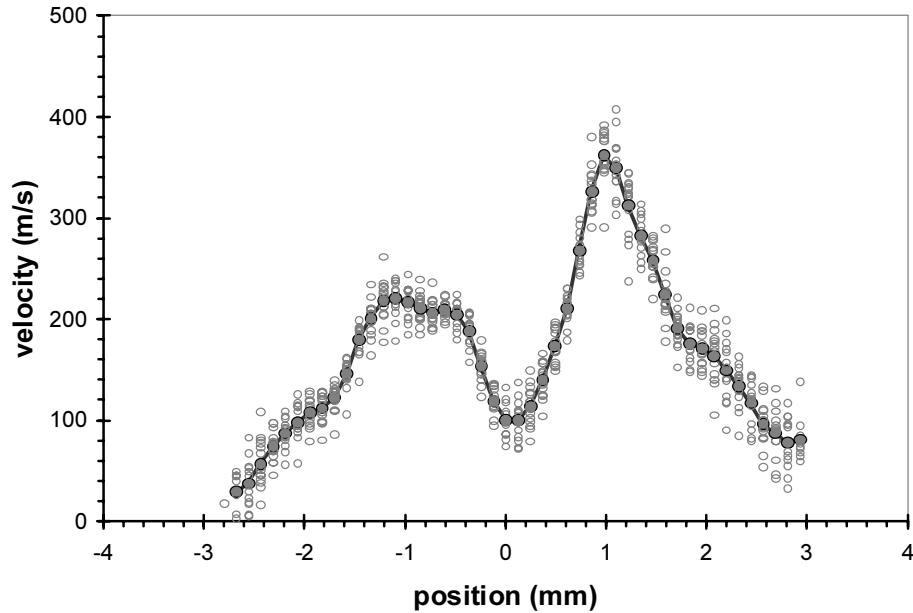
Figure 39 – Plot of the mean velocities along the same horizontal cut as Figure 38. The solid line represents the mean velocity taken from 15 separate runs and the open circles are the data points for the mean velocities of each of those 15 runs.

through 41 possibly is a result of asymmetric flow separation within the nozzle, which yields a skewed pattern of shock diamonds. The nature of the asymmetry, then, would be dependent upon the downstream location and the position the within the shock diamond.

Following the inviscid analysis of Romine [17], it can be shown that the lowest jet axial velocity occurs after passing through a Mach disk at the jet centerline, which yields a downstream velocity of 153 m/s for the present flow conditions and geometry. The largest velocities near the Mach disk can be expected to have originated from an oblique shock generated at the separation point within the nozzle, which yields a downstream velocity of 463 m/s. In inviscid analysis, these velocities will repeat at subsequent shock diamonds. Along the horizontal cuts displayed in Figures 38 and 39, any radial velocities would be expected to occur parallel to the plotted axis because it passes through the jet centerline, and as shown in Figure 9a, the DGV system is not sensitive to velocities in this direction. Therefore, the velocities measured in this configuration should be sensitive only to jet axial velocities and are found as $V_c = V_a \cos(31.5°)$, where V_c is the DGV velocity sensitivity and V_a is the jet axial velocity. The minimum and maximum velocities predicted by gas dynamics, then, are reduced to 130 m/s and 395 m/s, respectively, in the direction of DGV velocity sensitivity. While such inviscid analysis

is of limited utility given the viscous mixing present in the jet, the velocities are measured in the second shock diamond downstream of the nozzle exit and thus these predicted velocities provide a reasonable estimate of those expected from the DGV measurements. The data in Figures 38 and 39 are consistent with such estimates.

Data have been acquired for the radial velocity component using the optical configuration drawn in Figure 9b, but these data have not been fully reduced at the time of this writing.
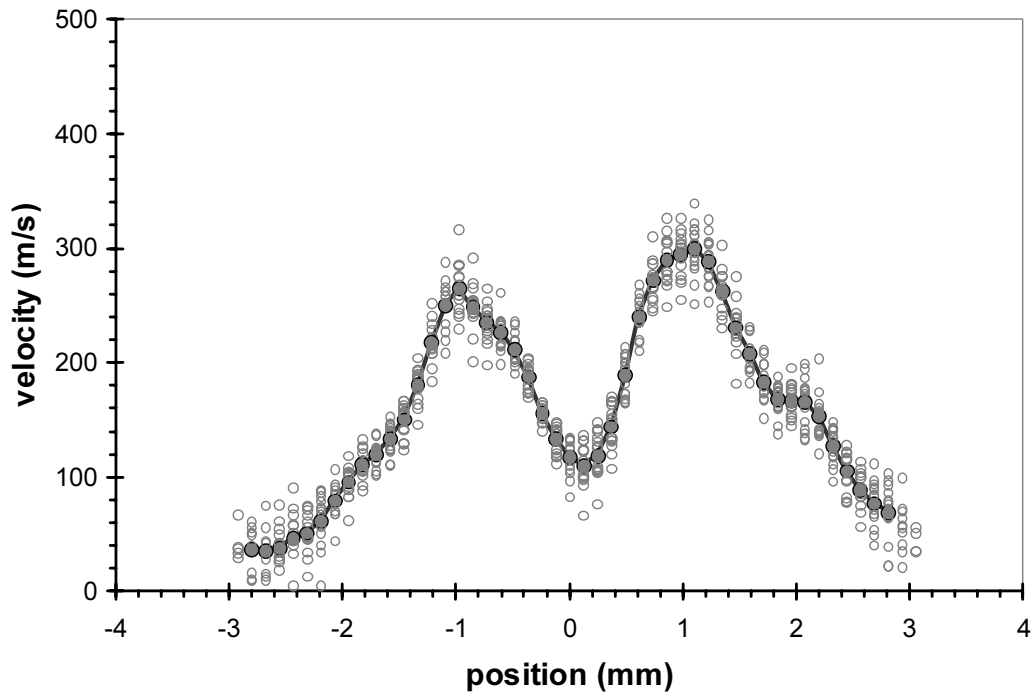
Figure 40 – Plot of the mean velocities along a horizontal cut 0.5 mm above that in Figure 39. The solid line represents the mean velocity taken from 15 separate runs and the open circles are the data points for the mean velocities of each of those 15 runs.
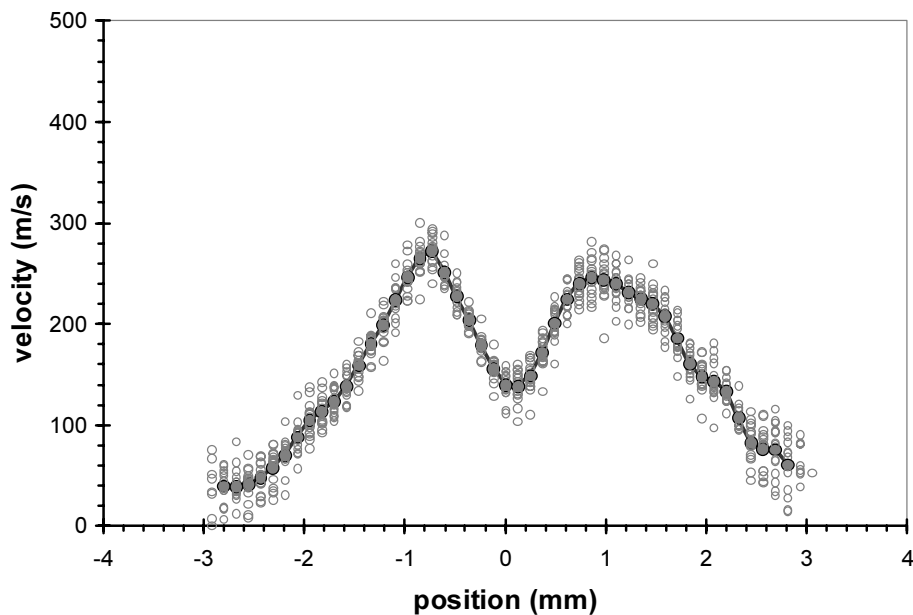
Figure 41 – Plot of the mean velocities along a horizontal cut 1.0 mm above that in Figure 39. The solid line represents the mean velocity taken from 15 separate runs and the open circles are the data points for the mean velocities of each of those 15 runs.

Transitioning DGV to the Sandia HWT

To conduct DGV measurements in the HWT, a new measurement system has been constructed independent of that used for the developmental process. This route was taken to allow the original system to continue to be used to acquire temperature measurements in a laboratory environment while DGV measurements proceeded simultaneously in the HWT. To this end, a new injection-seeded Nd:YAG laser was purchased (Continuum Precision II 8000) and installed in a newly-constructed laser laboratory integrated with the HWT facility. Duplicates of the optics and instrumentation used in the initial system were purchased and installed as part of the system for the HWT, with the notable exception of the PixelVision CCD cameras, which were not required for the temperature instrumentation and hence could simply be relocated to the HWT system. A photograph of the DGV system for the HWT is shown in Figure 42; the schematic would be identical to that shown in Figure 7 except that the jet is replaced by the HWT test section.
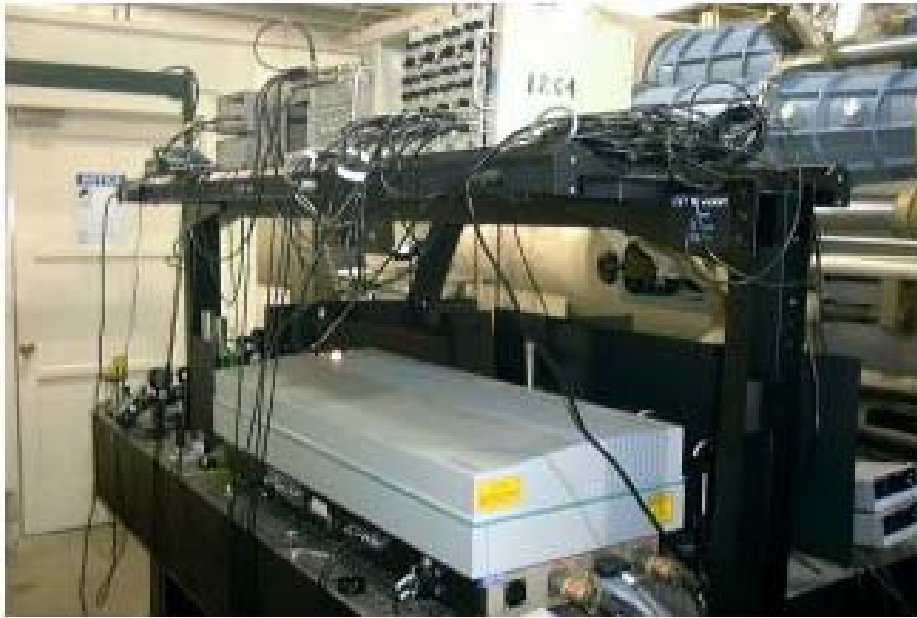
Figure 42 – A photograph of the optical configuration of the DGV system for the HWT.

Additional improvements to the system were made based upon experiences with the developmental system used in the supersonic jet measurements. These included removal of the pellicle beamsplitter in favor of a cubic beamsplitter, as the pellicle was found to have an undesirable impact upon the focus of the reflected light scattered from the jet. Also, the green card calibration procedure that was used to correct for differences in intensity response of the two cameras has been altered. As described earlier, the intensity response was normalized by projecting laser light at frequency tuned away from an iodine absorption line upon a white card placed in the position of the measurement laser sheet. Images then were acquired from each camera for a sequence of laser intensities to generate a calibration for each camera pixel. However, it was found that beam nonuniformities in the laser light projected upon the white card added a significant quantity of noise to the calibration, and furthermore, it was difficult to spatially filter the powerful pulsed laser beam – several spatial filters were destroyed in the attempt. An attractive alternative is to remove the white card and projected laser beam and instead utilize the measurement laser sheet scattered off small smoke particles introduced into the HWT test section during the calibration process. This approach, favored for the DGV measurement system in the HWT, reduces the errors in the camera intensity calibration.

The ethanol seeding system used for the lab-scale Mach 3.7 jet had to be dramatically altered for use in the HWT. The condensate chemical must be introduced upstream of the wind tunnel's heaters, which eliminates the possible use of a flammable chemical such as ethanol. A logical replacement is carbon dioxide, which will condense into a solid phase at the low temperatures found in the HWT test section. However, while the Mach 5 nozzle for the HWT uses nichrome heaters, the Mach 8 and 14 nozzles use tungsten heaters. The presence of oxygen in the flow can cause a chemical reaction on the tungsten heater wires leading to their overheating and rupture, but Mach 8 and 14 flowfields employ nitrogen as a test gas rather than air and thus eliminate this concern. While the heaters for Mach 8 and 14 operate at temperatures lower than that at which carbon dioxide may dissociate to produce oxygen, the heaters may possess hot spots at which such dissociation could occur locally. For this reason, carbon dioxide seeding was deemed appropriate only for the Mach 5 nozzle; a different gas would be necessary for Mach 8 or 14.

The DGV system would be implemented only for the Mach 5 test section within the scope of the present work. A schematic of this seeding system is shown in Figure 43. Two "six-packs" of carbon dioxide cylinders provide the supply gas, which is regulated to the necessary pressure to

drive the gas into the air supply line leading to the wind tunnel. By seeding the carbon dioxide into the supply line upstream of the HWT control valves, stagnation chamber, and heaters, adequate distance is provided for the carbon dioxide to mix with the primary flow and thus create a reasonably uniformly seeded flow. A high-flow rate regulator is employed to produce the desired seeding pressure. The carbon dioxide is switched using two cryogenic valves to ensure that any freezing during the carbon dioxide expansion does not cause the valve to stick. One of these valves is used for control during a wind tunnel run while the other is interlocked to the HWT's downstream vacuum valve, thus ensuring that the seeder cannot be operated unless the HWT is exhausted to vacuum and thus preventing against overpressurization. Oxygen monitors are used to detect any leaks into the laboratory. Construction of the carbon dioxide seeder is complete at the time of this writing and undergoing testing under a variety of flow conditions.

A photograph of the HWT is shown in Figure 44. Implementation of laser operations has necessitated construction of an interlocked room around the test section to enclose laser light scattered from the test section to the cameras (not shown in the photograph). The laser beam must be brought from a similar interlocked laser lab on the opposite side of the wind tunnel over the dormant test sections mounted on the rotary arrangement for the tunnel. At the time of this writing, an enclosed laser tube is being constructed over the entire HWT to pipe the beam from one room to the other, including remotely-controlled laser mirrors to guide the beam. Beam-shaping optics similarly are to be shielded from view for wind tunnel personnel. Construction of the optical apparatus for the HWT, begun in the final year of the current project, is expected to be complete in the first quarter of FY04 under a program continuing the DGV work. The first laser-based images will be acquired shortly thereafter.
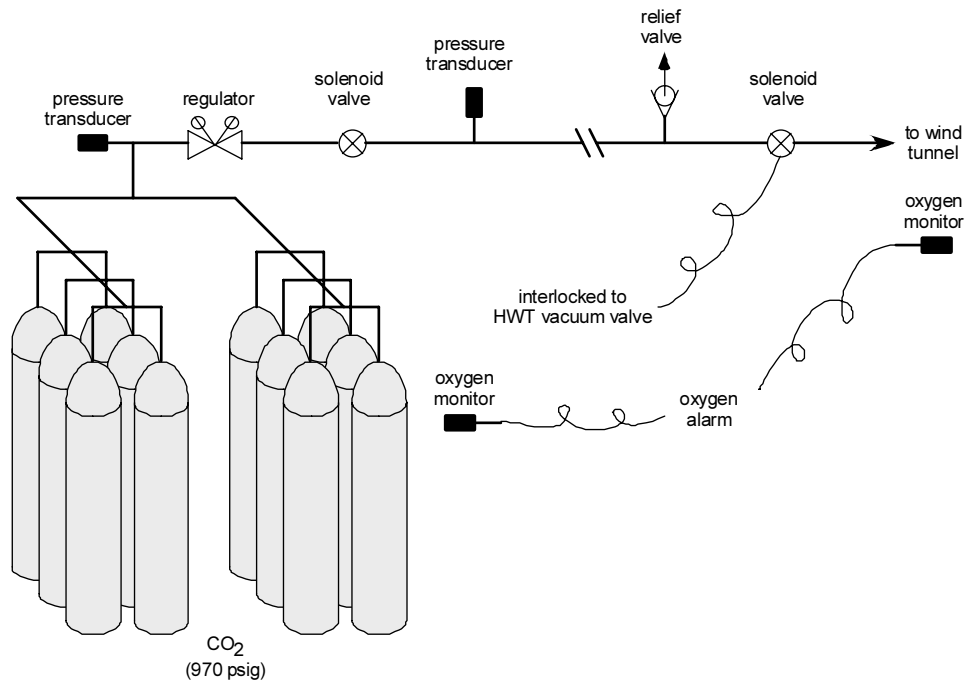
Figure 43 – A schematic of the carbon dioxide seeding system for the HWT.
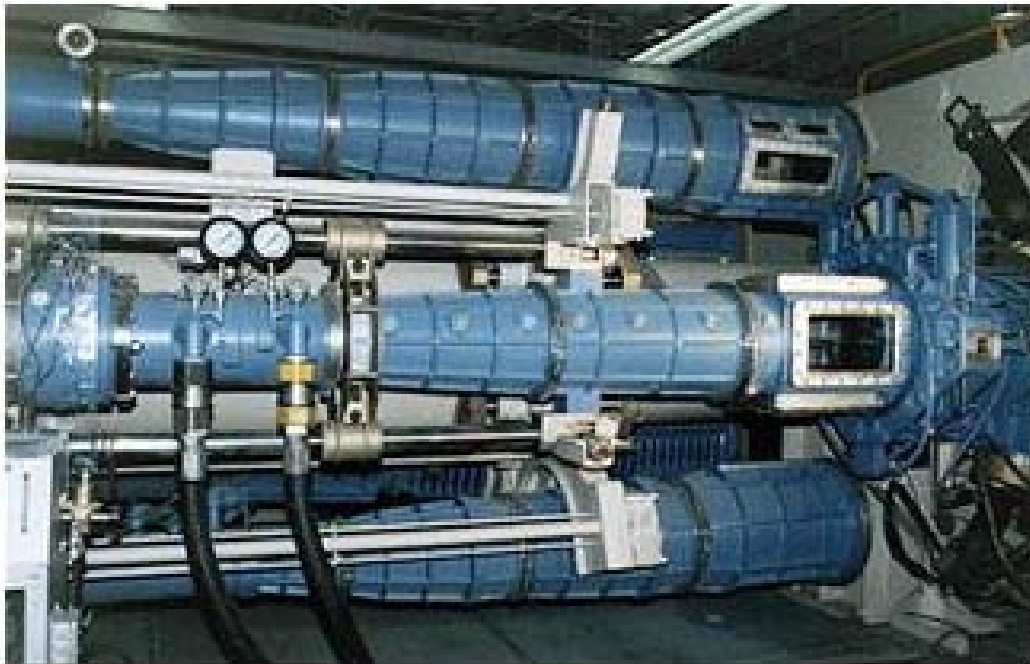
Figure 44 – A photograph of the hypersonic wind tunnel (HWT). The laser for DGV measurements must be brought over the top of the facility in beam tubes to safely reach the test section.

PROJECT SUMMARY AND CONCLUSIONS

FRS Temperature Imaging – Conclusions

A filtered Rayleigh scattering (FRS) instrument for quantitative temperature imaging has been developed in Sandia's Engineering Sciences Center. The FRS instrument has been applied in a systematic manner to increasingly difficult applications. Our FRS system was first applied to heated air jets, where chemistry dependent variations in Rayleigh cross section that are the main source of bias error in flames are not an issue. The FRS system was then applied to nonsooting premixed and diffusion flames. The premixed flame provided an environment where variations in scattering cross section were moderate, while the diffusion flame was a more severe test with extreme variations in cross section that were corrected using Raman imaging of the methane fuel molecule and a mixture-fraction-based model. The FRS thermometry program was concluded with an investigation of a sooting, premixed ethylene-air flame and complimentary laser-induced incandescence (LII) measurements of the local soot volume fraction.

In the nonreacting heated air-jet flowfield, the precision in the shot-averaged FRS temperatures is on the order of $\pm$ 20 K for a laminar jet at 800-K bulk temperature issuing into 293-K air.

When the Rayleigh cross section of the combustion gases is evaluated using the actual gas composition of the premixed CH_4-air flat flame, the shot-averaged FRS flame-temperature data are within ±50 K of adiabatic equilibrium temperatures and corroborating nitrogen CARS measurements for equivalence ratios less than about 1.3. At richer equivalence ratios, the FRS results displayed a high-temperature bias on the order of 75 K. Use of the cross section for nitrogen leads to a low-temperature bias of as high as 150 K in FRS temperatures for lean to slightly rich ϕ. Assumption of stoichiometric product cross section for all ϕ results in greatly minimized bias errors for ϕ from 0.8 to 1.2.

FRS-temperature, Raman fuel-mole-fraction, and CH-chemiluminescence data have been presented for a steady CH_4-N_2-air diffusion flame. FRS-measured peak flame temperatures in the steady-state reference flame were generally within -5% of CARS-measured peak flame temperatures. Data from periodically forced diffusion flames at the 7.5- and 90-Hz forcing frequencies previously studied by Mueller and Schefer [34] have also been presented. The 7.5-Hz case shows the impact of a single fuel-side vortex interacting with the flame zone with

changes in local flame temperature from as high as 1950-2000 K (near adiabatic equilibrium) in regions of negative strain to 1650-1750 K in regions of strong, positive strain, which are believed to be 50-100 K too low. The 90-Hz forcing case permitted the study of two interacting fuel-side vortices that combine to produce strain rates that are high enough to cause localized flame extinction. FRS-measured temperatures near flame quenching are on the order of 1600-1650 K.

FRS measurements from the sooting premixed C_2H_4-air flame proved to be possible for soot volume fractions of order 0.1 ppm or less. The FRS data from this sooting flame were also necessarily corrected for spectrally broadband interferences from soot LII and C_2/PAH emission. These corrections were approximate in nature and were less than 10% of the measured FRS signal for 4 of the 5 flames investigated. In these 4 flames, the measured FRS temperatures were 1500-1700 K, which are 100-200 K lower than expected values. These measurements are currently being repeated with a shorter ICCD gate to further reduce measurement bias resulting from spectrally broadband interferences. The sooting flame is also being better stabilized and will be probed using the nitrogen CARS technique to obtain a more quantitative assessment of FRS performance under sooting conditions.

FRS Velocity Imaging – Summary and Conclusion

A Doppler global velocimetry (DGV) system has been designed, constructed, and tested for use in a Mach 3.7 overexpanded jet prior to future implementation in a hypersonic wind tunnel. The present work describes the implementation and operation of the system, including the optical configuration, the iodine cell calibration, the image transformation procedure, and the culminating velocity data reduction. Calibrations of a pressure-broadened iodine cell have shown that the induced line shift can create velocity biases unless a second iodine cell is scanned simultaneously to provide an independent frequency reference. Exploratory velocity data in the jet have been acquired that are experimentally repeatable and consistent with physical expectations, which lends confidence towards the performance of the assembled system. Measurements in Sandia's hypersonic wind tunnel also are planned and construction of this second diagnostic system is largely complete. Measurements in the hypersonic tunnel are currently being performed.

REFERENCES

1.   Fourguette, D.C., R.M. Zurn, and M.B. Long, "Two-Dimensional Rayleigh Thermometry in a Turbulent Nonpremixed Methane-Hydrogen Flame," *Combustion Science and Technology* **44**, 307-317, 1986.

2.   Otugen, M.V., "Uncertainty Estimates of Turbulent Temperature in Rayleigh Scattering Measurements," *Experimental Thermal-Fluid Science* **15**, 25-31, 1997.

3.   Pitts, W.M. and T. Kashiwagi, "The Application of Laser-Induced Rayleigh Light Scattering to the Study of Turbulent Mixing," *Journal of Fluid Mechanics* **141**, 391-429, 1984.

4.   Eckbreth, A.C., *Laser Diagnostics for Combustion Temperature and Species*: Abacus Press, Cambridge, MA, 1988.

5.   Kearney, S.P. and F.V. Reyes, "Quantitative Temperature Imaging in Gas-Phase Turbulent Thermal Convection by Laser-Induced Fluorescence of Acetone," *Experiments in Fluids* **37**, 87-97, 2003.

6.   Miles, R.B., J.N. Forkey, and W.R. Lempert, "*Filtered Rayleigh Scattering Measurements in Supersonic/Hypersonic Facilities,*" AIAA paper 92-3894, 30th Aerospace Sciences Meeting and Exhibit: Reno, NV, 1992.

7.   Elliott, G.S., N. Glumac, C.D. Carter, and A.S. Nejad, "Two-Dimensional Temperature Field Measurements Using a Molecular Filter Based Technique," *Combustion Science and Technology* **125**, 351-369, 1997.

8.   Elliott, G.S., N. Glumac, and C.D. Carter, "Molecular Filtered Rayleigh Scattering Applied to Combustion," *Measurement Science and Technology* **12**, 452-466, 2001.

9.   Most, D. and A. Leipertz, "Simultaneous Two-Dimensional Flow Velocity and Gas Temperature Measurements by use of a Combined Particle-Image Velocimetry and Filtered Rayleigh Scattering Technique," *Applied Optics* **40**, 5379-5387, 2001.

10.   Hoffman, D., K.U. Munch, and A. Leipertz, "Two-Dimensional Temperature Determination in Sooting Flames by Filtered Rayleigh Scattering," *Optics Letters* **21**(7), 525-527, 1996.

11.   Samimy, M. and S.K. Lele, "Motion of Particles with Inertia in a Compressible Free Shear Layer," *Physics of Fluids A* **3**(8), 1915-1923, 1991.

12.   Melling, A., "Tracer Particles and Seeding for Particle Image Velocimetry," *Measurement Science and Technology* **8**(12), 1406-1416, 1997.

13.   Sutton, G.P., *Rocket Propulsion Elements*: Wiley, New York, 1992.

14. Summerfield, M., C.R. Foster, and W.C. Swan, "Flow Separation in Overexpanded Supersonic Exhaust Nozzles," *Jet Propulsion* **24**, 319-321, 1954.

15. Arens, M. and E. Spiegler, "Shock-Induced Boundary Layer Separation in Overexpanded Conical Exhaust Nozzles," *AIAA Journal* **1**(3), 578-581, 1963.

16. Morrisette, E.L. and T.J. Goldberg, *Turbulent-Flow Separation Criteria for Overexpanded Supersonic Nozzles*: NASA TP-1207, 1978.

17. Romine, G.L., "Nozzle Flow Separation," *AIAA Journal* **36**(9), 1618-1625, 1998.

18. Frey, M. and G. Hagemann, "Restricted Shock Separation in Rocket Nozzles," *Journal of Propulsion and Power* **16**(3), 478-484, 2000.

19. Murdock, J.W. and R.P. Welle, "Downstream Gas Effect on Nozzle Flow-Separation Location," *Journal of Propulsion and Power* **17**(4), 935-937, 2001.

20. Beresh, S.J., J.F. Henfling, and R.J. Erven, "*Flow Separation Inside a Supersonic Nozzle Exhausting into a Subsonic Compressible Crossflow,*" AIAA Paper 2002-1067, 40th AIAA Aerospace Sciences Meeting and Exhibit: Reno, NV, 2002.

21. Deck, S. and P. Guillen, "Numerical Simulation of Side Loads in an Ideal Truncated Nozzle," *Journal of Propulsion and Power* **18**(2), 261-269, 2002.

22. Tenti, G., C.D. Boley, and R.C. Desai, "On the Kinetic Model Description of Rayleigh-Brillouin Scattering from Molecular Gases," *Canadian Journal of Physics* **52**(4), 285-290, 1974.

23. Ghaem-Maghami, V. and A.D. May, "Rayleigh-Brillouin Spectrum of Compressed He, Ne, and Ar II. The Hydrodynamic Regime," *Physical Review A* **22**(2), 698-705, 1980.

24. Ghaem-Maghami, V. and A.D. May, "Rayleigh-Brillouin Spectrum of Compressed He, Ne, and Ar I. Scaling," *Physical Review A* **22**(2), 692-697, 1981.

25. Elliott, G.S. and T.J. Beutner, "Molecular Filter Based Planar Doppler Velocimetry," *Progress in Aerospace Sciences* **35**, 799-845, 1999.

26. McKenzie, R.L., "Measurement Capabilities of Planar Doppler Velocimetry Using Pulsed Lasers," *Applied Optics* **35**(6), 948-964, 1996.

27. Forkey, J.N., N.D. Finkelstein, W.R. Lempert, and R.B. Miles, "Demonstration and Characterization of Filtered Rayleigh Scattering for Planar Velocity Measurements," *AIAA Journal* **34**(3), 442-448, 1996.

28. Meyers, J.F., "Development of Doppler Global Velocimetry as a Flow Diagnostics Tool," *Measurement Science and Technology* **6**(6), 769-783, 1995.

29. Forkey, J.N., W.R. Lempert, and R.B. Miles, "Corrected and Calibrated I$_2$ Absorption Model at Frequency-Doubled Nd:YAG Laser Wavelengths," *Applied Optics* **36**(27), 6729-6738, 1997.

30. Elliott, G.S., M. Samimy, and S.A. Arnette, "A Molecular Filter Based Velocimetry Technique for High Speed Flows," *Experiments in Fluids* **18**(1-2), 107-118, 1994.

31. Clemens, N.T. and M.G. Mungal, "A Planar Mie Scattering Technique for Visualizing Supersonic Mixing Flows," *Experiments in Fluids* **11**(2-3), 175-185, 1991.

32. Gordon, S. and B.J. McBride, *Computer Program for Calculation of Complex Chemical Equilibrium Compositions and Applications -- I. Analysis*: NASA RP 1311, 1994.

33. Smyth, K.C., J.H. Miller, R.C. Dorfman, W.G. Mallard, and R.J. Santoro, "Soot Inception in a Methane/Air Diffusion Flame as Characterized by Detailed Species Profiles," *Combustion and Flame* **62**, 157-181, 1985.

34. Mueller, C.J. and R.W. Schefer, "Coupling of Diffusion Flame Structure to an Unsteady Vortical Flowfield," *Proceedings of the Combustion Institute* **27**, 1105-1112, 1998.

35. Starner, S.H., R.W. Bilger, and M.B. Long, "A Method for Contour-Aligned Smoothing of Joint 2D Scalar Images in Turbulent Flames," *Combustion Science and Technology* **107**, 195-203, 1995.

36. Peters, N., *Turbulent Combustion*: Cambridge University Press, Cambridge, UK, 2000.

37. Starner, S.H., R.W. Bilger, K.M. Lyons, J.H. Frank, and M.B. Long, "Conserved Scalar Measurements in Turbulent Diffusion Flames by a Raman and Rayleigh Imaging Method," *Combustion and Flame* **99**, 347-354, 1994.

38. Starner, S.H., R.W. Bilger, J.H. Frank, D.F. Marran, and M.B. Long, "Mixture Fraction Imaging in a Lifted Methane Jet Flame," *Combustion and Flame* **107**, 307-313, 1996.

39. Starner, S.H., R.W. Bilger, M.B. Long, J.H. Frank, and D.F. Marran, "Scalar Dissipation Measurements in Turbulent Jet Diffusion Flames of Air-Diluted Methane and Hydrogen," *Combustion Science and Technology* **129**, 141-163, 1997.

40. Chen, S.J., J.A. Silver, W.J.A. Dahm, and N.D. Piltch, "Mixture Fraction Measurements via WMS/ITAC in a Laminar Diffusion Flame," *Proceedings of the Combustion Institute* **29**, 1-10, 2002.

41. Schefer, R.W., Personal Communication, 2002.

42. Schefer, R.W., Personal Communication, 2003.

43. Farrow, R.L., R.P. Lucht, W.L. Flower, and R.E. Palmer, "Coherent Anti-Stokes Raman Spectroscopic Measurements of Temperature and Acetylene Spectra in a Sooting

Diffusion Flame," *Twentieth Symposium (International) on Combustion* , 1307-1312, 1984.

44. Bengtsson, P.E., L. Martinsson, M. Aldén, and S. Kröll, "Rotational CARS Thermometry in Sooting Flames," *Combustion Science and Technology* **81**, 129-140, 1992.

45. Brackmann, C.J., C.J. Bood, P.E. Bengtsson, T. Seeger, M. Schenk, and A. Leipertz, "Simultaneous Vibrational and Pure Rotational Coherent Anti-Stokes Raman Spectroscopy for Temperature and Multispecies Concentration Measurements Demonstrated in Sooting Flames," *Applied Optics* **41**(3), 564-572, 2002.

46. Aldén, M. and S. Wallin, "CARS Experiments in a Full-Scale (10 m X 10 m) Industrial Coal Furnace," *Applied Optics* **24**(21), 3434-3437, 1985.

47. Lucht, R.P., *Coherent Anti-Stokes Raman Scattering Measurements in Coal-Particle-Laden Flames*: SAND88-8721, Sandia National Laboratories; Livermore, CA, 1988.

48. Bradley, D.M., M. Lawes, M.J. Scott, and N. Usta, "The Structure of Coal-Air-CH4 Laminar Flames in a Low-Pressure Burner: CARS Measurements and Modeling Studies," *Combustion and Flame* **124**, 82-105, 2001.

49. Harris, L.E. and M.E. McIlwain, "Coherent Anti-Stokes Raman (CARS) Temperature Measurements in a Propellant Flame," *Combustion and Flame* **48**(1), 97-100, 1982.

50. Stufflebeam, J.H. and A.C. Eckbreth, "CARS Diagnostics of Solid-Propellant Combustion at Elevated Pressure," *Combustion Science and Technology* **66**, 163-179, 1989.

51. Nygren, J., J. Engstrom, J. Walewski, C.F. Kaminski, and M. Aldén, "Applications and Evaluation of Two-Line Atomic LIF Thermometry in Sooting Combustion Environments," *Measurement Science and Technology* **12**, 1294-1303, 2001.

52. Rabenstein, F. and A. Leipertz, "One Dimensional, Time-Resolved Raman Measurements in a Sooting Flame Made with 355-nm Excitation," *Applied Optics* **37**(21), 4937-4943, 1998.

53. Shaddix, C.R. and K.C. Smyth, "Laser-Induced Incandescence Measurements of Soot Production in Steady and Flickering Methane, Propane, and Ethylene Diffusion Flames," *Combustion and Flame* **107**, 418-452, 1996.

54. VanderWal, R.L. and K.J. Welland, "Laser-Induced Incandescence: Development and Characterization Towards a Measurement of Soot-Volume Fraction," *Applied Physics B* **59**, 445-452, 1994.

55. VanderWal, R.L., "Laser-Induced Incandescence: Detection Issues," *Applied Optics* **35**(33), 6548-6559, 1996.

56. VanderWal, R.L., K.A. Jensen, and M.Y. Choi, "Simultaneous Laser-Induced Emission of Soot and Polycyclic Aromatic Hydrocarbons Within a Gas-Jet Diffusion Flame," *Combustion and Flame* **109**, 399-414, 1997.

57. Witze, P.O., S. Hochgreb, D. Kayes, H.A. Michelson, and C.R. Shaddix, "Time-Resolved Laser-Induced Incandescence and Laser Elastic-Scattering Measurements in a Propane Diffusion Flame," *Applied Optics* **40**(15), 2443-2452, 2001.

58. Beretta, F., A. D'Alessio, A. D'Orsi, and P. Minutolo, "U.V. and Visible Laser Excited Fluorescence from Rich Premixed and Diffusion Flames," *Combustion Science and Technology* **85**, 455-470, 1992.

59. Beretta, F., V. Cincotti, A. D'Alessio, and P. Menna, "Ultraviolet and Visible Fluorescence in the Fuel Pyrolysis Regions of Gaseous Diffusion Flames," *Combustion and Flame* **61**, 211-218, 1985.

60. Bengtsson, P.E. and M. Aldén, "C_2 Production and Excitation in Sooting Flames Using Visible Laser Radiation: Implications for Diagnostics in Sooting Flames," *Combustion Science and Technology* **77**, 307-318, 1991.

61. Xu, F., P.B. Sunderland, and G.M. Faeth, "Soot Formation in Laminar Premixed Ethylene / Air Flames at Atmospheric Pressure," *Combustion and Flame* **108**, 471-493, 1997.

62. Bengtsson, P.E. and M. Aldén, "Soot Visualization Strategies Using Laser Techniques," *Applied Physics B* **60**, 51-59, 1995.

63. Dasch, C.J., "One-Dimensional Tomography: A Comparison of Abel, Onion-Peeling, and Filtered Backprojection Methods," *Applied Optics* **31**(8), 1146-1152, 1992.

64. Dalzell, W.H. and A.F. Sarofim, "Optical Constants of Soot and Their Application to Heat-Flux Calculations," *Journal of Heat Transfer* **91**, 100-104, 1969.

65. Smyth, K.C. and C.R. Shaddix, "The Elusive History of m = 1.57 - 0.56i for the Refractive Index of Soot," *Combustion and Flame* **107**, 314-320, 1996.

66. Seasholtz, R.G. and A.G. Buggele, *Improvement in Suppression of Pulsed Nd:YAG Laser Light with Iodine Absorption Cells for Filtered Rayleigh Scattering Measurements*: NASA TM 113177, 1997.

67. Crafton, J., C.D. Carter, and G.S. Elliott, "Three-Component Phase-Averaged Velocity Measurements of an Optically Perturbed Supersonic Jet using Multi-Component Planar Doppler Velocimetry," *Measurement Science and Technology* **12**(4), 409-419, 2001.

68. Padrick, T.D. and R.E. Palmer, "Pressure Broadening of the Atomic Iodine 52P1/2 - 52P3/2 Transition," *Journal of Chemical Physics* **62**(8), 3350-3352, 1975.

69.   Mukhtar, E.A., H.J. Baker, and T.A. King, "Pressure Induced Frequency Shifts in the Atomic Iodine Laser," *Optics Communications* **24**(2), 167-169, 1978.

70.   Fletcher, D.G. and J.C. McDaniel, "Laser-Induced Iodine Fluorescence Technique for Quantitative Measurement in a Nonreacting Supersonic Combustor," *AIAA Journal* **27**(5), 575-560, 1989.

DISTRIBUTION

1	MS-0151	09750	A.C. Ratzel
1	MS-0323	01011	D.L. Chavez (LDRD Office)
1	MS-0821	09132	L.A. Gritzo
1	MS-0825	09115	B. Hassan
1	MS-0825	09115	W.P. Wolfe
1	MS-0825	09110	W.L. Hermina
1	MS-0826	09113	J.R. Torczynski
1	MS-0828	09133	W.L. Oberkampf
10	MS-0834	09112	S.P. Kearney
1	MS-0834	09112	T.W. Grasser
10	MS-0834	09112	S.J. Beresh
1	MS-0834	09112	W.M. Trott
1	MS-0834	09112	T.J. O'Hern
1	MS-0834	09112	M.R. Prairie
1	MS-0834	09112	C.J. Bourdon
1	MS-0834	09112	S.M. Trujillo
1	MS-0834	09112	D.J. Rader
1	MS-0834	09112	J.F. Henfling
1	MS-0841	09100	T.C. Bickel
1	MS-0841	09100	C.W. Peterson
1	MS-1135	09132	J.C. Hewson
1	MS-1135	09132	K.A. Jensen
1	MS-1135	09132	J.T. Nakos
1	MS-1135	09132	S.R. Tieszen
1	MS-1146	09132	T.K. Blanchat
1	MS-1162	15414	W.H. Rutledge
1	MS-1393	09100	T.Y. Chu
1	MS-9051	08367	R.W. Schefer
1	MS-9051	08351	J.H. Frank
1	MS-9052	08367	C.R. Shaddix
1	MS-0612	09612	Review and Approval Desk for DOE/OSTI-
2	MS-0899	09616	Technical Library
1	MS-9018	08945-1	Central Technical File

Campbell D. Carter
Aerospace Propulsion Office (AFRL/PRA)
1950 5th St.
Wright-Patterson AFB, OH 45433

Greg Elliott
Department of Aerospace Engineering
University of Illinois at Urbana-Champaign
306 Talbot Lab
103 S. Wright St.
Urbana, IL 61801